

Acoustic Noise and Vibration of Brushless Motors for Fans

Thesis submitted for the degree of
Doctor of Philosophy at the University of Leicester

by

Yi Cheng BEng (Leicester)
Department of Engineering
University of Leicester

September 2005

UMI Number: U212059

All rights reserved

INFORMATION TO ALL USERS

The quality of this reproduction is dependent upon the quality of the copy submitted.

In the unlikely event that the author did not send a complete manuscript and there are missing pages, these will be noted. Also, if material had to be removed, a note will indicate the deletion.



UMI U212059

Published by ProQuest LLC 2015. Copyright in the Dissertation held by the Author.
Microform Edition © ProQuest LLC.

All rights reserved. This work is protected against
unauthorized copying under Title 17, United States Code.



ProQuest LLC
789 East Eisenhower Parkway
P.O. Box 1346
Ann Arbor, MI 48106-1346

Acknowledgements

I thank God for His blessings and support from whom I've constantly received, and continue to receive. I want to express my greatest gratitude to Professor Charles Pollock for his support and guidance, and most of all for his patience and encouragement, without whom the work described in this thesis could not have been accomplished. Thank you to members of my beloved family to whom I dedicate this work and from whom I've been given financial and moral support, and Miss Tian Hui Wang for her undivided care and encouragement during most of my time in the research course.

I want to thank the Overseas Research Students Awards Scheme (ORSAS) for partially funding me to take up this research study, and The Carbon Trust, UK for further financial support. I would also like to thank the staffs and students in the Engineering Department whom I have worked with during the course of this project for their friendship, encouragement, ingenuity, technical skills and support. The interest and support from companies within the Centre for Advanced Electronically Controlled Drives are greatly appreciated as well. Special thanks also to Arnold Magnetics Limited who have generously supplied the permanent magnets for prototyping.

Beyond the laboratory, I want to thank my friends for just being there to share, to have fun and to inspire.

Yi Cheng.

September 2005

Name of author: YI CHENG

Title of thesis: ACOUSTIC NOISE AND VIBRATION OF BRUSHLESS MOTORS FOR FANS

Abstract

An investigation on vibration and acoustic noise on brushless motors for fan or blower applications is presented, particularly concentrating on the vibration due to electromagnetic origin within the brushless electronically commutated motors.

The flux switching motor is introduced as a relatively new class of reluctance machine, which retains the benefits of switched reluctance machines, but with simpler and cheaper power electronic converters. The novel work of this thesis is the introduction of two $8/4$ flux switching motors with permanent magnets of internal rotor and external rotor configuration respectively, which are presented as alternatives for the brushless DC motor, and called the permanent magnet flux switching motor. The two new permanent magnet flux switching motors were able to show potential in reducing power consumption, reducing vibration and noise, and reducing the cost of the power electronic drive when compared with an existing commercial 3-phase brushless DC and induction motor.

Investigation on the vibration and noise of the flux switching motor was also done by performing experiments, mechanical finite element analysis and algebraic frequency equation analysis. Algebraic frequency equations were implemented into the electromagnetic design environment, stressing the need and potential in having algebraic frequency equations to predict the mechanical resonant frequency of any shape of the electrical machine stator lamination in the electromagnetic design environment.

Table of Contents

Acknowledgements.....	ii
Abstract.....	iii
Table of Contents.....	iv
List of Figures.....	vi
List of Tables.....	x
List of Symbols.....	xi
Chapter 1 INTRODUCTION.....	1
1.1 Introduction.....	1
1.2 Objectives.....	2
1.3 Format of Thesis.....	2
1.4 Principle operation of the flux switching motor.....	3
1.5 Sources of acoustic noise.....	5
1.6 Weighting functions.....	7
1.7 Behavior of the stator during vibration.....	8
Chapter 2 INVESTIGATION ON THE PERMANENT MAGNET BRUSHLESS DC MOTOR ...	10
2.1 Introduction.....	10
2.2 Principle operation and converter topology.....	11
2.3 The acoustic noise and vibration investigation.....	13
2.4 Experimental tests.....	15
2.5 Summary.....	23
Chapter 3 VIBRATION AND ACOUSTIC NOISE INVESTIGATION ON THE FLUX SWITCHING MOTOR.....	24
3.1 Introduction.....	24
3.2 Investigation on the round-shaped flux switching motor.....	25
3.3 Investigation on the polygon-shaped flux switching motor.....	34
3.4 Summary.....	47
Chapter 4 PREDICTING THE MECHANICAL RESONANT FREQUENCY OF THE FLUX SWITCHING MOTOR.....	48
4.1 Introduction.....	48
4.2 Finite element analysis of mechanical resonant frequency.....	49
4.3 Mechanical resonant frequency prediction of electrical machines using algebraic analysis ...	54
4.4 Implementation of simple algebraic frequency equation.....	58

4.5 Summary	62
Chapter 5 THE PERMANENT MAGNET FLUX SWITCHING MOTOR: THE INTERNAL ROTOR VERSION.....	64
5.1 Introduction	64
5.2 Evolution of the PMFSM	66
5.3 Electromagnetic finite element design	68
5.4 Design of the internal rotor permanent-magnet flux switching motor.....	68
5.5 CAD design.....	74
5.6 Experimental tests on the internal rotor PMFSM, INTPMFSM 2	79
5.7 Summary	83
Chapter 6 THE PERMANENT-MAGNET FLUX SWITCHING MOTOR: THE EXTERNAL ROTOR VERSION.....	84
6.1 Introduction	84
6.2 Design of the external rotor permanent-magnet flux switching motor	85
6.3 CAD design.....	91
6.4 Experimental tests on the external rotor PMFSM, EXTPMFSM 2	96
6.5 Summary for the internal rotor and external rotor PMFSM.....	100
Chapter 7 CONCLUSION AND FUTURE WORKS	102
7.1 Conclusion.....	102
7.2 Future works.....	103
REFERENCES	105
Appendix A Power Circuit Board.....	108
Appendix B A-weighting post-processing of noise in MATLAB	110
Appendix C Determining the torque direction for external rotor PMFSM	111
Appendix D Ferrite magnet BH curves	113
Appendix E New Permanent-magnet Flux Switching Motor CAD drawings	114
Appendix F Assembly of INTPMFSM 2 and EXTPMFSM 2	139

List of Figures

Figure 1.1: 4/2 Flux switching motor with the rotor at 2 different aligned positions.....	3
Figure 1.2: H-bridge power electronic converter.....	4
Figure 1.3: New power electronic converter to accommodate bifilar armature windings.....	4
Figure 1.4: Parallel configuration of power electronic converter with bifilar armature windings	5
Figure 1.5: A-, B-, C- and D- weighting networks (Taken from [9]).....	7
Figure 1.6: Circumferential vibration modes [23].....	8
Figure 1.7: Longitudinal vibration modes [23].....	9
Figure 2.1: Schematic diagram of the internal stator bifilar windings	11
Figure 2.2: Permanent magnet external rotor	11
Figure 2.3: Schematic circuit diagram of the power electronic inverter drive.	11
Figure 2.4: Waveforms at 2000rpm.....	12
Figure 2.5: The permanent magnet brushless DC.....	12
Figure 2.6: A-weighting network applied in MATLAB obtained from [9].....	14
Figure 2.7: Acoustic noise frequency spectrum under load at 2000rpm.	15
Figure 2.8: Vibration FFT at 2000rpm on inner frame.....	16
Figure 2.9: Schematic diagram to perform static vibration test.....	17
Figure 2.10: Static vibration test with rotor locked at stable equilibrium position	18
Figure 2.11: Static vibration test with rotor locked at aligned, stable equilibrium position before 3- stage commutation method.....	20
Figure 2.12: Static vibration test with rotor locked at aligned, stable equilibrium position after 3- stage commutation method.....	20
Figure 2.13: Waveforms before 3-stage commutation method	21
Figure 2.14: Waveforms after 3-stage commutation method	21
Figure 2.15: Acoustic noise frequency spectrum.....	22
Figure 2.16: Noise frequency domain with estimated siren tone harmonics at 2000rpm.	23
Figure 3.1: Schematic diagram for static vibration test	25
Figure 3.2: Round-shaped flux switching motor	26
Figure 3.3: Vibration signals when rotor aligned in position 1 and 5.....	27
Figure 3.4: Vibration measuring points	28
Figure 3.5: Vibration signals when rotor aligned in position 3 and 7.....	28
Figure 3.6: Vibration signals when rotor aligned in position 3 and 7.....	29
Figure 3.7: Vibration on stator at 1800rpm	30

Figure 3.8: Vibration on stator at 480rpm	31
Figure 3.9: Acoustic noise at 1800rpm measured about 15cm away from stator.....	32
Figure 3.10: Acoustic noise at 480rpm measured about 15cm away from stator.....	32
Figure 3.11: Vibration at circular frame at 1800rpm.....	33
Figure 3.12: Vibration at circular frame at 480rpm.....	33
Figure 3.13: Polygon-shaped flux switching motor.....	34
Figure 3.14 : Static vibration test on polygon-shaped flux switching motor.....	35
Figure 3.15: Static vibration test results	36
Figure 3.16: Vibration data after bandpass filtering between 500Hz and 1500Hz.....	37
Figure 3.17: Vibration mode $m=1$ at around 700Hz.....	38
Figure 3.18: Vibration data after bandpass filtering between 2000Hz and 5000Hz.....	39
Figure 3.19: Vibration mode $m=2$ at around 3500Hz.....	40
Figure 3.20: Current and voltage waveforms are obtained at 10000rpm.	41
Figure 3.21: Plot of vibration frequency against motor speed.....	42
Figure 3.22: Acoustic noise surface plot.....	43
Figure 3.23: Current and voltage waveforms are obtained at 10000rpm	44
Figure 3.24: Current and voltage waveforms at 16350rpm.	45
Figure 3.25: Acoustic noise FFTs at 16350rpm.....	45
Figure 3.26: Surface plot showing acoustic noise frequency against motor speed	46
Figure 4.1: Round-shaped FSM model in FEMLAB.	49
Figure 4.2: Constraints applied on round-shaped FSM model	50
Figure 4.3: Vibration mode 2 of round-shaped flux switching motor	51
Figure 4.4: Polygon-shaped FSM model in FEMLAB	52
Figure 4.5: Photo of actual polygon-shaped flux switching motor with supports.....	52
Figure 4.6: Vibration at 3442.31Hz of mode 2.....	53
Figure 4.7: Stator ring of flux switching motor	58
Figure 4.8: Geometric parameters for frequency equation calculation.....	61
Figure 4.9: An example of a stator ring with the combination of $r1$ and $r5$	61
Figure 5.1: A permanent magnet flux switching motor, PMFSM.	64
Figure 5.2: A conventional flux switching motor.....	66
Figure 5.3: Proposed permanent magnet configuration.....	67
Figure 5.4: A permanent magnet flux switching motor.....	67
Figure 5.5: Back-emf of INTPMFSM 1	69
Figure 5.6: Simulated torque waveforms for INTPMFSM 1.....	70

Figure 5.7: Modified INTPMFSM 2.....	71
Figure 5.8: Simulated torque waveforms for INTPMFSM 2.....	72
Figure 5.9: Existing ventilation fan with 3-phase brushless DC motor.....	74
Figure 5.10: Winding configuration for PMFSM.....	75
Figure 5.11: Internal rotor PMFSM, INTPMFSM 2.....	76
Figure 5.12: Stator lamination of INTPMFSM 2.....	76
Figure 5.13: Partly assembled INTPMFSM 2	76
Figure 5.14: Exploded CAD drawing of INTPMFSM 2	77
Figure 5.15: Assembled view with existing components	77
Figure 5.16: Assembled view of INTPMFSM 2.....	77
Figure 5.17: View showing rotor-shaft assembly with other components	77
Figure 5.18: Assembled section view of INTPMFSM 2	77
Figure 5.19: Fan blade with reflective and non-reflective tapes to act as sensor interrupter	78
Figure 5.20: Opto-sensor circuit schematic	78
Figure 5.21: Power converter schematic driving both PMFSM prototypes	79
Figure 5.22: Comparison of back EMF from simulation and experiment of INTPMFSM 2 at 443rpm.....	80
Figure 5.23: Waveforms of INTPMFSM 2 at 3 different speeds	81
Figure 6.1: External rotor version of PMFSM.....	84
Figure 6.2: Back-emf and armature flux of EXTPMFSM 1	85
Figure 6.3: Simulated torque waveforms for EXTPMFSM 1.....	86
Figure 6.4: Modified EXTPMFSM 2	87
Figure 6.5: Simulated instantaneous torque and back-EMF waveform for EXTPMFSM 2	88
Figure 6.6: External rotor PMFSM, EXTPMFSM 2	92
Figure 6.7: Stator lamination of EXTPMFSM 2	92
Figure 6.8: Exploded CAD drawing of EXTPMFSM 2	92
Figure 6.9: Assembled view	93
Figure 6.10: Assembled section view inside the EXTPMFSM 2	93
Figure 6.11: Assembled EXTPMFSM 2 without existing housings.....	93
Figure 6.12: Assembled rotor and rotor frames with fan blade housing	93
Figure 6.13: Assembled stator laminations, magnets and frames.....	93
Figure 6.14: Static shaft for EXTPMFSM 2 design without modification.....	94
Figure 6.15: Rotor position when rotor shorts magnet flux paths	94
Figure 6.16: Partly assembled external rotor PMFSM with additional washer and nut.....	95

Figure 6.17: Simulated and experimental back-EMF waveform for EXTPMFSM 2.....	96
Figure 6.18: Waveforms of EXTPMFSM 2 at 3 different speeds.....	97
Figure C.1: External rotor topology.....	111
Figure C.2: Blue line is 400At, red line is -400At.....	111
Figure C.3: -400At at 9°.....	111
Figure C.4: 400At at 52°.....	111
Figure C.5: Correct instantaneous torque waveform for external rotor design.....	112
Figure D.1: BH Curves for ARNOX-AC8 permanent magnets.....	113

List of Tables

Table 3.1: Measured mechanical resonant frequency.....	47
Table 4.1: Comparison of measured and finite element predicted mechanical resonant frequency..	53
Table 4.2: Geometric dimensions and material constants	58
Table 4.3: Calculated mechanical resonant frequencies for mode 2	59
Table 4.4: Comparison of measured and calculated mechanical resonant frequencies for vibration mode 2	59
Table 4.5: Comparison between finite element prediction and algebraic prediction	60
Table 4.6: Table of predicted mechanical resonant frequencies with equivalent stator ring geometry	62
Table 5.1: Comparison of performance among IM, BLDC, and INTPMFSM 2.....	73
Table 5.2: Main dimensions for INTPMFSM 2.....	75
Table 5.3: Comparisons of results between BLDC and INTPMFSM 2	82
Table 5.4: Comparisons of results between BLDC and INTPMFSM 2 with modified predicted results.....	82
Table 6.1: Comparison of performance among IM, BLDC, INTPMFSM 2 and EXTPMFSM 2.....	90
Table 6.2: Main dimensions for EXTPMFSM 2	91
Table 6.3: Comparison of experimental results between BLDC and EXTPMFSM 2.....	98
Table 6.4: Comparison of results between BLDC and EXTPMFSM 2 with modified predicted results.....	98
Table 6.5: Summary of performance comparison between BLDC, INTPMFSM 2 and EXTPMFSM 2	99
Table 6.6: Comparison of experimental results between IM, INTPMFSM 2 and EXTPMFSM 2	99
Table D.1: Courtesy of Arnold Magnetics Limited	113
Table E.1: Part names in CAD drawings for INTPMFSM 2 and EXTPMFSM 2.....	114

List of Symbols

$A_{csa,yoke}$	Cross-sectional area of stator yoke in [m ²]
A_z	Mean tooth cross sectional area in [m ²]
b	Stator core length in [m]
E	Young's Modulus in [GPa]
e	Electro-motive force in [V]
F	Magneto-motive force in [At/m]
f	Frequency in [Hz]
G	Shear Modulus in [GPa]
G_B	Weight of insulations in [N]
G_f	Weight of stator yoke, i.e. weight of stator without teeth in [N]
G_w	Weight of windings in [N]
G_z	Total weight of teeth in [N]
h	Thickness of stator yoke in [m]
I_m	2 nd moment of cross-sectional area in [m ²]
i	Current in [A]
k	Number of nodal diameter
L	Inductance in [H]
L_{spl}	Sound pressure level, SPL, in [dB]
L_{stk}	Stack length in [m]
l_z	Tooth length in [m]
M	Mutual inductance in [H]
m	Circumferential vibration mode number
N	Number of winding turns
n	Longitudinal vibration mode number
n_{rpm}	Motor speed in [rpm]
p	Linear RMS value of acoustic pressure at a particular frequency in [Pa]
p_{ref}	RMS reference acoustic pressure, 2×10^{-5} [Pa]
R	Resistance in [Ω]

R_m	Mean radius of stator yoke excluding teeth in [m]
T	Generalized expression for kinetic energy
T_{rel}	Reluctance torque in [Nm]
t	Time in [s]
U	Generalized expression for strain energy
u, v, w	Axial, tangential and radial components of displacements respectively
x	Generalized expression for displacements
Z_{st}	Stator slot number
z_b	Number of fan blades
r, ϕ, z	Cylindrical coordinates
ψ	Flux in [Wb]
ω	Frequency in [rads/s]
ρ	Density of material in [kg/m ³]
ν	Poisson's ratio
θ	Rotor position in [rads]
θ°	Rotor position in [degrees]

Chapter 1

INTRODUCTION

1.1 Introduction

The environmental issue on vibration and acoustic noise produced by electrical motors has been a vital topic in society. Noise is considered undesirable to everyone due to its potential threat towards health and safety of the general public. The study on determining, predicting and reducing vibration and acoustic noise in electrical motors have been on-going for many years. As electrical motors find their way into various commercial uses, such as in offices, homes, etc, this study has become more demanding and challenging. The negative effect of vibration and acoustic noise on the human subject is widely recognised as a problem in industry, as well as in communal areas. Hence, low vibration and acoustic noise has become an important marketing feature in products consisting electrical motors.

The noise produced by brushless electronically commutated motors is of particular interest in recent years, due to the growing interest of using brushless electronically commutated motors in fan applications. Furthermore, it is also because the costs of electronic components has been reasonably low allowing mechanical commutators in brushed machines replaced by electronic commutators, leading to electrical machines without brushes, i.e. brushless electrical machines. These led to low mechanical maintenance costs, no brush noise, higher efficiency, reduction in machine sizes etc, but leaving complex control algorithms in power electronic drives. Well-known brushless electronically commutated motors are the induction motors (IM), switched reluctance motors (SRM), permanent-magnet brushless DC motors (traditionally known as the brushless DC, BLDC), and most recently, the flux switching motors (FSM) [1].

This thesis focuses on the investigation of the vibration and acoustic noise in brushless motors of electromagnetic origin in fan applications, and producing two brushless machines, called the permanent magnet Flux Switching Motor, that are presented as alternatives to the classical brushless DC motor.

The investigation of vibration and acoustic noise of electromagnetic origin in brushless electrical motors are performed in both experimental tests and simulation analysis. Experimental tests involve the dynamic tests and the static test. Simulations to predict the mechanical resonant frequencies (or mechanical natural frequencies) of the stator are performed by the mechanical finite

element package called FEMLAB [2]. The electromagnetic finite element package called Vector Fields OPERA [3] was used to aid in the design of the permanent magnet Flux Switching Motors.

1.2 Objectives

The main objective of this thesis is to investigate the vibration and acoustic noise of electromagnetic origin of brushless motors in fans, by means of performing experiments, implementing algebraic equations and finite element analysis. Two permanent-magnet flux switching motor prototypes are designed to have better efficiency and lower acoustic noise, which are presented as alternatives to the existing BLDC for the same fan application.

1.3 Format of Thesis

This thesis is composed of 7 chapters, including this introductory chapter, and appendices.

Chapter 2 introduces a typical brushless DC topology, of an external rotor configuration, and its power electronic circuits as a conventional kind of brushless DC machine, and introduces a vibration reduction technique called the '3-stage commutation method' to suppress an induced vibration component. Its operation is described, and its vibration and acoustic noise characteristics investigated.

Chapter 3 presents the work on determining the mechanical resonant frequencies and vibration mode shapes of electrical machines. A round-shaped flux switching motor and a polygon-shaped flux switching motor were chosen for this investigation because they had an internal rotor configuration. Chapter 4 then compliments the work in Chapter 3 by introducing the mechanical finite element analysis and algebraic frequency equations to predict the mechanical resonant frequencies and vibration mode shapes of the round-shaped and polygon-shaped flux switching motor.

Chapter 5 and Chapter 6 introduce an internal rotor version and external rotor version of the flux switching motor with permanent magnets, called the permanent magnet flux switching motors, respectively. Both permanent magnet flux switching motors were introduced as alternatives to the classical brushless DC motor in fan applications. Design procedures towards the two prototypes are shown, and the prototypes are built and tested. These 2 prototypes are to compete with an existing AC induction motor and another conventional 3-phase brushless DC. Both prototypes showed that they have potential in consuming less input power, being less noisy and lower in cost than the BLDC and induction motor.

Chapter 7 gives conclusions on the overall work in this thesis, and will have suggestions on future approaches or ideas to carry on the work of investigating and eliminating vibration and acoustic noise in brushless motors.

1.4 Principle operation of the flux switching motor

As most of the work described in this thesis is on the flux switching motor, this section gives a general description of the flux switching motor.

The flux switching motor combines some of the features of the switched reluctance motor and the inductor alternator [1]. Figure 1.1 below shows the simplest construction of a doubly salient 4/2 flux switching motor. Both the field windings and the armature windings are fully-pitched and wound on the stator in this example. The cross and dot symbols in Figure 1.1 show the inward and outward direction of current respectively which are perpendicular to the surface of the paper. The field winding (F) is energized with DC current, whereas the armature winding (A) is energized with electronically altered DC current.

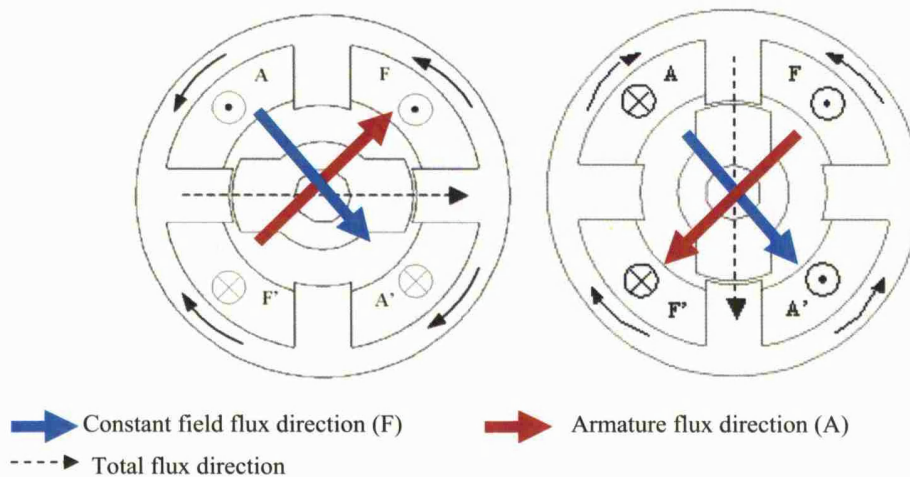


Figure 1.1: 4/2 Flux switching motor with the rotor at 2 different aligned positions

As shown in Figure 1.1, only the armature flux direction is switched at different rotor positions. When the armature current polarity is switched, so does the direction of the total flux, and consequently the salient rotor with no windings tends to align itself to a new position of minimum reluctance. If the switching frequency of the armature current is synchronized relative to the rotor position when inductance of the machine is rising, continuous motoring torque is produced [4] because reluctance torque is defined as

$$T_{rel} = \frac{1}{2} i^2 \frac{dM}{d\theta} \quad (1.1)$$

This synchronism of armature current with respect to rotor position will then produce continuous rotation, and can achieve optimum efficiency. This mechanism of producing torque is also similar to the Laws Relay actuator, where each change in armature current polarity, changes the direction of flux. [5].

There are numerous power electronic converter topologies used to control the switching of the armature currents. For this particular example, a classical H-bridge power electronic converter shown in Figure 1.2 can be used to illustrate the operation.

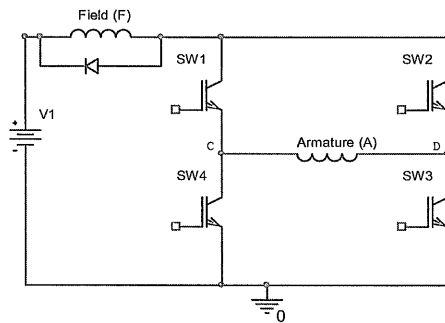


Figure 1.2: H-bridge power electronic converter

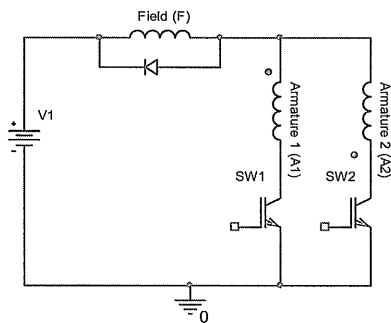


Figure 1.3: New power electronic converter to accommodate bifilar armature windings

In Figure 1.2, SW1 and SW3 are both switched in-phase with each other, but out-of-phase with SW2 and SW4. Switching on SW1 and SW3 applies DC voltage to the armature windings from point C to D, whereas switching on SW2 and SW4 applies negative voltage (C relative to D), reversing the current polarity on the armature windings.

Alternatively, in order to reduce the cost of the electronics, the use of bifilar armature windings can be employed which reduces the number of switches from 4, as shown in Figure 1.2, to 2 switches in the bifilar power electronic converter as shown in Figure 1.3. Basically, the bifilar

armature has two coils with equal numbered of turns, magnetically coupled with each other. Then, each bifilar armature coil has its ends connected opposite from each other onto the power converter as shown in Figure 1.3 by dots representing the start of the coil. The two power electronic switches operate out-of-phase of each other, applying the alternating voltage to the armature windings. The current flows in the same direction from the DC supply, but producing alternating armature flux in the machine.

In addition, the field winding can be connected in series (as already shown in Figure 1.2 and Figure 1.3) or in parallel with the armature windings as shown in Figure 1.4. Advantage of having the series field winding configuration is that higher torque can be achieved, similarly to the series brush DC motor configuration, where the torque is proportional to the square of armature current. However, this poses a difficulty of controlling torque compared with the parallel field winding configuration. The series field winding configuration has a non-linear relationship between torque and armature current, whereas in the parallel winding configuration, similar to the shunt brush DC motor configuration, there is a linear relationship between torque and armature current.

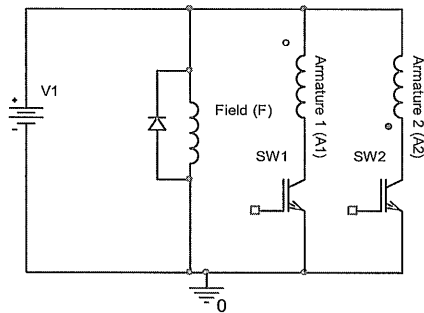


Figure 1.4: Parallel configuration of power electronic converter with bifilar armature windings

1.5 Sources of acoustic noise

The vibration of air particles produces sound, and if the sound is unwanted, undesired to be heard or detected, it is referred to as noise or more scientifically called acoustic noise. Therefore, noise is a consequence of vibration. From a vibrating body, which is the source of vibration, the air particles at the body vibrates, producing fluctuating pressure in the air which propagates in a longitudinal manner towards the human ear drum, and finally processed by the human brain, and interpreted as sound or noise. Therefore, it can be sufficiently recognized that, the source of vibration, is also the source of acoustic noise.

There are mainly three kinds of acoustic noise sources: the electromagnetic source, mechanical source and aerodynamic source. These three sources of acoustic noise interact with one another, and are sometimes dependent on one another.

For variable speed doubly salient machines, acoustic noise due to the electromagnetic induction is mainly produced by radial vibration between the stator and rotor [6]. Radial vibration is induced when the stator and rotor experience radial magnetic air gap forces which are created due to the air gap magnetic energy stored when the field or armature windings are energised. These air gap forces effectively 'hits' the stator surface like a hammer, applying an impulse force onto the stator surface, and the stator responds as a vibration. As the rotor rotates around the stator, continuous impulse forces act on the stator, and on the rotor. In brushless salient pole machines, impulse forces are created at each commutation of current in the armature winding to create a damped vibration as shown from time domain analysis when each step change in applied voltage to the armature winding, creates a step change in the gradient of the current in the armature winding, producing a damped vibration [7]. If the frequency of the commutation current, and hence the frequency of the induced impulse forces, have a frequency equal to or near the mechanical resonant frequency of the motor or to its supporting frames, then large mechanical vibration will be produced on the solid bodies.

Mechanically induced acoustic noise is due to mechanical imbalances, bad fitting of components, weak stator or rotor geometry in terms of poor mechanical stiffness, worn out ball bearings, etc. These imperfections allow mechanical structures or frames to vibrate and hence propagate acoustic noise.

Aerodynamic acoustic noise sources involve fluid flows around the motor and its supporting frames. When the motor were to run a fan load, then parameters such as fan blade tip speed, blade passing frequencies, turbulence etc. come into the equations. Each time a blade passes through a certain volume of air particles, that certain amount of particle vibrates, and hence propagates acoustic noise. Furthermore, as the rotor rotates, the volume of air gap between the stator and rotor changes periodically and therefore creates a periodic pressure variation. This change of pressure creates acoustic noise too. This phenomenon is known as the siren effect. From [8], the siren tone is defined as,

$$f_q = \frac{qz_b n_{rpm}}{60} [Hz] \text{-----} (1.2)$$

where z_b : number of fan blades; n_{rpm} : motor speed in [rpm]; q : 1,2,3... when $q=1$, f_i =blade passing frequency, whereas $q=2, 3...$ corresponds to siren tones.

Arranging fan blades with non-uniform blade pitches or angles, increasing the distance between fan blades and its surrounding frame can reduce the siren effect [8].

1.6 Weighting functions

The normal, healthy young adult is generally regarded to be sensitive to sounds having frequencies ranging from 20Hz to 20kHz typically. However, the loudness of the sound detected by the human ear varies with frequency. The human ear is more sensitive to certain frequencies, typically between 1kHz and 5kHz, i.e. the human ear hears it louder than other frequencies. The dynamic range of a normal young ear is considered to be from about -15dB to 150dB SPL. But, damage to the cochlea (a part of the ear which transduces mechanical vibration into neural impulses) may start to occur above 85dB [9].

Since the microphone used is to determine the effect of a sound on the human ear, an appropriate weighting has to be applied onto the sound detected by the microphone, so that it can closely represent the sensitivity of the human ear at certain frequencies. Figure 1.5 shows the internationally recognised weighting functions used for acoustic measurements, namely the A, B, C and D weighting functions.

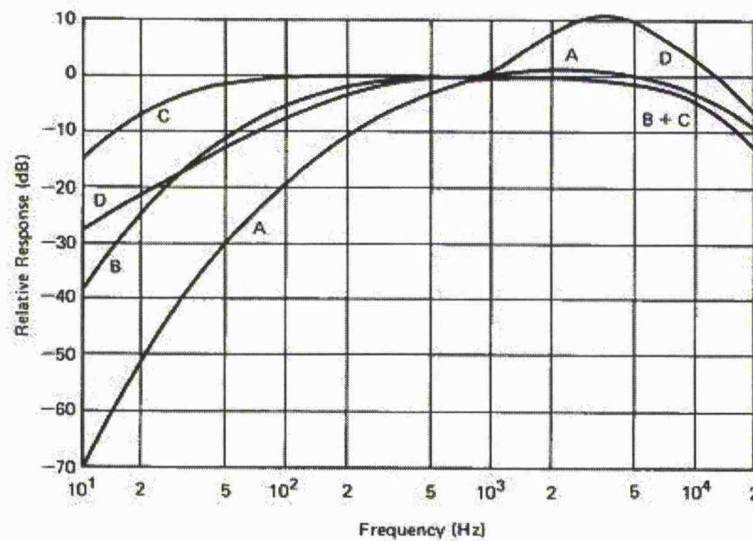


Figure 1.5: A-, B-, C- and D- weighting networks (Taken from [9])

The A-weighting is the most widely used weighting function to approximate the response of the human ear at low sound levels. Similarly, the B and C weighting functions were designed to approximate the response of the human ear at sound levels of 55-85dB and above 85dB respectively. The D weighting function has been proposed for aircraft noise measurements [9].

1.7 Behavior of the stator during vibration

Vibration mode shapes arise once the motor vibrates. Practically once a motor operates and vibrates, the vibration is a combination of lots of frequencies of different vibration mode shapes. However, any vibration frequency has its unique vibration mode shape. So-called mode numbers are given for a particular vibration mode shape. So, vibration modes are products of mechanical resonant frequencies.

Figure 1.6 shows the shapes of stator radial deflections for vibration modes of $m = 0$ to $m = 5$. Circumferential modes of vibration, $m = 1, 2, 3$ and 4 , are most important in small machines, where the circumferential mode of $m = 1$ can be predominant due to eccentricity of the rotor when the speed of operation is near the critical speed of the rotor [23].

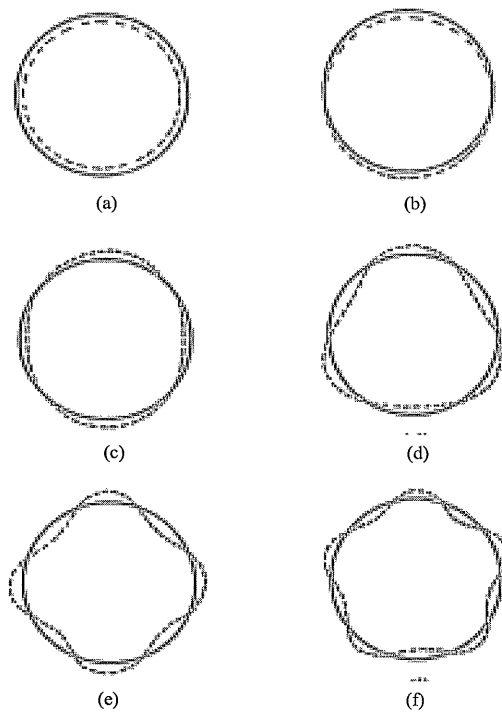


Figure 1.6: Circumferential vibration modes [23]

(a) $m = 0$; (b) $m = 1$; (c) $m = 2$; (d) $m = 3$; (e) $m = 4$; (f) $m = 5$

Adding to the complexity, there is also longitudinal vibration along the stator. Figure 1.7 shows the different modes of longitudinal vibrations, where the mode $n = 0$ is the most important [23].

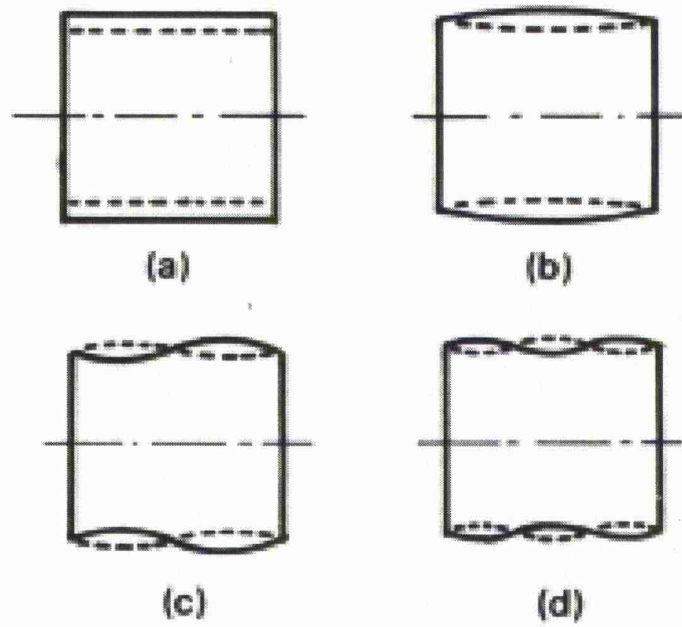


Figure 1.7: Longitudinal vibration modes [23]

(a) $n = 0$; (b) $n = 1$; (c) $n = 2$; (d) $n = 3$

Chapter 2

INVESTIGATION ON THE PERMANENT MAGNET BRUSHLESS DC MOTOR

2.1 Introduction

This chapter presents an investigation on acoustic noise produced by a 4-pole single-phase brushless DC (BLDC) of external rotor configuration driving a fan load. The BLDC was the first commonly used brushless electrical machines that have been favoured in commercial applications, due to its ability to provide better efficiency and, being brushless, eliminates brush noise and brush maintenance compared to the then DC motor. Therefore, this chapter gives a head-start into vibration investigations on brushless electrical motor with the investigation on a classical BLDC, and introduces a vibration reduction technique called the '3 stage commutation method' to try to suppress induced vibrations during commutation. Previous work has shown that changes in the voltage applied to a phase winding to drive the BLDC cause abrupt changes in the gradient of the flux waveform and result in motor vibration and acoustic noise. It was found that, the acoustic noise generated by the BLDC is similar to that by a switched reluctance motor [10] because both motors can induce a radial damped vibration due to current commutation. The investigation on the production and reduction of acoustic noise in switched reluctance motor has been on going in the recent years. Hence, acoustic noise analysis procedure and noise cancellation techniques on switched reluctance motors [7], [11] – [12] are referred in this report.

Dynamic tests and static tests were performed to investigate the noise and vibration of the motor, and results are presented. The 3-stage commutation method was then implemented to the switches in the power electronic inverter, using a 8-bit PIC microcontroller. Unfortunately, no significant noise cancellation was achieved at this stage. It was thought that the vibrations due to commutation were not the dominant source of the radiated acoustic noise.

2.2 Principle operation and converter topology

The operation principle for the 4-pole brushless DC fan system is described here. The fan used is a 12V-dc 3.2W 150mm Vent-Axia LoWatt Kitchen ventilation fan.

The brushless DC motor consists of bifilar windings wound on an internal 4-pole stator. The external 4-pole permanent magnet rotor carries a 5-blade impeller load. Figure 2.1 shows the schematic diagram of the internal stator bifilar windings. One winding is physically coupled on another. Figure 2.2 shows a diagram of the arrangements of the magnet on the external rotor.

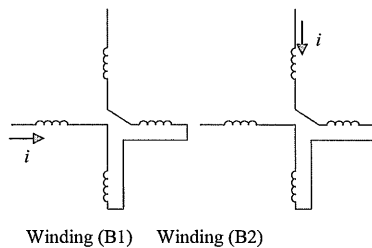


Figure 2.1: Schematic diagram of the internal stator bifilar windings

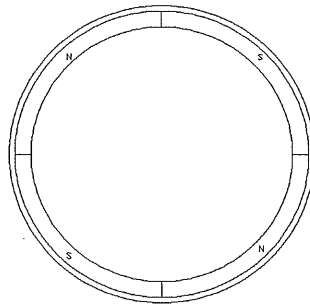


Figure 2.2: Permanent magnet external rotor

A Hall-effect sensor is used to detect the 4-pole permanent-magnet external rotor. The schematic of the power electronic converter used is shown in Figure 2.3. The sensor signal drives the switches SW1 and SW2 to energized one of the required bifilar windings. It requires 2 electrical sensor cycles to rotate 1 mechanical rotation of the rotor. When the switches are synchronized at the correct time with respect to the rotor position, continuous rotation is achieved.

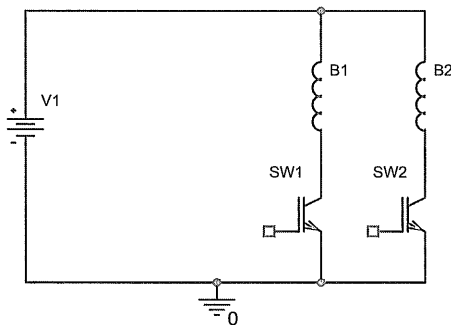


Figure 2.3: Schematic circuit diagram of the power electronic inverter drive.

B1: winding; B2: winding; V1: DC power supply

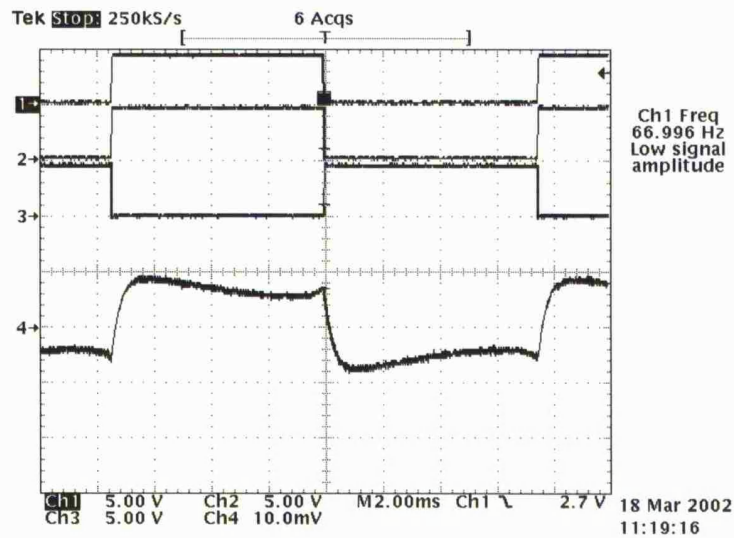
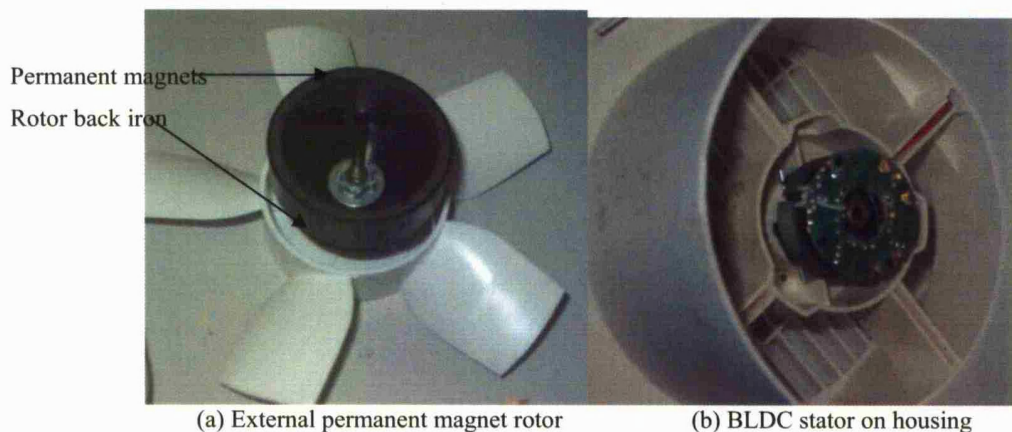


Figure 2.4: Waveforms at 2000rpm

CH1: Hall sensor; CH2: Switch 1; CH3: Switch 2; CH4: Current in motor winding (0.5A/div)

Figure 2.4 shows the current waveform and the switching waveforms while the motor was running at 2000rpm. The current decreases to zero at the point when the hall sensor changes its polarity, i.e. when the back-emf of one bifilar winding has changed its polarity. For positive torque to be produced, the current and back-emf have to be in-phase. Knowing that current cannot decrease to zero instantly due to the inductive nature of the windings, at the instant when the back-emf has changed polarity, the current is still having a non-zero value while starting to decrease to zero, and consequently negative torque can be produced. One way to avoid negative torque to be produced, is to turn off the switch earlier, i.e. before the hall sensor has changed polarity, allowing some time for the current to decrease to zero, and having the same zero-crossing point as the back-emf. Figure 2.5 below shows the picture of the brushless DC used.



(a) External permanent magnet rotor

(b) BLDC stator on housing

Figure 2.5: The permanent magnet brushless DC

2.3 The acoustic noise and vibration investigation

Measuring vibration and sound are very delicate tasks to perform. The sound of the experimenter sighing, the cooling fan noise from other instruments in the test cell etc., could be picked up by the microphone in used, even the noise of opening and closing of doors just outside the test cell can be detected. Vibration of another machine running on the same platform as the machine under investigation can be picked up as well by the accelerometer used. Hence, it is desirable to isolate the investigation environment as much as possible, so that the detection of noise or vibration of other sources is minimized or eliminated.

The accelerometer used for measuring vibration on the surface of the machine has an output sensitivity of 49.7mV/ms⁻² or 197.394394ms⁻²/V, where its natural frequency is 47.5kHz and weighs 30g. The output was then pre-amplified by 20dB before connected to an oscilloscope.

The microphone used for measuring sound pressure has an output sensitivity of 64.6mV/Pa or 15.47987616Pa/V, and having a flat frequency response within ±2dB up to 20kHz.

During the investigation of noise, both time-domain and frequency domain of the noise were explored. The sound pressure level (SPL), L_{spl} , is used to calculate the level of noise pressure of a certain frequency detected by the microphone. The SPL has the expression

$$L_{spl} = 20 \log \frac{P}{P_{ref}} [dB] \text{-----} \quad (2.1)$$

The A-weighting has been chosen to be used in the work described in this thesis, due to its wide recognition by other acoustic engineers. The typical A-weighting function, shown in Figure 2.6, is then applied to the sound pressure detected by the microphone in the post-processing stage in MATLAB.

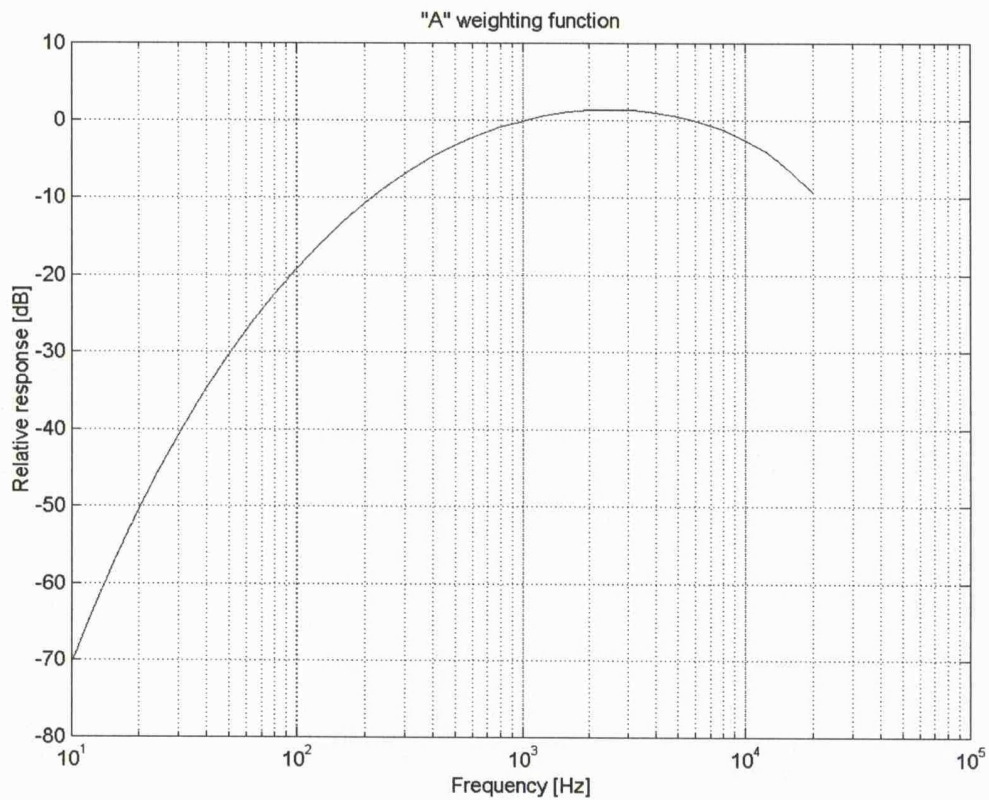


Figure 2.6: A-weighting network applied in MATLAB obtained from [9]

The post-processing approach of the acoustic noise will be outlined in Appendix B, where the raw data is post-processed in MATLAB.

Suppose now the sound pressure level of a certain frequency, f , is obtained using equation (2.1), and denoted as $L_{spl,f}[dB]$, then after applying A-weighting on it, its corresponding A-weighted sound power level will be denoted as

$$L_{dBA, f} = L_{spl, f} + L_{A, f}[dBA] \text{ ----- (2.2)}$$

where $L_{A,f}$ is the relative sound pressure level obtained from Figure 2.6 at frequency f . The unit $[dBA]$ is associated with the sound pressure level with A-weighting applied.

2.4 Experimental tests

The dynamic test was performed with the 5-blade fan load at a DC voltage of 13V, running the motor at 2000rpm.

A fan blade passing frequency of about 168Hz was expected to be detected in the acoustic noise spectrum. The acoustic noise was recorded as shown in Figure 2.7.

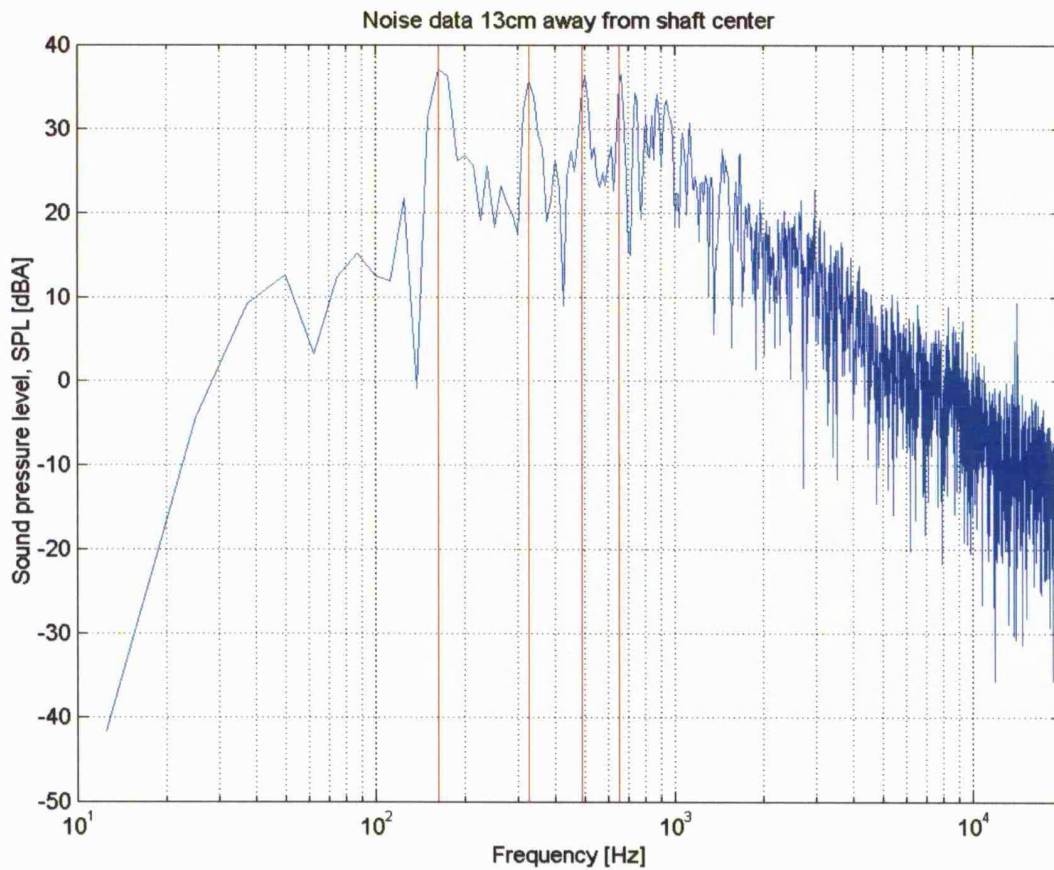


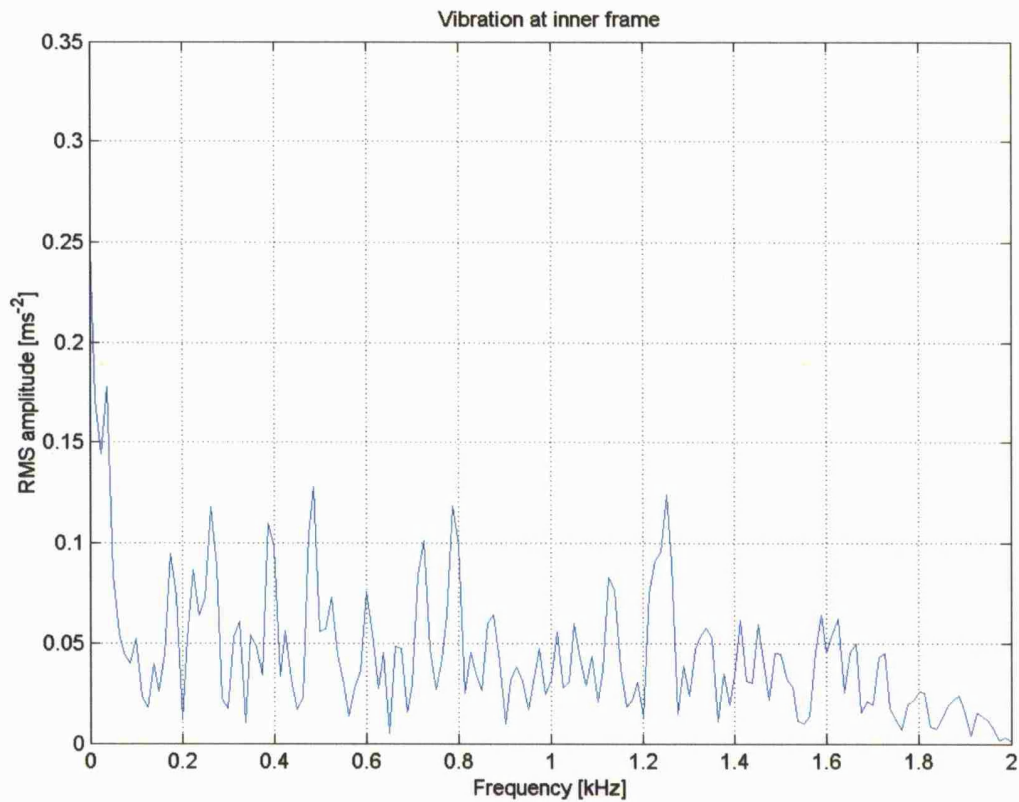
Figure 2.7: Acoustic noise frequency spectrum under load at 2000rpm.

Microphone placed around 13cm from shaft center.

From Figure 2.7, it was obtained that the fan passing frequency of 168Hz dominates the acoustic noise spectrum. Other frequency components in Figure 2.7 are the harmonics of the fan blade passing frequencies as indicated by red lines.



(a)



(b)

Figure 2.8: Vibration FFT at 2000rpm on inner frame

While the motor was running at 2000rpm, the vibration was measured on the inner frame, shown in Figure 2.8(a) at point H1 which is the closest place where the vibration of the stator could be measured, a vibration frequency of around 500Hz was detected as shown in Figure 2.8(b). This suggests that a radial vibration of electromagnetic origin could have induced the 500Hz vibration

component on the inner frame, and consequently induced one of the acoustic noise component of around 500Hz shown in Figure 2.7.

Hence, a static vibration test was performed to further investigate if the vibration component of around 500Hz is one of the mechanical resonant frequencies of the inner frame. Figure 2.9 shows the schematic diagram to perform the static vibration test. As shown, only one of the stator phase winding is energized.

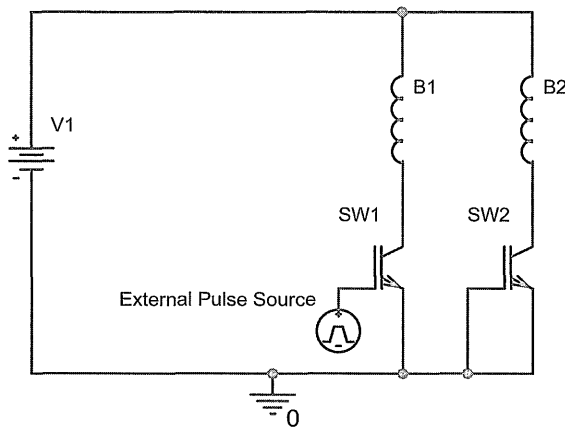


Figure 2.9: Schematic diagram to perform static vibration test

The rotor was locked at its stable equilibrium position. The stable equilibrium position of the rotor, is the position the permanent magnet rotor rests when no stator winding is energized. A pulse with pulse width of 20.4ms was supplied to one of the switches by a signal generator, in order to feed current pulses of 0.5A peak into the motor windings. 0.5A peak was fed because the running instantaneous current at 2000rpm, shown in Figure 2.4, was able to reach at about 0.5A peak.

It should be noted that, at each pulse of current, a vibration is induced on the stator. Hence, it is good practice to have a long time transition between current pulses to allow the vibration die away before inducing another vibration.

Figure 2.10 shows the switching pulse, current pulse in one of the windings and vibration at point H1. From the static test, a natural vibration frequency of 500Hz was identified.

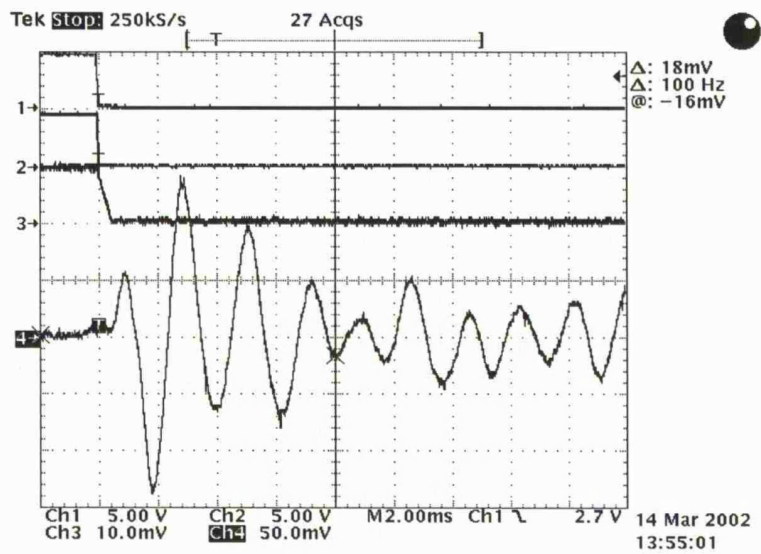


Figure 2.10: Static vibration test with rotor locked at stable equilibrium position
 CH1: Input pulse; CH2: Switch waveform; CH3: Winding current waveform (0.5A/div)
 CH4: Resonance at fan housing at point H1

Figure 2.10 shows that a radial vibration on the fan housing induced one of the acoustic noise components. This also verifies that a radial, damped vibration was induced at the commutation of the current. Only the vibration due to the falling edge of the current is of concern, because at this falling edge the vibration is the largest [7].

2.4.1 The '3-stage' commutation method

Next, the 3-stage commutation was applied to the falling edge of the switch to attempt to eliminate the 500Hz vibration component shown in Figure 2.10. The 3-stage commutation was programmed in the PIC to cancel the 500Hz vibration.

Noise cancellation using the 3-stage commutation method has been successful in [11]. The objective is to suppress currents that do not produce torque, but instead produce radial vibration between that stator and rotor during commutation. According to [11], after extensive trial and error, it has been found that for the cancellation to be most effective, the 3-stage commutation method has to be implemented in the following procedure:

- (i) First Stage – opening one of the switches at the point of initial commutation to produce a first vibration in which the acceleration is initially negative
- (ii) Second Stage – After $\frac{3}{20}$ of the period of the vibration to be cancelled, closing the initially opened switch to re-apply the positive voltage to the phase winding, thus increasing the radial force again and producing an acceleration which is in opposition to the negative acceleration of the first stage
- (iii) Third Stage – After $\frac{4}{20}$ of the period of the vibration to be cancelled, the switch closed during the second stage is opened again applying negative volts to the phase winding, decreases current to zero, and produce a final vibration which will be in opposition to the vibration produced in the second stage.

The '3-stage commutation method' with the suggested time intervals were implemented using PIC microcontroller programming.

The 3-stage commutation was done on the falling edges of the switches during the static vibration test. Resonant results before and after implementing the 3-stage commutation on the falling edges of the switches are shown in Figure 2.11 and Figure 2.12 respectively.

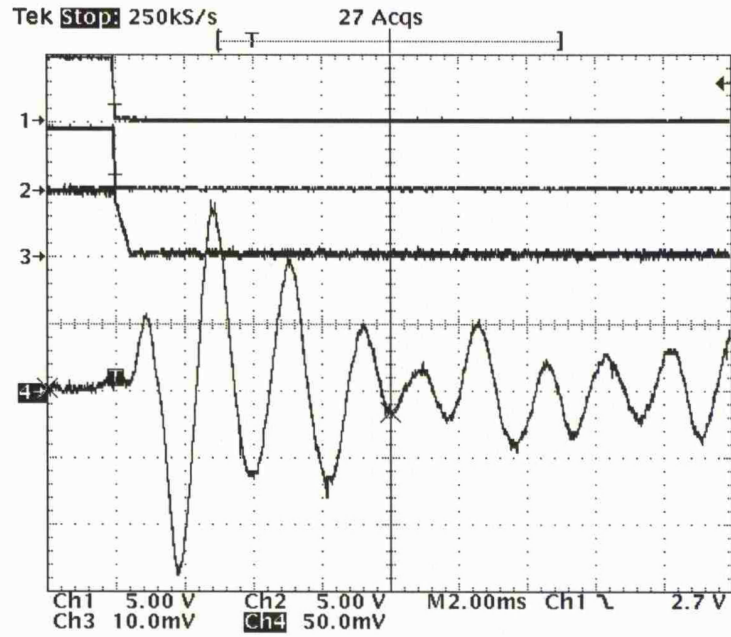


Figure 2.11: Static vibration test with rotor locked at aligned, stable equilibrium position before 3-stage commutation

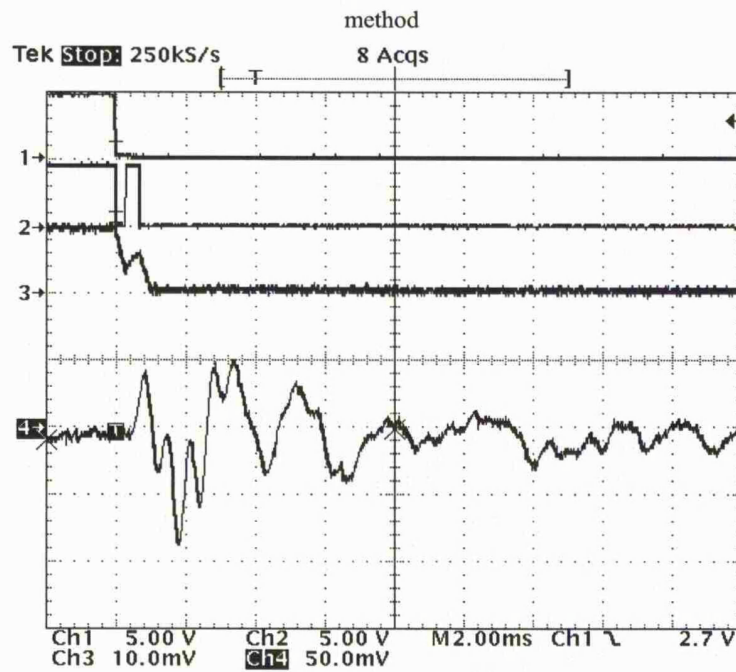


Figure 2.12: Static vibration test with rotor locked at aligned, stable equilibrium position after 3- stage commutation

CH1: Hall sensor; CH2: Switch; CH3: Current in winding (0.5A/div); CH4: Vibration at point H1

The 3-stage commutation method did attenuate the 500Hz component of vibration on the case of the fan, but instead of leaving no vibration, a higher frequency emerged at a lower magnitude.

Then, the method was implemented on the switches while the motor was driven at 2000rpm. Waveforms before and after implementing the 3-stage commutation method are shown in Figure 2.13 and Figure 2.14. The acoustic noise results are shown in Figure 2.15. The current waveform after the 3-stage commutation method implementation was rising slower, indicating that the implementation was applied when the back-emf was high. This was because the turn-on angle was delayed due to the lengthened turn off angle in order to implement the 3-stage commutation method.

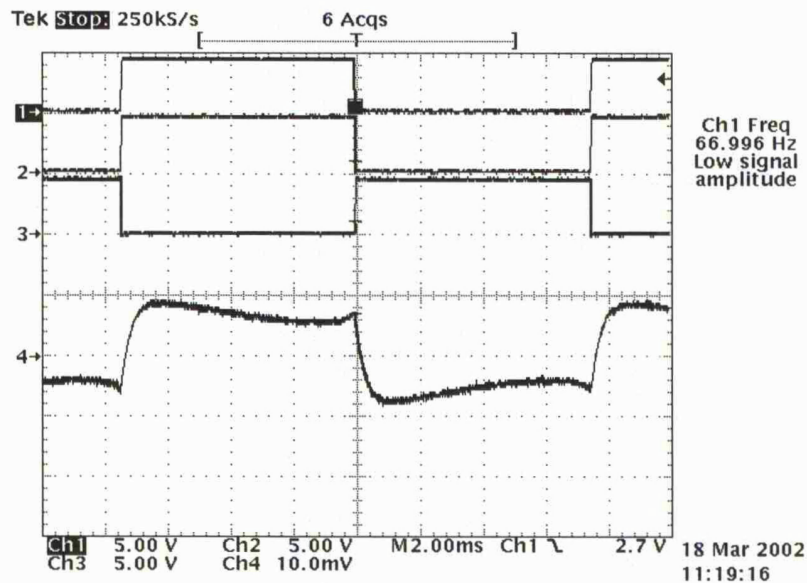


Figure 2.13: Waveforms before 3-stage commutation method

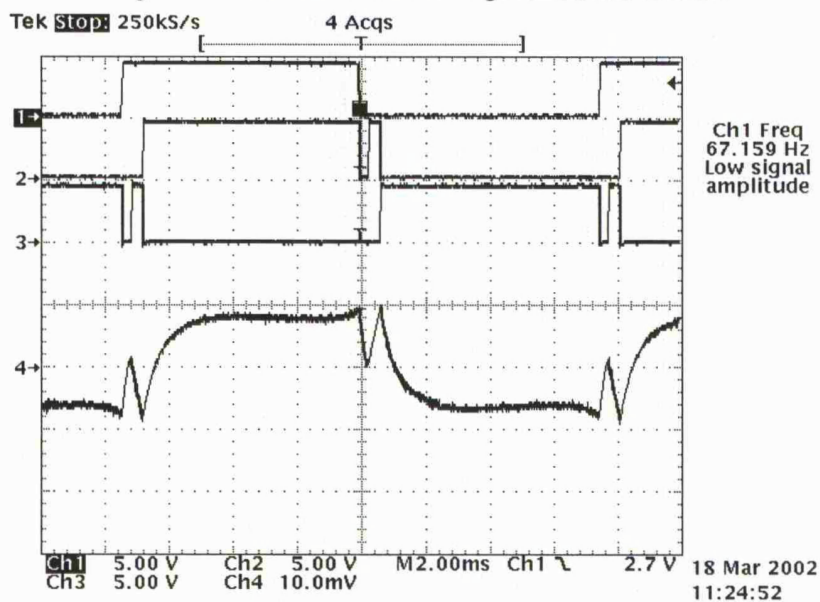


Figure 2.14: Waveforms after 3-stage commutation method

CH1: Hall sensor; CH2: Switch 1; CH3: Switch 2; CH4: Current in motor winding (0.5A/div)

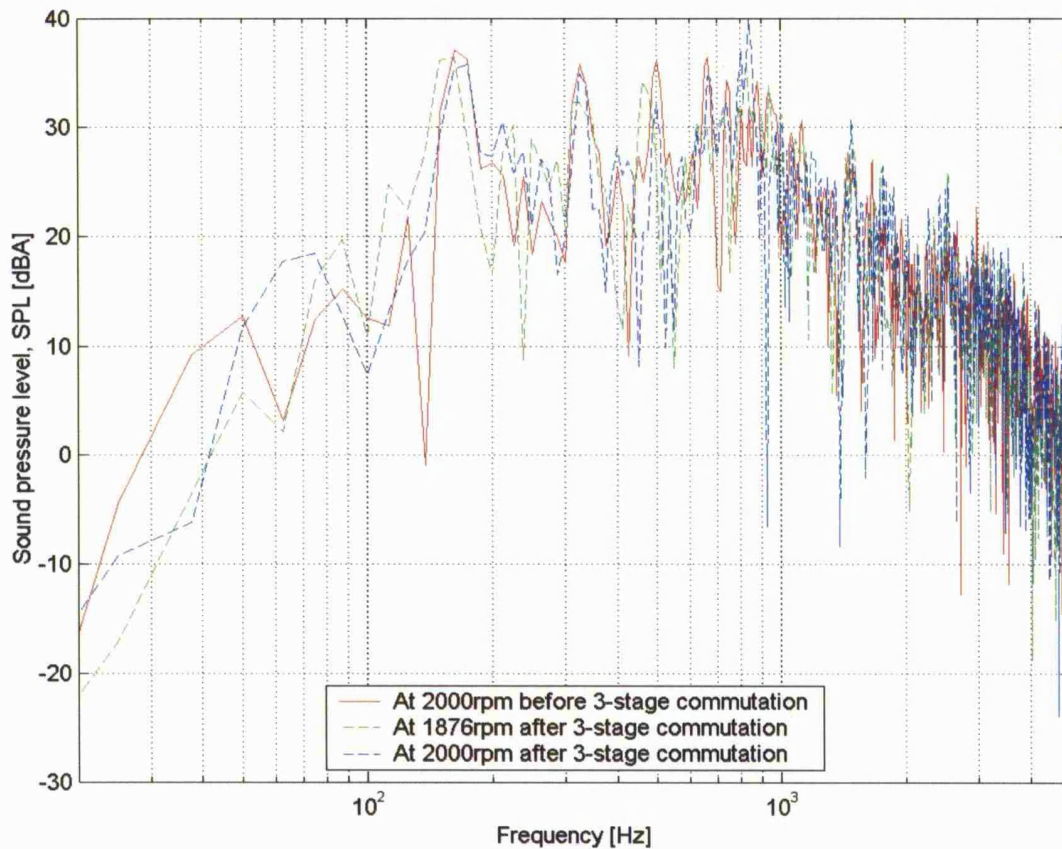


Figure 2.15: Acoustic noise frequency spectrum

It was observed that the acoustic noise is motor speed dependent. Implementation of the 3-stage commutation caused the motor speed to drop to about 1876rpm. The voltage was increased to restore the speed to 2000rpm. Notice that in Figure 2.15, the 500Hz noise component was shifted to the left as the motor speed decreased (green dashed line) when the cancellation was initially applied. As the motor speed was increased back to 2000rpm, the 500Hz noise component still remains detected (blue dashed line) but at a lower magnitude.

Unfortunately, from the subjective point of view, the overall acoustic noise was not cancelled or even reduced. The 3-stage commutation method had no effect in canceling noise significantly when the motor was running.

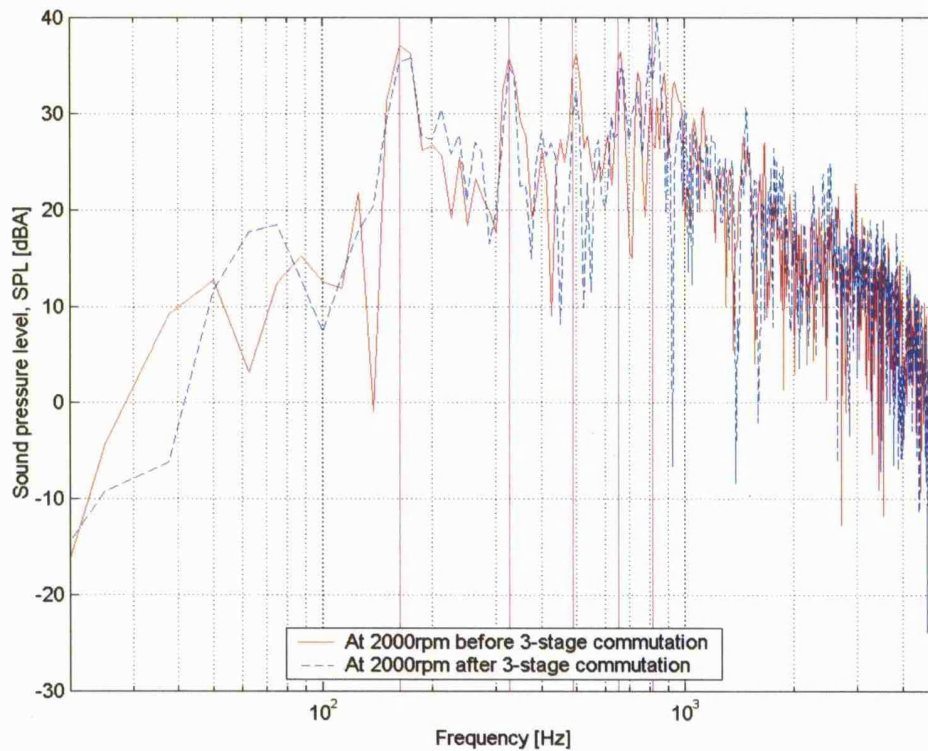


Figure 2.16: Noise frequency domain with estimated siren tone harmonics at 2000rpm.

The first magenta line from the left indicates the blade passing frequency.

As shown in Figure 2.16, the 500Hz noise component had only a very slight reduction with the 3-stage commutation method applied. The 3-stage commutation method was not effective in canceling the 500Hz noise component because it was dominated by its aerodynamic origin where it was the 3rd harmonic of the fan blade passing frequency shown by the magenta lines in Figure 2.16.

2.5 Summary

In conclusion, the 3-stage commutation method was not effective enough to cancel a noise component of 500Hz which was believed to have been induced due to electromagnetic origin while the motor was running, because that component was dominantly of aerodynamic origin, namely the harmonic of the fan blade passing frequency as shown in Figure 2.16. Furthermore, the permanent magnet might have also been the dominant source of magnetic force that could induce dominant vibration on the stator, which can not be suppressed by applying the 3-stage commutation method on the armature current, since this source of magnetic force did not come from the applying of current in the windings. Authors in [13, 14, 15] have investigated the origins of vibration due to permanent magnets, and the effects of the geometry of permanent magnets to reduce vibration, and reducing radial magnetic forces. However, Figure 2.11 and Figure 2.12 presented results which showed that the method of commutation can have an impact on the vibration of motor components.

Chapter 3

VIBRATION AND ACOUSTIC NOISE INVESTIGATION ON THE FLUX SWITCHING MOTOR

3.1 Introduction

Work has been brought forward to determine the mechanical resonant frequency of both a round-shaped Flux Switching Motor (FSM) used in a lawnmower, and a polygon-shaped FSM for a vacuum cleaner, where both motors have the internal rotor configuration. Experiments were performed by performing static vibration tests and dynamic tests. Being able to determine the mechanical resonant frequency of a particular stator lamination will provide useful information on what motor speed the motor should avoid operating on, because if a motor speed or its harmonic components is near or equal to the motor's mechanical resonant frequency, it will eventually induce mechanical resonance, which can cause severe structural damage to the motor. Work done in this chapter will compliment the preceding chapter that will introduce a mechanical finite element and algebraic analysis to predict the mechanical resonant frequency of both the round-shaped and polygon-shaped FSM.

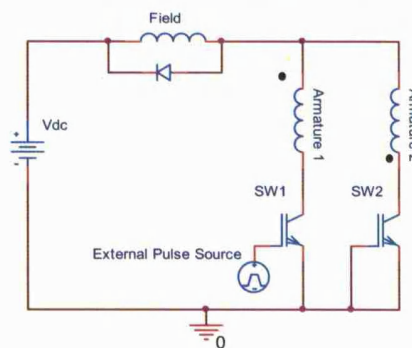
Apart from finding out the mechanical resonant frequency of the stator laminations, the acoustic noise produced while the motors were running was also investigated. The source of acoustic noise of the round-shaped FSM was believed to be the housing of the motor that was propagating the noise, as the vibration frequency of the housing was near the noise frequency. An attempt to eliminate the high-frequency whistling noise produced by the polygon-shaped FSM was made. It was believed that, a high-frequency short voltage pulse during commutation was the main source of the high-frequency whistling noise while the motor was running at any speed. Furthermore, during the vibration measurement at any speed, it is possible to determine certain motor speeds that should be avoided to prevent the harmonics of the motor speed from exciting the speed-independent vibration frequency components. A conclusion was made that this whistling noise was related to 2 forms of aerodynamic sources, namely the fan blade passing frequency and siren noise.

3.2 Investigation on the round-shaped flux switching motor

The investigation on determining the mechanical resonant frequency of the round-shaped FSM was done by performing the static vibration test and then the dynamic test. The accelerometers and microphones used are as described in section 2.3.

3.2.1 Static vibration test

A schematic diagram shown in Figure 3.1(a) was used to perform the static vibration test with the 2-pole rotor locked aligned along positions 1 and 5 in Figure 3.2(b), and positions 3 and 7 in Figure 3.4. A 5V pulse, with pulse-width of 67.2ms and a pulsing frequency of 1.16Hz was applied to only one switch. This created a pulsating dc current applied to only one of the fully-pitched windings. A damped vibration is induced at each falling edge of the current in the winding. The low pulsing frequency is to ensure that the previous vibration dies away before inducing the next vibration. An accelerometer was used to measure the vibration frequency of the stator by moving it around the circumference of the stator. Refer to Figure 3.2(b) for the accelerometer positions. No measurements were taken from positions 2, 4, 6, and 8 because the existing pillars holding the housing, as shown in Figure 3.2(a), prohibited the placing of the accelerometer. Consequently, one of the asymmetrical vibration mode of 2, shown in Figure 4.3(a), could not be measured.

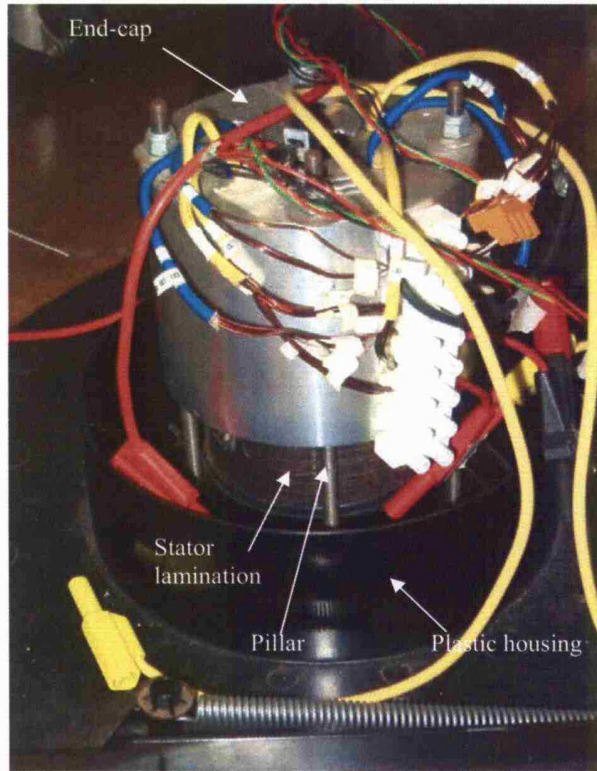


(a)

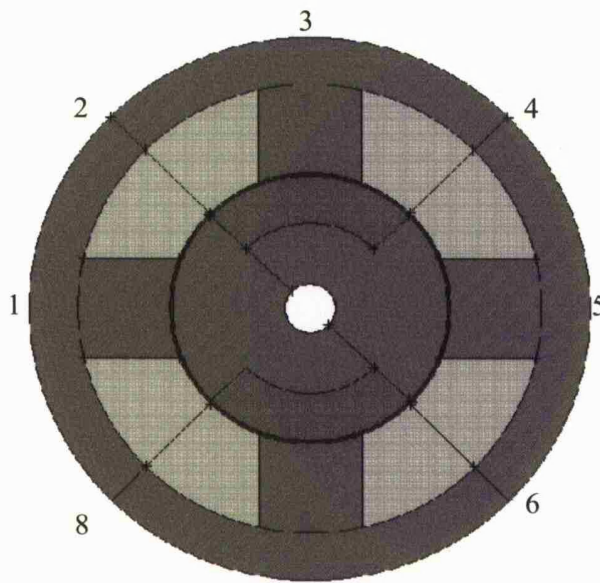


(b)

Figure 3.1: Schematic diagram for static vibration test



(a) Photo of motor



(b) Vibration measuring points

Figure 3.2: Round-shaped flux switching motor

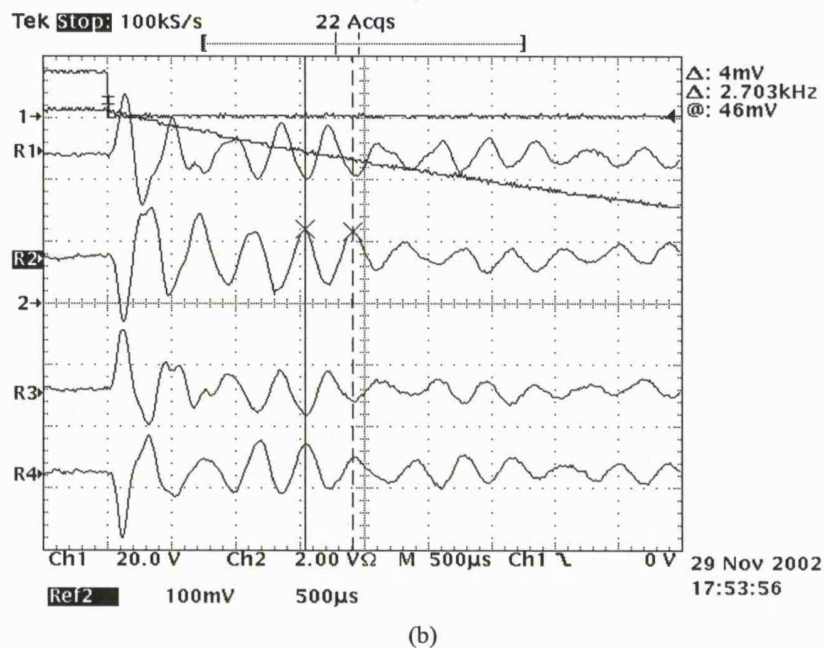
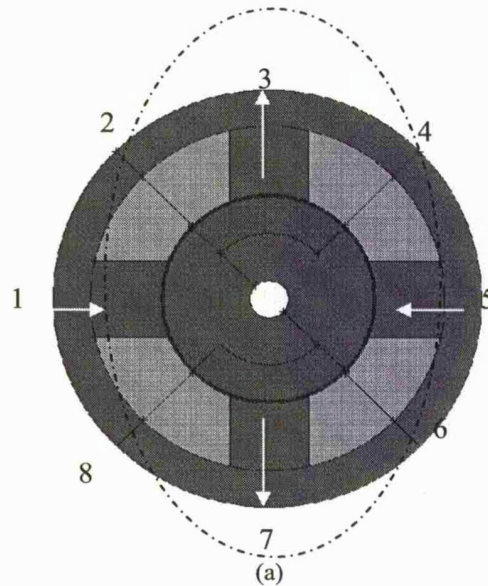


Figure 3.3: Vibration signals when rotor aligned in position 1 and 5
 CH1: Switch pulse; CH2: winding current (2A/div); R1: vibration at position 1;
 R2: vibration at position 3; R3: vibration at position 5; R4: vibration at position 7

It can be concluded from Figure 3.3(b) that an average frequency of about 2.7kHz is the dominant mechanical resonant frequency of the stator. Furthermore, one pair of vibration waveforms, R1 and R3, are vibrating in-phase with each other, so as for the other pair of vibration waveforms, R2 and R4, at any instant in time. However, these 2 pairs of vibration waveforms, vibrate out-of-phase from each other at any instant in time. Assuming that a positive acceleration results an outward displacement, and a negative acceleration results an inward displacement, the

arrows in Figure 3.3(a) depicts the vibration mode at an instant in time when displacement is the largest.

Then, the rotor was turned to align along the positions 3 and 7, shown in Figure 3.4.

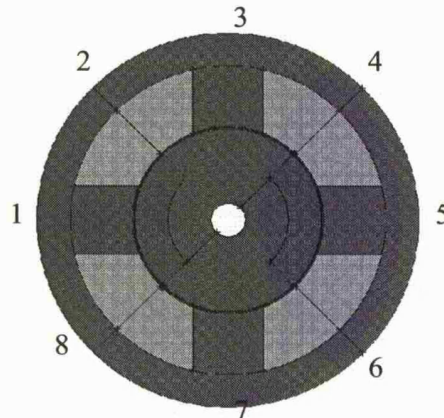


Figure 3.4: Vibration measuring points

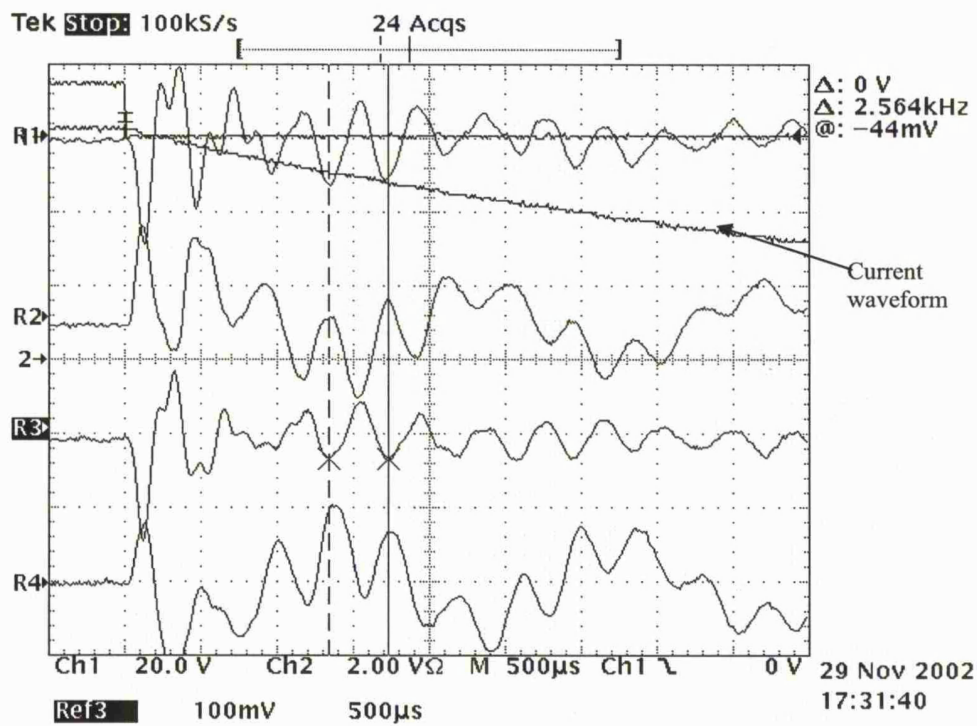
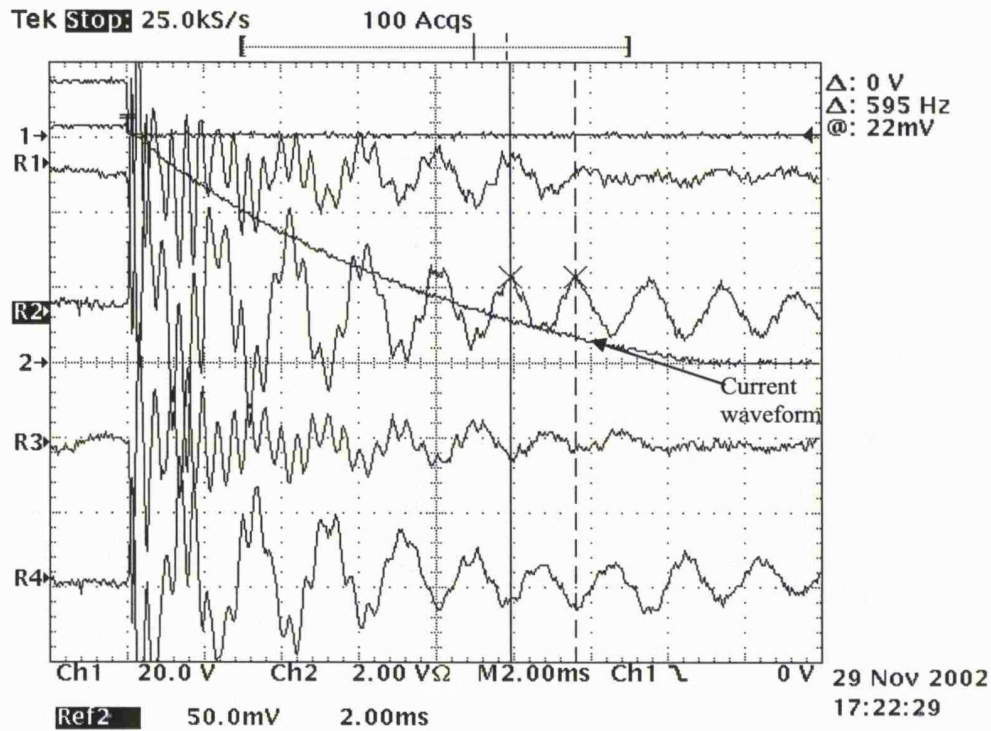


Figure 3.5: Vibration signals when rotor aligned in position 3 and 7

CH1: Switch pulse; CH2: Current pulse(2A/div); R1: vibration at position 1; R2: vibration at position 3;
R3: Vibration at position 5; R4: Vibration at position 7;

From Figure 3.5, the resulting vibration mode shape is still $m=2$ of an average of 2.5kHz.



(a) CH1: Switch pulse; CH2: Current pulse(2A/div); R1: vibration at position 1; R2: vibration at position 3; R3: Vibration at position 5; R4: Vibration at position 7;

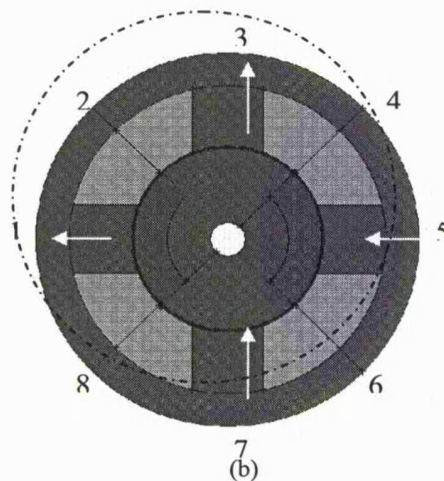


Figure 3.6: Vibration signals when rotor aligned in position 3 and 7

Apart from detecting a vibration of an average resonant frequency of 2.5kHz as shown in Figure 3.5, a vibration of an average resonant frequency of 500Hz was also detected as shown in Figure 3.6(a). It suggests that the vibration of 500Hz has a corresponding mode shape of $m=1$ [23], as shown in Figure 3.6(b), because the waveforms suggest that, at any instant in time, 2 pairs of adjacent stator teeth vibrate in the same direction, an adjacent pair displaced outwards, while another adjacent pair displaced inwards. This mode $m = 1$ appeared could probably be due to the

motion of the whole system and not the stator, since the whole system, as shown in Figure 3.1(b), was not tightly constraint and was on wheels.

3.2.2 Dynamic tests

The motor under investigation was driven by a two phase variable-frequency drive. Both the field and armature windings were fed with sinusoidal 2-phase currents of 20A peak-to-peak, producing a rotating magnetic field in the stator lamination. The rotor then turns in synchronism with the rotating magnetic field. The motor was run at 1800rpm. The vibration modes and frequency, as well as the acoustic noise spectrum were obtained from this experiment. Refer Figure 3.4 for the vibration measuring positions.

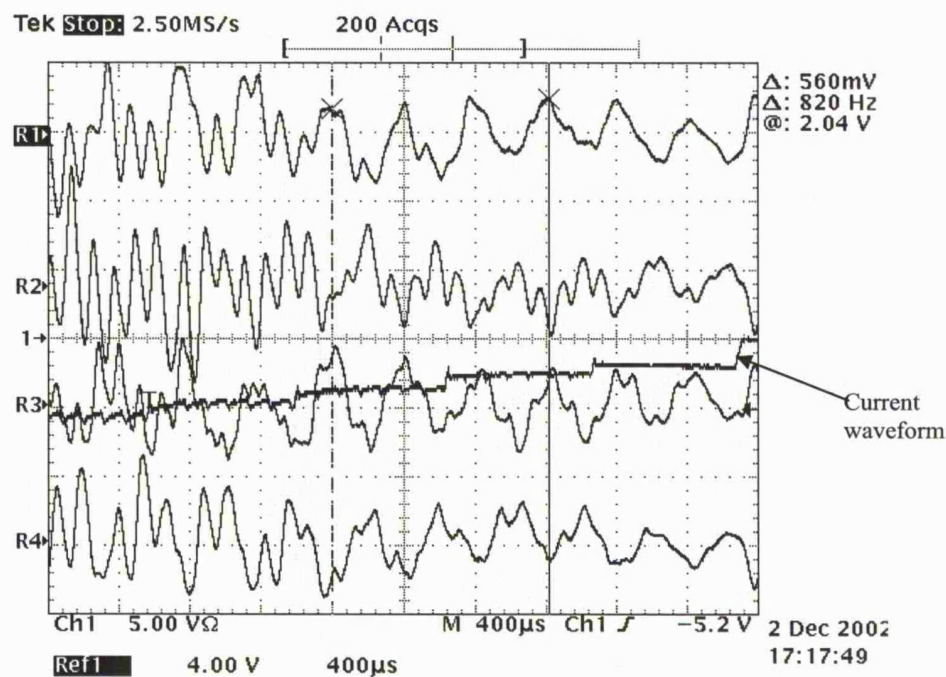


Figure 3.7: Vibration on stator at 1800rpm

CH1: armature current waveform (5A/div); R1: vibration at position 1; R2: vibration at position 3;
R3: vibration at position 5; R4: vibration at position 7;

It can be concluded from Figure 3.7 that, an average vibration frequency of around 2460Hz (shown by cursor) dominates at 1800rpm. The vibration mode shape at this frequency was determined to be $m=2$, as it can be seen from Figure 3.7, because the trace of R1 is in-phase with R3, R2 in-phase with R4, but the pairs of waveforms R1 and R3 are 180° out-of-phase from R2 and R4 at any instant in time. This approach is also illustrated in [16].

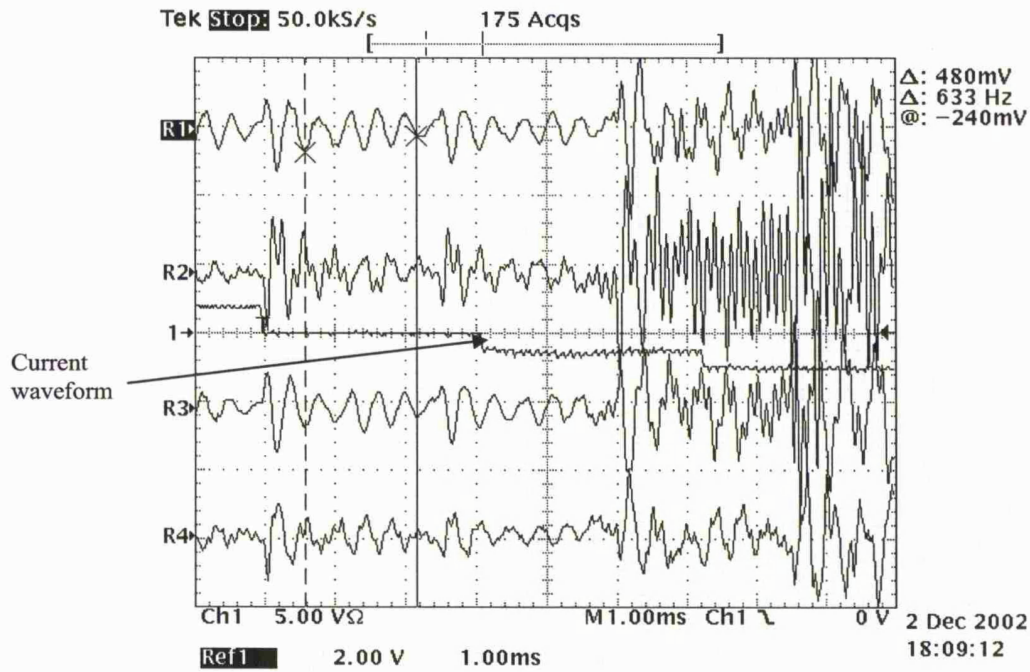


Figure 3.8: Vibration on stator at 480rpm

CH1: armature current waveform (5A/div); R1: vibration at position 1; R2: vibration at position 3;
R3: vibration at position 5; R4: vibration at position 7;

Changing the motor speed to 480rpm, an average vibration frequency of around 2532Hz (shown by cursor in Figure 3.8) was detected. Again, a vibration mode shape of $m=2$ was confirmed. It can be concluded that, a resonant frequency of an average frequency value of 2496Hz of vibration mode 2 exists. Higher frequencies shown in both Figure 3.7 and Figure 3.8 are due to the current chopping frequency of the controller. The current chopping frequency becomes significant when the current level is gradually increasing in magnitude.

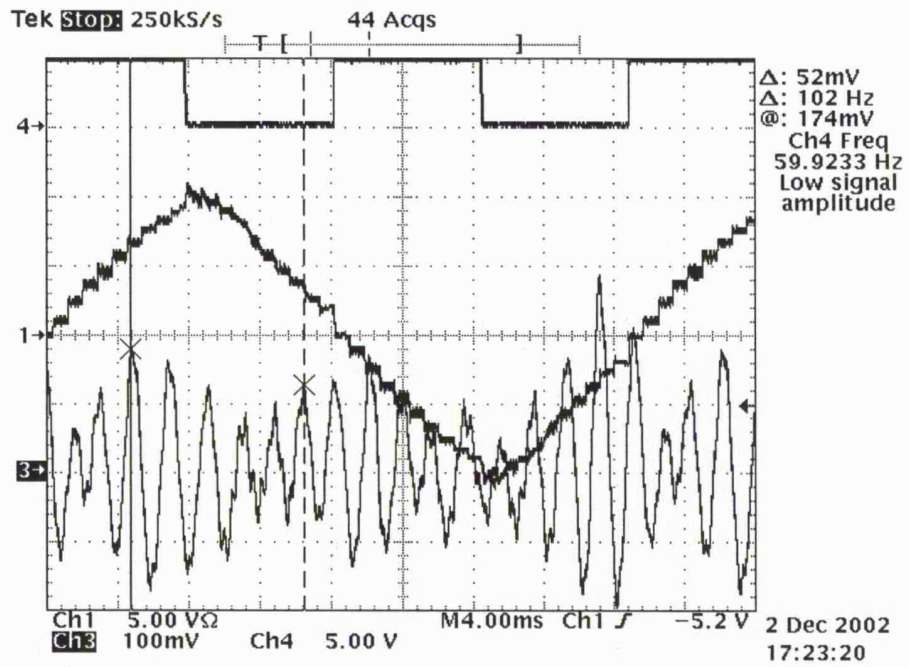


Figure 3.9: Acoustic noise at 1800rpm measured about 15cm away from stator
 CH1: Armature current waveform (5A/div); CH3: Noise waveform; CH4: Rotor position sensor

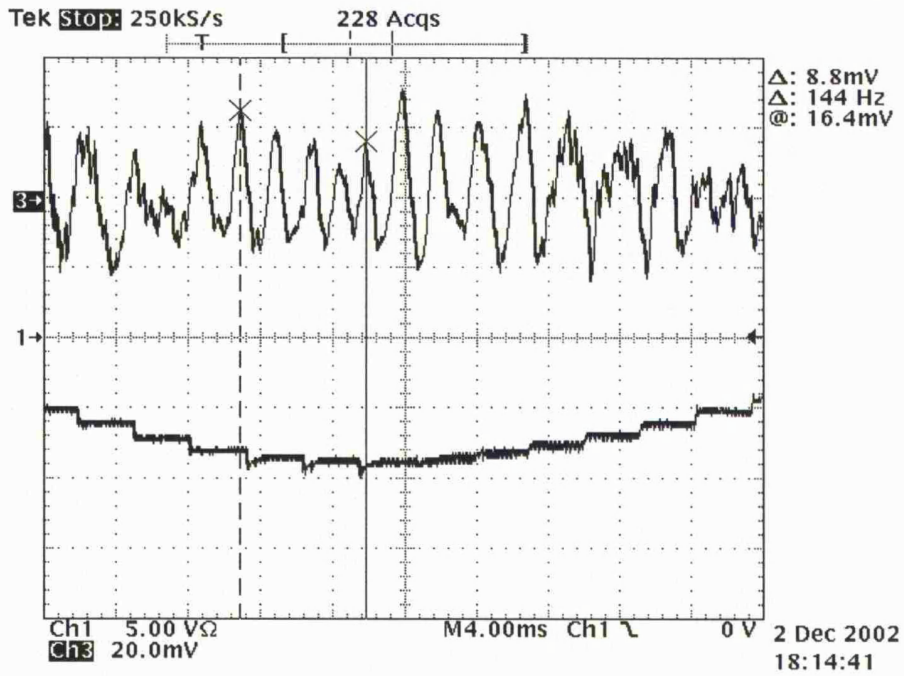


Figure 3.10: Acoustic noise at 480rpm measured about 15cm away from stator
 CH1: Armature current waveform (5A/div); CH3: Noise waveform

Figure 3.9 shows the acoustic noise waveform while running the motor at 1800rpm, measured from about 15cm away from the stator. It can be seen that the acoustic noise at this running speed is

dominated by an average noise frequency of around 510Hz frequency component (shown within cursors). When the speed was decreased to 480rpm, from Figure 3.10, the same dominant average noise frequency of around 576Hz frequency component remained. This was to show that the dominant noise frequency of average noise frequency does not depend on speed.

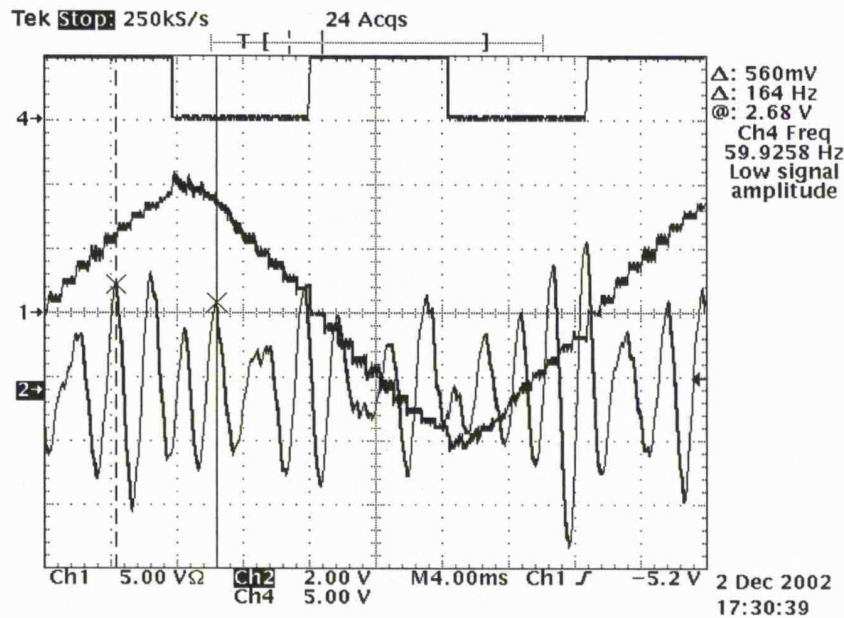


Figure 3.11: Vibration at circular frame at 1800rpm

CH1: armature current waveform (5A/div); CH2: vibration waveform; CH4: Sensor signal

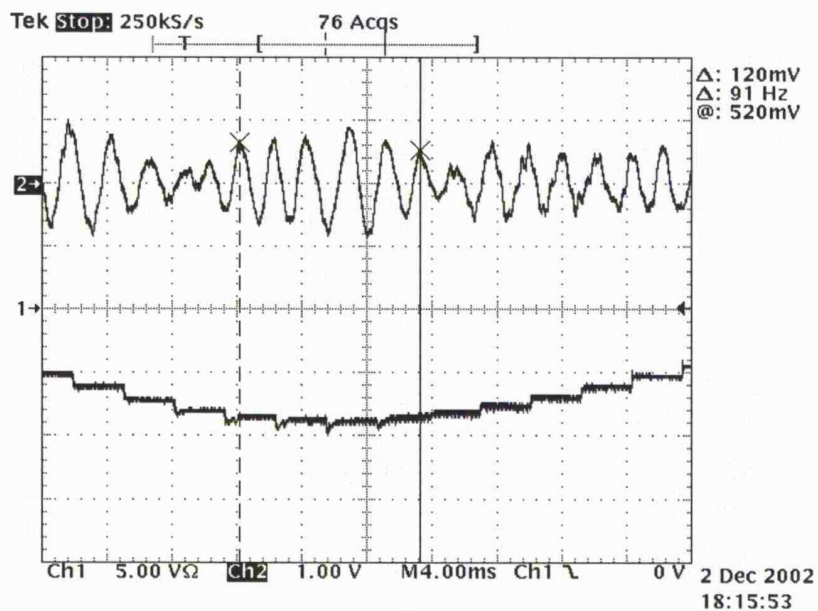


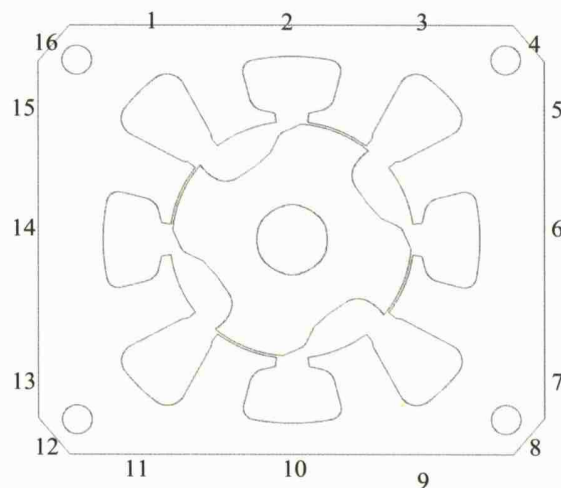
Figure 3.12: Vibration at circular frame at 480rpm

CH1: armature current waveform (5A/div); CH2: vibration waveform;

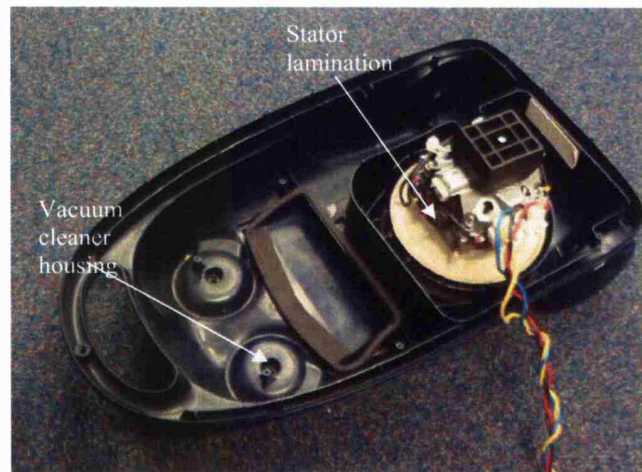
The 510Hz acoustic noise component at 1800rpm was traced to the circular frame that surrounds the stator. The circular frame vibrated with maximum amplitude of average frequency of around 492Hz (shown between cursors) as shown in Figure 3.11 and Figure 3.12. This suggested that the circular frame could be the source of the 510Hz noise component.

3.3 Investigation on the polygon-shaped flux switching motor

Similar experimental tests as performed on the round-shaped FSM were done on the polygon-shaped FSM. Vibration was measured using an accelerometer on 16 points around the polygon-shaped lamination, and recorded. These 16 points are shown in Figure 3.13(a). The investigation was done with the stator lamination sitting on its housings, as shown in Figure 3.13(b).



(a) 16 Vibration measurement points

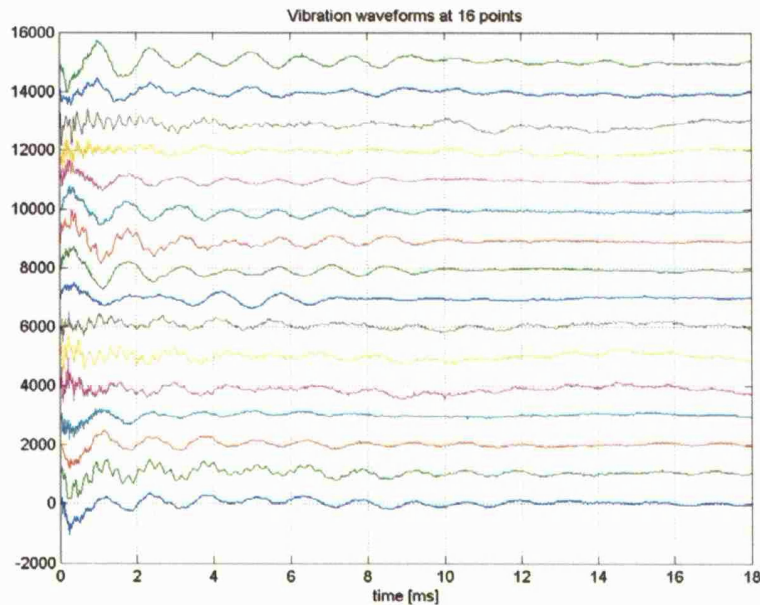
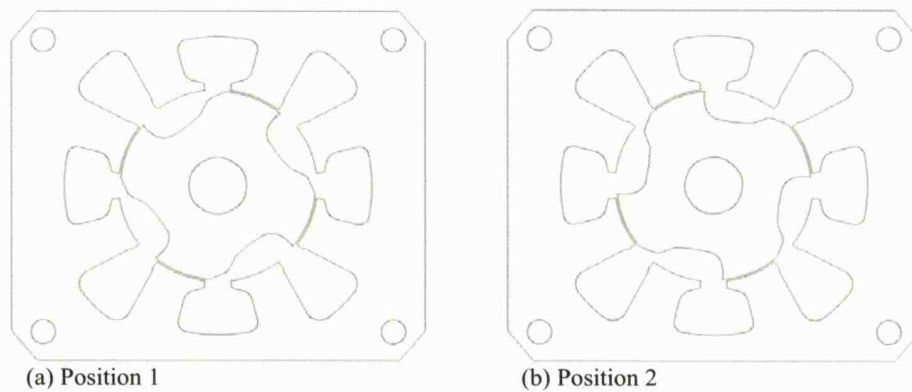


(b) the vacuum cleaner with polygon-shaped flux switching motor

Figure 3.13: Polygon-shaped flux switching motor

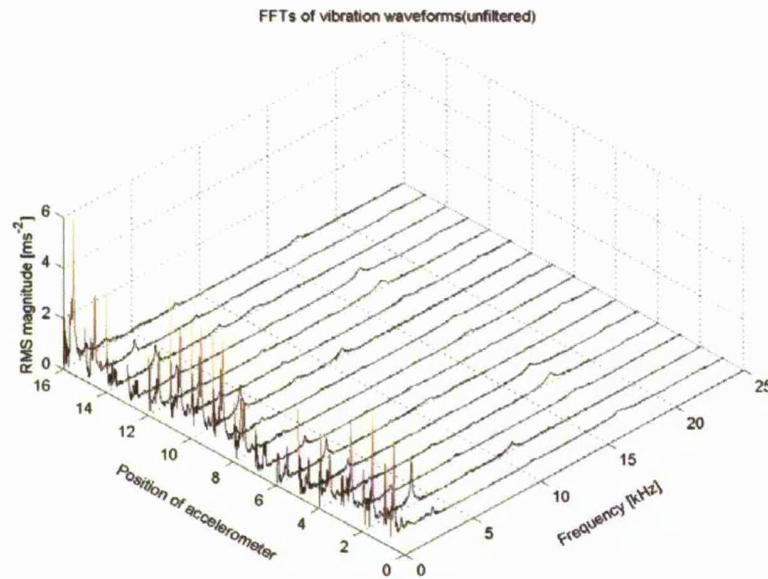
3.3.1 Static vibration test

The same power electronic circuit configuration shown in Figure 3.1 was used to perform the static vibration test. A pulse dc current was fed into one of the armature windings with the 4 pole rotor fixed in 2 aligned positions, i.e. rotor poles and stator poles overlap, as shown in Figure 3.14(a) and (b), referred as position 1 and 2 respectively. Each pulse of current in the armature induces a vibration on the stator. The pulse frequency has to be low enough in order to have the induced vibration die away before the next vibration is induced. All the vibration results were then post-processed in MATLAB, with some filtering applied. Both test positions gave the same results, so only the results with the rotor at position 1 are shown here.



(c) Unfiltered vibration waveforms. Waveform amplitudes not to scale. Waveform from bottom to top corresponds to accelerometer position 1 to 16 respectively.

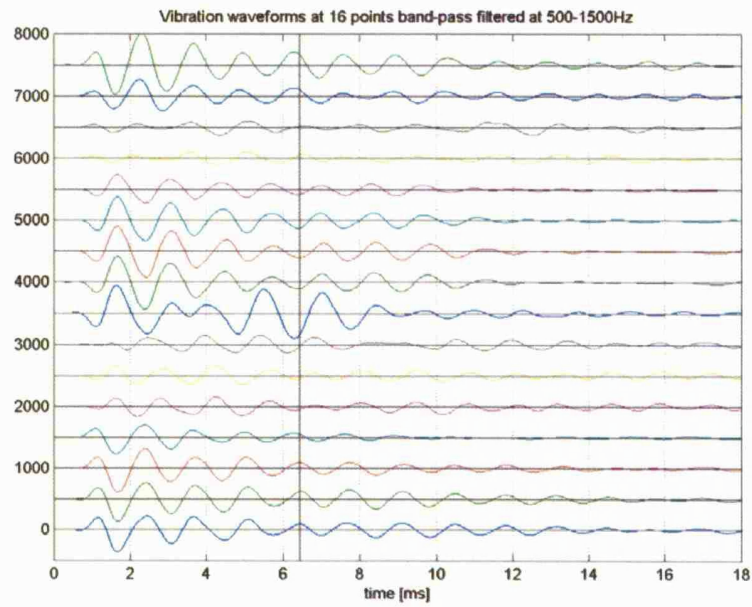
Figure 3.14 : Static vibration test on polygon-shaped flux switching motor



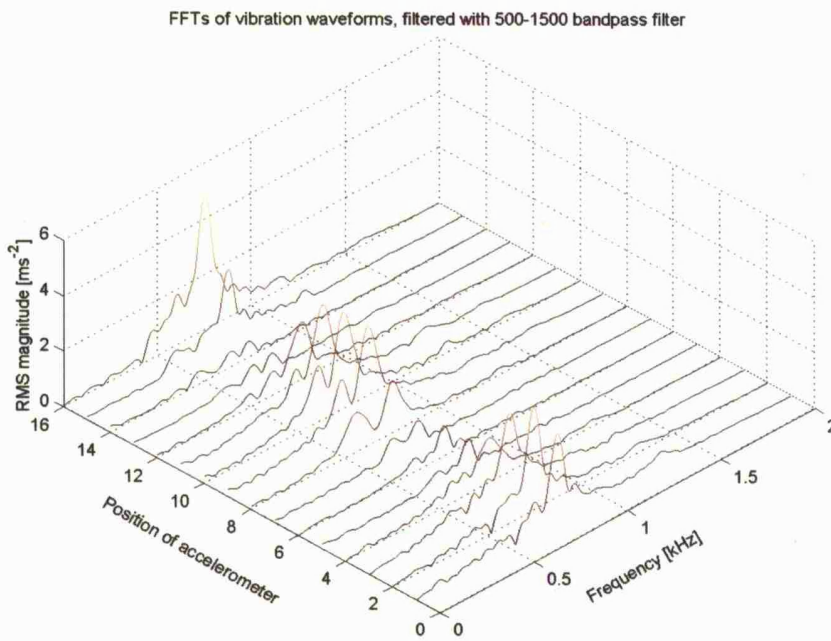
FFT of unfiltered vibration waveforms in Figure 3.14(c). Magnitudes are in linear RMS.

Figure 3.15: Static vibration test results

From Figure 3.14(c), it shows the vibration waveforms from all 16 measurement points on the stator lamination during the static vibration test. *Note that the waveform amplitudes and FFT amplitudes are not to scale, and hence not comparable.* In Figure 3.14(c), from the bottom waveform to the top are data at the first measurement point to the 16th measurement point, going clockwise around the stator lamination in Figure 3.13. It can be observed that, in the frequency range from 0 to 10kHz, significant components are observed before 2000Hz and between 2000Hz and 4000Hz, as shown in Figure 3.15. Hence, in order to identify the particular component frequency value and its vibration mode shape, these data were fed through a digital FIR filter, post-processed in MATLAB.



(a) Waveforms filtered by bandpass FIR filter of the 130th order, Hanning windowed. Waveforms from bottom to top are vibrations on positions 1 to 16 respectively. Amplitudes are not to scale.



(b) FFT of waveforms in Figure 3.16(a). Magnitudes are in linear RMS.

Figure 3.16: Vibration data after bandpass filtering between 500Hz and 1500Hz

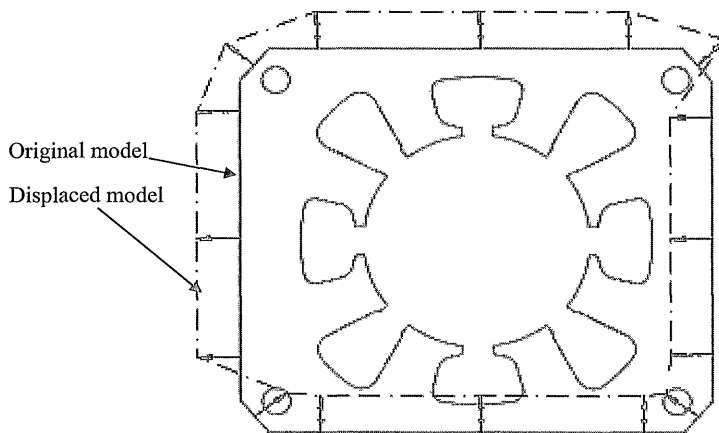
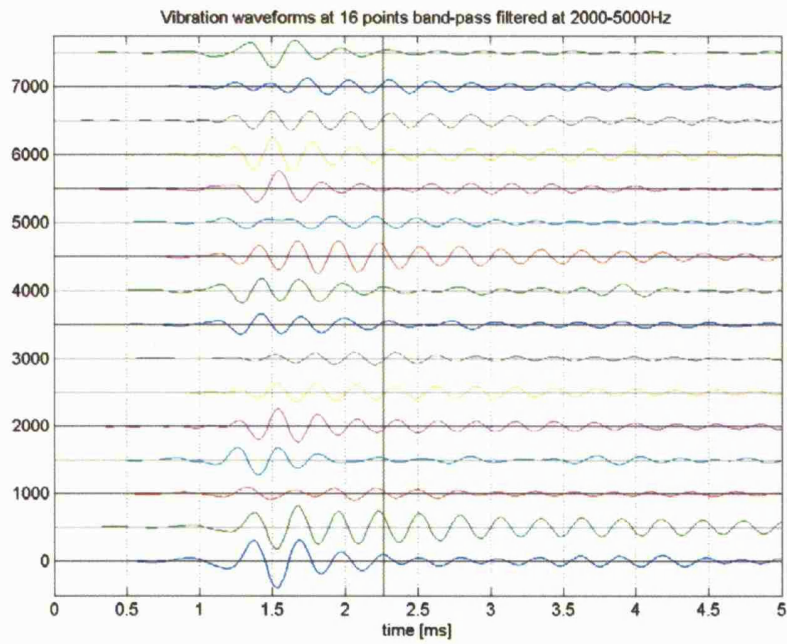


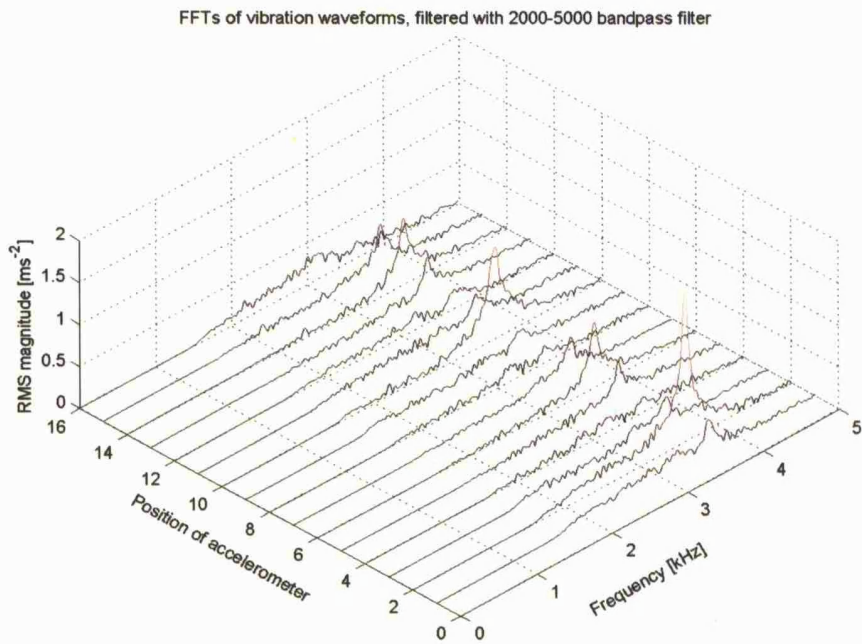
Figure 3.17: Vibration mode $m=1$ at around 700Hz.

Arrows indicate vibration direction at an instant in time, magnitude of arrow not to scale. Dash lines indicate vibration mode shape.

From Figure 3.16(a), assuming that a positive vibration is an outward acceleration and a negative vibration is an inward acceleration, the vibration at any one point in time from all the 16 points can be plotted onto Figure 3.13, which then produces a displacement plot of Figure 3.17. Figure 3.16(a) and Figure 3.17 suggest that the motor lamination has an average mechanical resonant frequency of 700Hz with a vibration mode of mode 1. This mode could have arisen due to the vibration of the assembly of the vacuum cleaner, because the whole supporting frame is prone to vibration as there is no support on the whole machine system which is placed on the floor or table.



(a) Waveforms filtered by bandpass FIR filter of the 130th order, Hanning windowed. Waveforms from bottom to top are vibrations on positions 1 to 16 respectively. Amplitudes are not to scale.



(b) FFT of waveforms in Figure 3.18(a). Magnitudes in linear RMS.

Figure 3.18: Vibration data after bandpass filtering between 2000Hz and 5000Hz

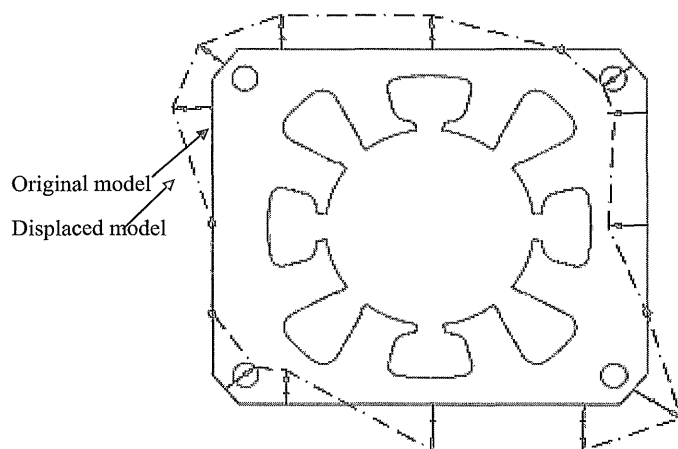


Figure 3.19: Vibration mode $m=2$ at around 3500Hz.

Arrows indicate vibration direction at an instant in time, magnitude of arrow not to scale. Dash lines indicate vibration mode shape.

From Figure 3.18(a), again assuming that a positive vibration is an outward acceleration and a negative vibration is an inward acceleration, the point of displacement at each 16 point can be drawn onto Figure 3.13 and produce a displacement plot as shown in Figure 3.19. Figure 3.18(a) and Figure 3.19 both suggest that the motor lamination has another average mechanical resonant frequency of 3500Hz, which has a vibration mode of mode 2.

Filtering to analyse the frequency components higher than 5000Hz were not done because, as shown in Figure 3.15(b), the power of these frequency components were very small compared to the components of 700Hz and 3500Hz.

3.3.2 Dynamic tests

The dynamic vibration test was performed by running the motor at various motor speeds, and recording vibration and acoustic noise measurements. The power electronic drive is shown in Figure 1.3.

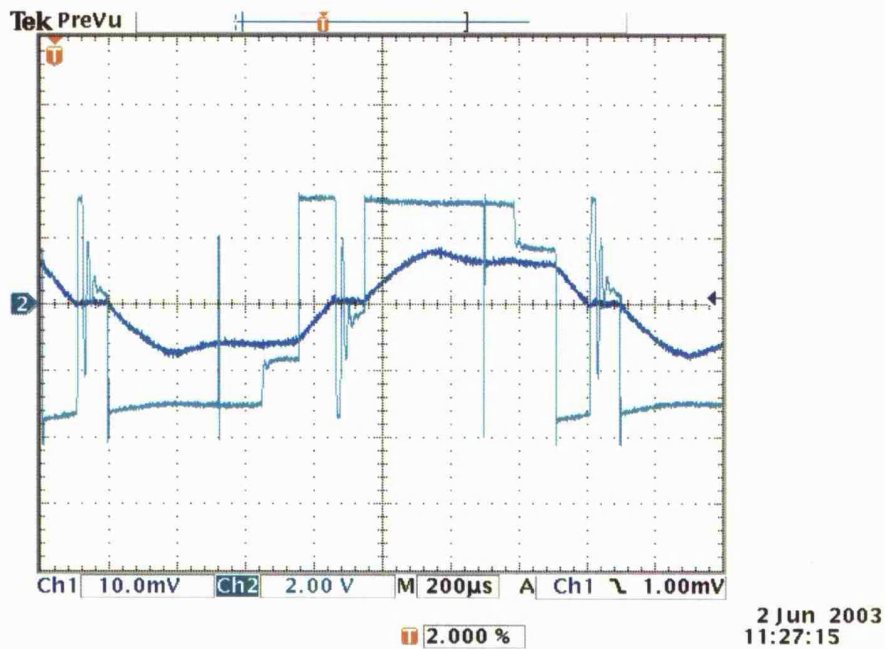


Figure 3.20: Current and voltage waveforms are obtained at 10000rpm.

Blue trace is current flowing through both windings (0.5A/div); Purple trace is voltage across ONE armature winding.

Figure 3.20 shows the armature voltage of 1 armature winding, and the current flowing through both armature windings while running at average speed of 10000rpm. The voltage waveform where the current has negative slope, i.e. where current decreases to zero, occurs when the magnetizing current of the one armature winding free-wheels in the free-wheeling diodes across the switches, and flows back to the supply via the other armature winding. When this current reaches zero, the free-wheel diode is reverse-biased, hence the reverse recovery oscillation shown in Figure 3.20. When the next switch is closed later, the voltage applied across the armature windings builds up a current drawn from the supply again.

A method to visualize the vibration or noise components in relation with the motor speed was to plot the vibration or noise amplitude, its frequency and motor speed in one single surface plot. This enables the possibility to observe what particular vibration frequency is excited at certain motor speeds, and if the vibration or noise amplitude excited is high at that motor speed, then either

active vibration or noise cancellation should be employed at that speed, or the motor should not be operated at that motor speed at all.

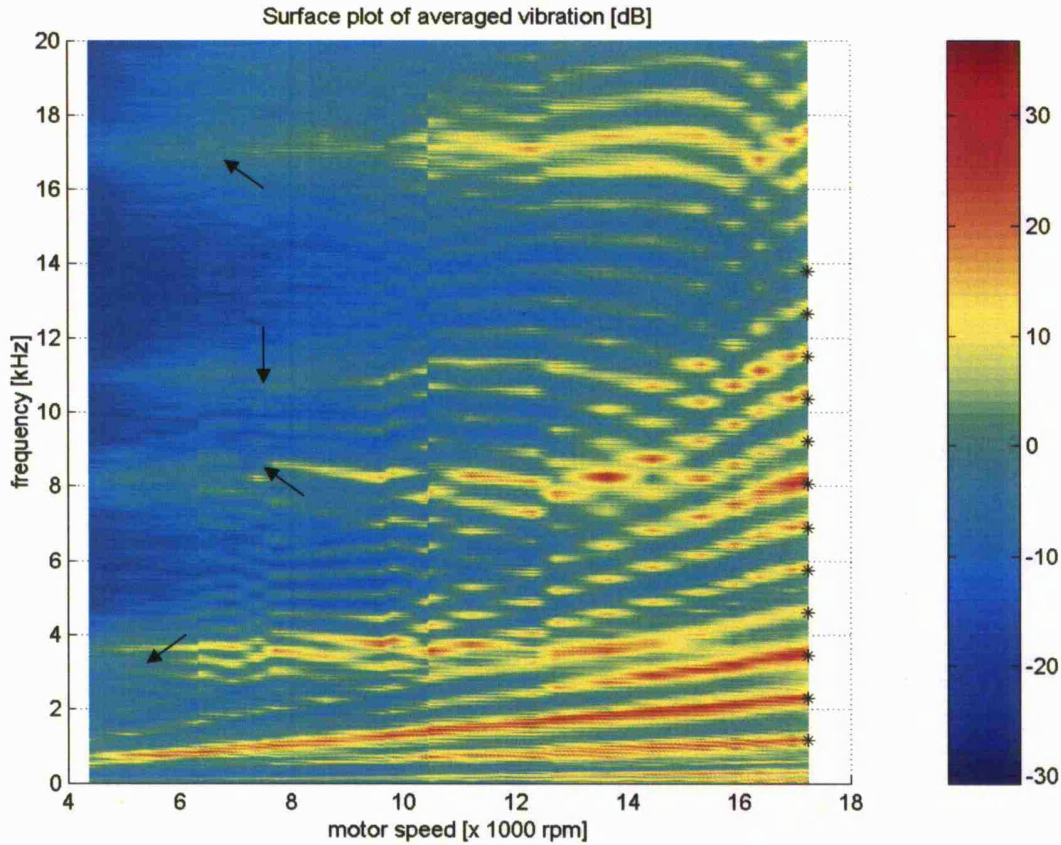


Figure 3.21: Plot of vibration frequency against motor speed.

Colorbar indicates the RMS magnitude in [dB]. '*' indicates the harmonics of the motor commutation frequency at 17250rpm

Figure 3.21 shows the averaged vibration frequency response taken from the 16 measurement points at different motor speeds. It could be observed that, significant diagonal region lines appear in the plot. These are where the harmonics of the motor commutation frequency lies, as indicated by '*' for a motor speed at 17250rpm.

There are also indications of regions where the vibration frequencies are independent of motor speed, and excited at various motor speeds and vary in amplitude. These regions are pointed by arrows in Figure 3.21 which correspond to about 3.5kHz, 8kHz, 11kHz and 17kHz, termed here as speed-independent-frequencies (SIF). The 3.5kHz frequency region has a value close to the mechanical resonant frequency for vibration mode $m=2$, as obtained from the static vibration test in Figure 3.18 and Figure 3.19, suggesting that these SIF regions are indicating the values of some of the mechanical resonant frequencies that the stator lamination possesses. At some motor speeds, the

vibration of 3.5kHz is weak in amplitude, while at some motor speeds, the vibration of 3.5kHz is strong in amplitude, as indicated by the surface plot colours. Another interesting feature from Figure 3.21 is that, it shows what motor speeds are likely to have its harmonics coincide with the SIFs. It is desirable that the motor does not operate at the motor speed which has its motor speed harmonics coinciding with the SIF regions and inducing the highest-amplitude vibration. For example, running at 17250rpm, the third motor commutation harmonic, as shown in Figure 3.21, coincides with the first SIF of 3.5kHz, and having a high amplitude. Furthermore, it can be seen that, the higher the motor speed gets, the higher the magnitude of the vibration becomes. If more samples were taken, the area of the SIFs could be shown more distinctly in order to pin-point a more accurate motor speed to avoid its harmonics coinciding with the SIFs.

3.3.3 Acoustic noise analysis on polygon-shaped flux switching motor

Figure 3.22 shows a surface plot of acoustic noise FFT against motor speed, with indications of mostly speed dependent noise frequencies. Unlike the vibration surface plot in Figure 3.21, there's no significant region where any acoustic noise frequency is independent of motor speed. Furthermore, as motor speed increases, the magnitude of the frequency components increases as well. A high whistling noise was subjectively heard while running the motor, and the noise amplitude and frequency varied while motor speed was changing.

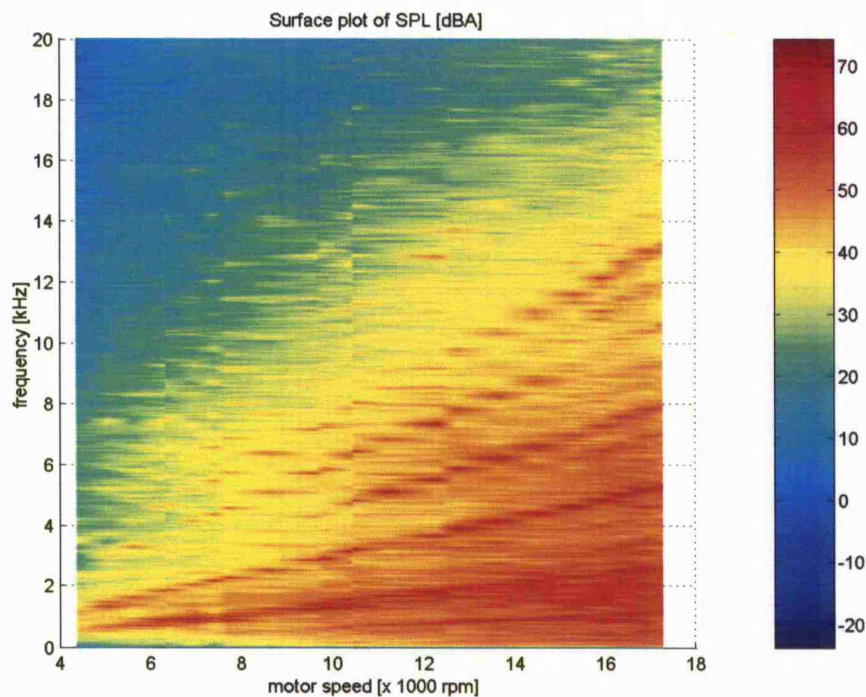


Figure 3.22: Acoustic noise surface plot.
Colorbar indicates magnitude in [dBA]

3.3.4 The elimination implementation

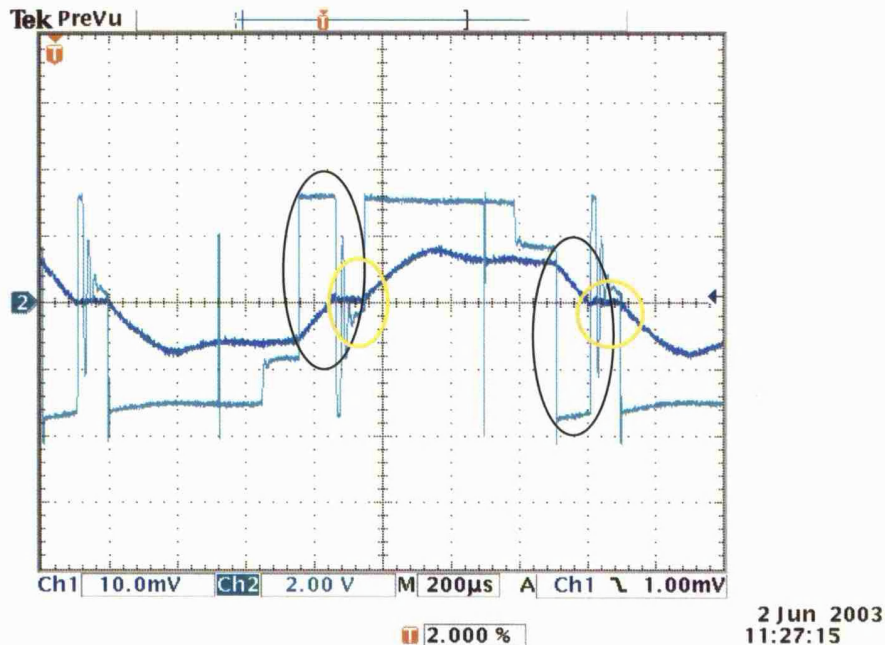


Figure 3.23: Current and voltage waveforms are obtained at 10000rpm

Blue trace is current flowing through both windings (0.5A/div); Purple trace is voltage across ONE armature winding.

The voltage pulses, as an example shown in Figure 3.23, build up pulses of flux density on the winding, and create pulses of magnetic radial force, which was believed to create vibration on the stator lamination and propagate acoustic noise in this investigation. On the voltage waveform, it can be observed that, the short pulses encircled in black in Figure 3.23 have a frequency of around 3kHz at 10000rpm. This pulse frequency varies with motor speed as well. It was then believed that, since the short voltage pulses are speed dependent, it could be this short voltage pulse that creates the consequent speed-dependent acoustic noise as shown in Figure 3.22.

It is desirable that the short pulse shown in Figure 3.23, be eliminated or shortened to increase its frequency above audible range, as it is believed to be this short, high-frequency pulses that are contributing to the vibration and acoustic noise at all speeds. To eliminate the short voltage pulses, means forcing the current to go through zero instead of staying at zero for a finite time, as shown encircled in yellow in Figure 3.23.

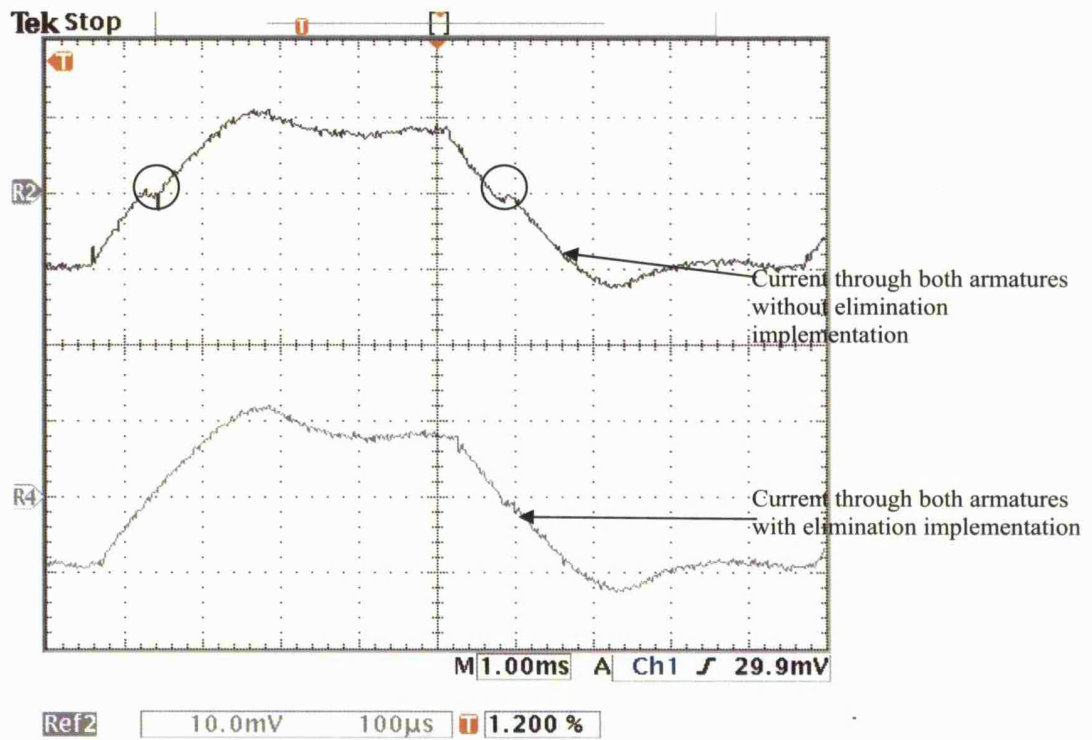


Figure 3.24: Current and voltage waveforms at 16350rpm.
Current scale: (0.5A/div)

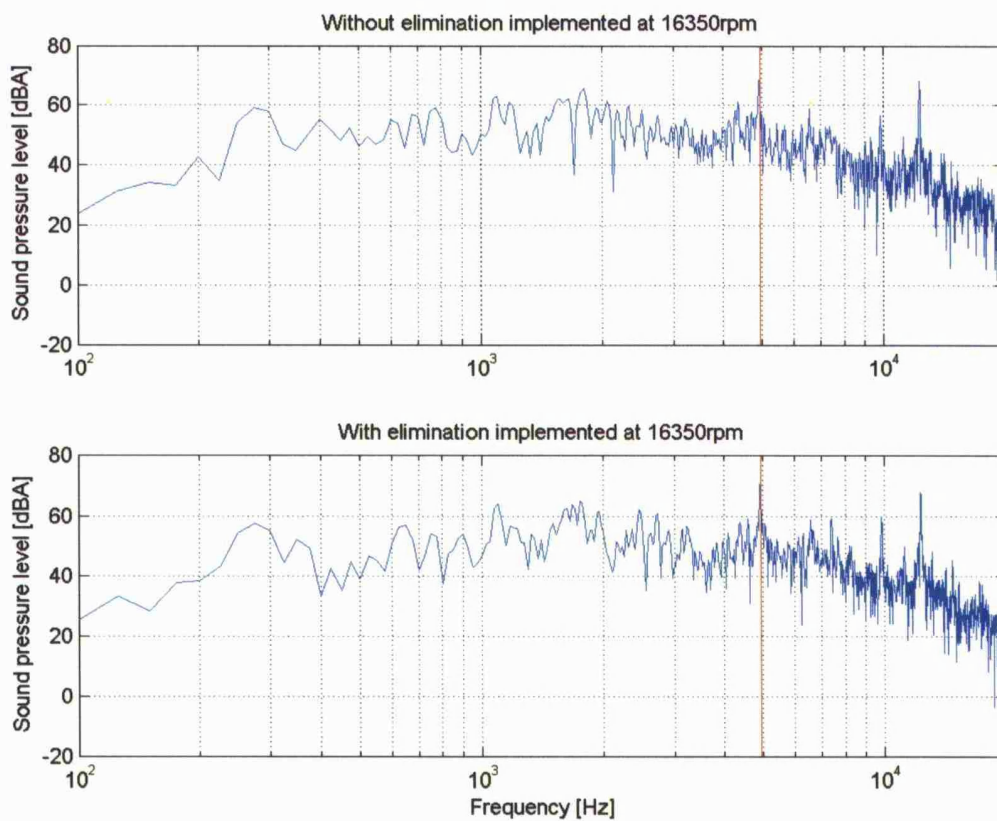


Figure 3.25: Acoustic noise FFTs at 16350rpm

Figure 3.24 shows current waveforms with the motor running at 16350rpm, with and without the elimination implemented. Note that the current section stays at zero, encircled, on the upper waveform before elimination. The bottom waveform shows where the current is passing through zero while the elimination was implemented.

However, the significant whistling noise was not reduced, which could still be heard subjectively. As Figure 3.25 shows, there's no significant elimination in the acoustic noise frequency domain. A significant 5kHz noise component still remained in the frequency domain shown at the red cursor.

This probably suggests that the maximum noise detected might be of aerodynamic origin such as siren tones, blade passing frequencies etc. Further investigation was done on finding out what possible siren tones might have been produced. There are 9 blades on the impeller.

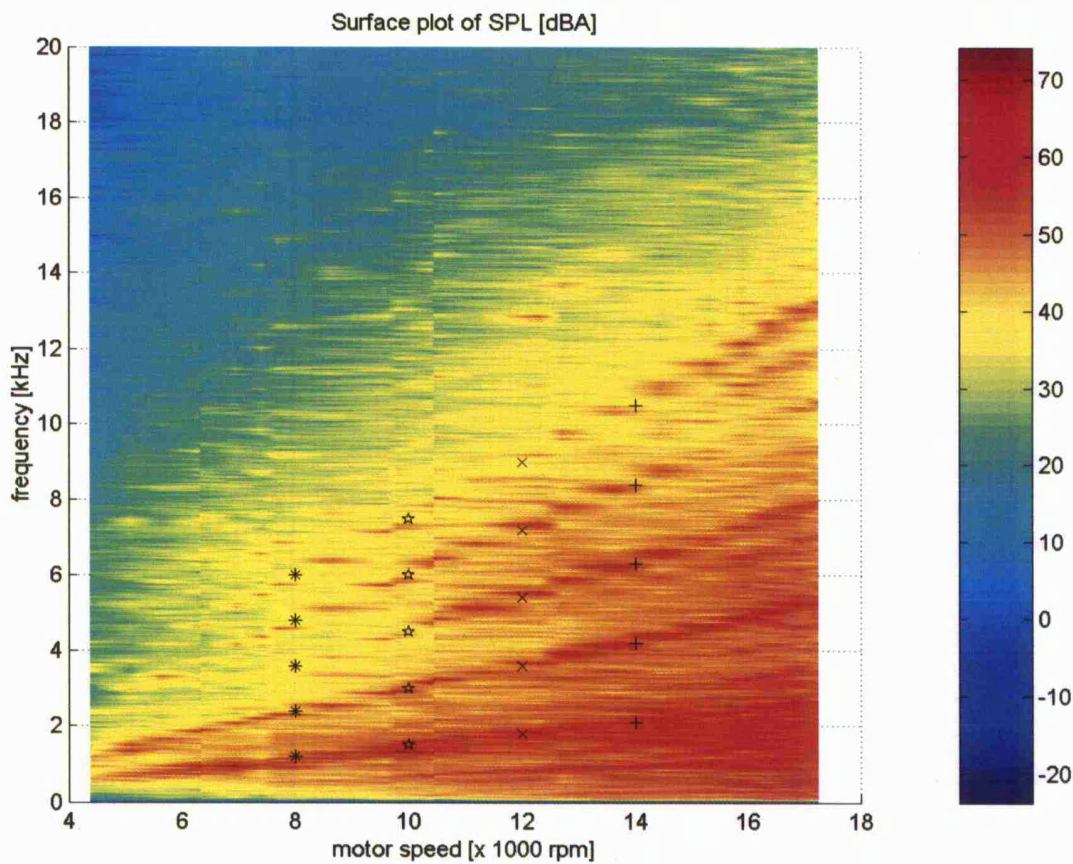


Figure 3.26: Surface plot showing acoustic noise frequency against motor speed.

Colorbar indicates the magnitude in [dBA]. '*' siren tone FFT peaks at 8000rpm; '☆' siren tone FFT peaks at 10000rpm; 'x' siren tone FFT peaks at 12000rpm; '+' siren tone FFT peaks at 14000rpm;

In Figure 3.26, siren tone frequencies computed by equation (1.2) were plotted onto the acoustic noise surface plot. As shown in Figure 3.26, the siren frequencies coincide with the

diagonal regions (that indicate the speed harmonics) on the acoustic noise surface plot at motor speed of 8000rpm, 10000rpm, 12000rpm and 14000rpm. This suggests that the dominant acoustic noise source is of aerodynamic characteristics, which are speed-dependent.

3.4 Summary

	Measured average mechanical resonant frequency of vibration mode 2
Round-shaped FSM	2496Hz (concluded in section 3.2.2)
Polygon-shaped FSM	3500Hz (concluded in Figure 3.19)

Table 3.1: Measured mechanical resonant frequency

Table 3.1 summarises the measured mechanical resonant frequency of vibration mode 2 of the round-shaped and polygon-shaped FSM. Only the vibration mode 2 results are summarized because they appear in both the static vibration test and dynamic test, which weighs more attention to the lower modes. Methods applied in the experiments, were able to extract the mechanical resonant frequency and its corresponding vibration mode shape by investigating the time-domain of the mechanical response [7].

From the round-shaped FSM, its noise source was traced to the motor's housing, which could be induced by the vibration of the motor lamination. The high-pitch whistling noise was the dominant noise component produced by the polygon-shaped FSM, and it is believed to be of aerodynamic origin, since the voltage pulse elimination did not significantly reduced the whistling noise subjectively. Furthermore, using the siren tone equation of equation (1.2), most components of the siren tone coincides with the significant components of the acoustic noise detected, as shown in Figure 3.26. Measurement results could probably be improved when more time could be spent in obtaining more results and taking the average of them. Using even smaller accelerometers could give the opportunity to measure the vibration on more points around the surface area of the polygon-shaped FSM stator lamination, and consequently giving a better resolution of the vibration surface plot in Figure 3.21. With better resolution, the speed-independent-frequencies can be distinctly shown along the various motor speeds, and one can determine which motor speed to avoid operating on that could result in producing mechanical resonance.

Chapter 4

PREDICTING THE MECHANICAL RESONANT FREQUENCY OF THE FLUX SWITCHING MOTOR

4.1 Introduction

Prediction of the mechanical resonant frequency of an electrical machine during the design stage is important, which can determine whether the electrical machine is mechanically reliable as well as being electromagnetically efficient. In this chapter, a mechanical finite element package and simple algebraic frequency equations are used in order to predict the mechanical resonant frequency of the round-shaped and polygon-shaped Flux Switching Motor (FSM) mentioned in Chapter 3. Mechanical finite element packages are commercially available to predict mechanical resonant frequencies of electrical machines, but these finite element packages could impose extra cost into electrical machine design projects using finite element packages that can only perform electromagnetic analysis. Hence, it would be a good idea to implement some simple algebraic frequency equations that could be implemented into electromagnetic finite element packages in order to predict the mechanical resonant frequency of the electrical machine designed, which will be useful for electrical machine design engineers, and without incurring extra cost on purchasing mechanical finite element packages or optional software modules.

The investigation first uses the mechanical finite element packages to predict the mechanical resonant frequencies of the round-shaped and polygon-shaped FSMs, and compare results with experimental results presented in Table 3.1. Then, three algebraic frequency equations derived in literatures, will be introduced and will be implemented into the electromagnetic finite element package. A choice will be made on which algebraic equation is most suitable to be implemented and can give a good prediction of the mechanical resonant frequency of the electrical machines. Conclusions will point out that, the mechanical finite element is yet the best option into predicting the mechanical resonant frequency of the stator of the FSM, regardless of its stator shape. Moreover, the algebraic frequency equation derived for thick rings was found to be most suitable to predict the round-shaped FSM's mechanical resonant frequency, but unable to give an approximate mechanical resonant frequency for the polygon-shaped FSM.

4.2 Finite element analysis of mechanical resonant frequency

The mechanical finite element modelling tool used for the work presented here is called FEMLAB 3.0. It allows 2D and 3D mechanical modelling and analysis. FEMLAB was mainly used to extract any possible mechanical resonant frequencies (termed as the ‘eigenfrequencies’ in the finite element package) and vibration mode shapes of a given stator model of an electrical machine.

All the stator models are considered to be a lump, solid model. One of the most important aspects to consider is the boundary conditions applied to the model. It is ultimately desired that the boundary conditions reflect the boundary conditions applied in the real world, otherwise inconsistent results will be presented. Units used are another crucial aspect to be considered carefully, which should be consistent in dimensions as well as in material constants. All dimensions of the finite element models are shown in metres.

The mechanical resonant frequency extraction was performed on the round-shaped FSM stator lamination where its 3D model in FEMLAB is shown in Figure 4.1. The photo of the machine used in this investigation is shown in Figure 4.2(b).

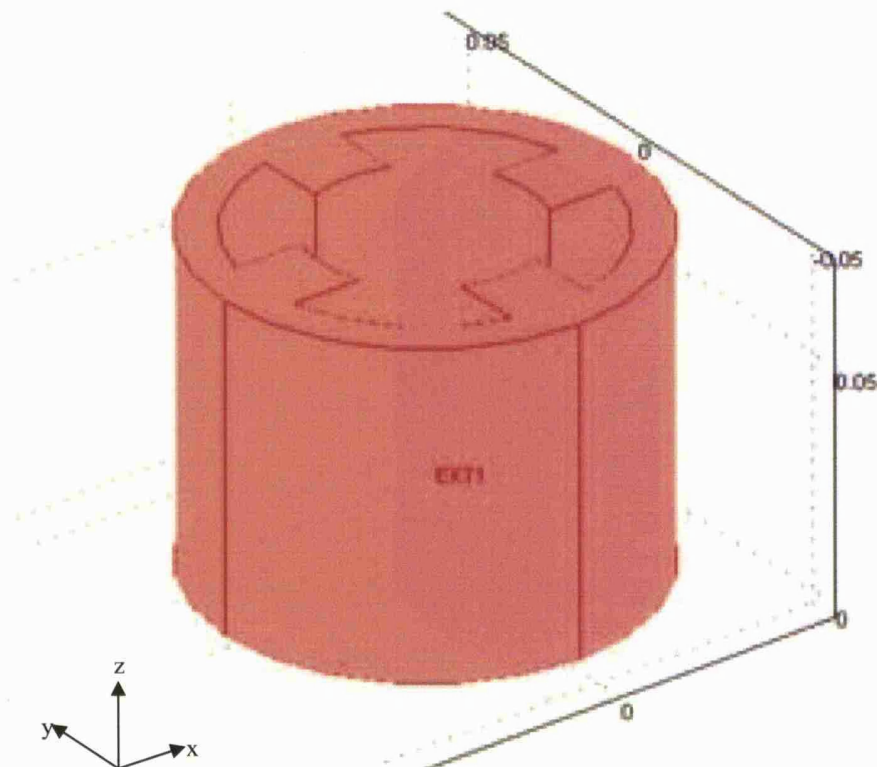
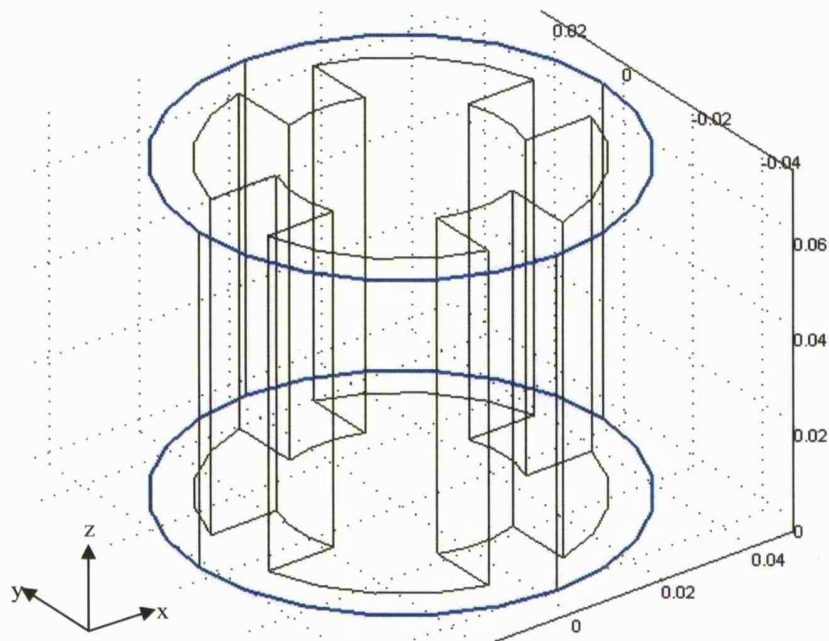


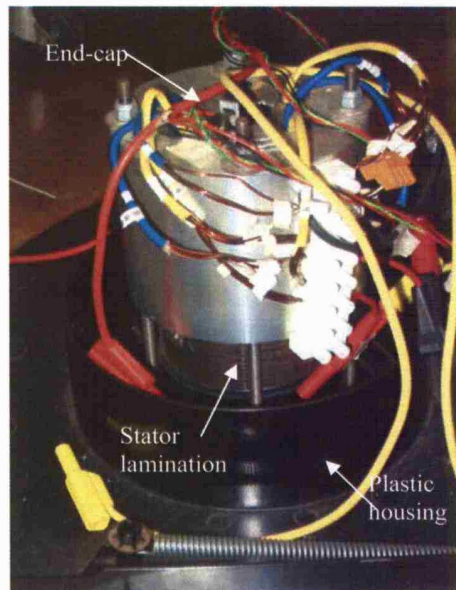
Figure 4.1: Round-shaped FSM model in FEMLAB.

Figure 4.2(a) shows the edges where simple supports were applied, constraint in the z-direction. This is because in the real motor, shown in Figure 4.2(b), the top end-cap clamps the stator laminations in the axial direction to the plastic lawnmower housing, but introducing no

support in the x- and y- directions. The material constants used are: $E = 201\text{GPa}$, $\rho = 7930\text{kg/m}^3$ and $\nu = 0.28$.



(a) Simply supported edges constraint in the z-direction



(b) Photo of motor

Figure 4.2: Constraints applied on round-shaped FSM model

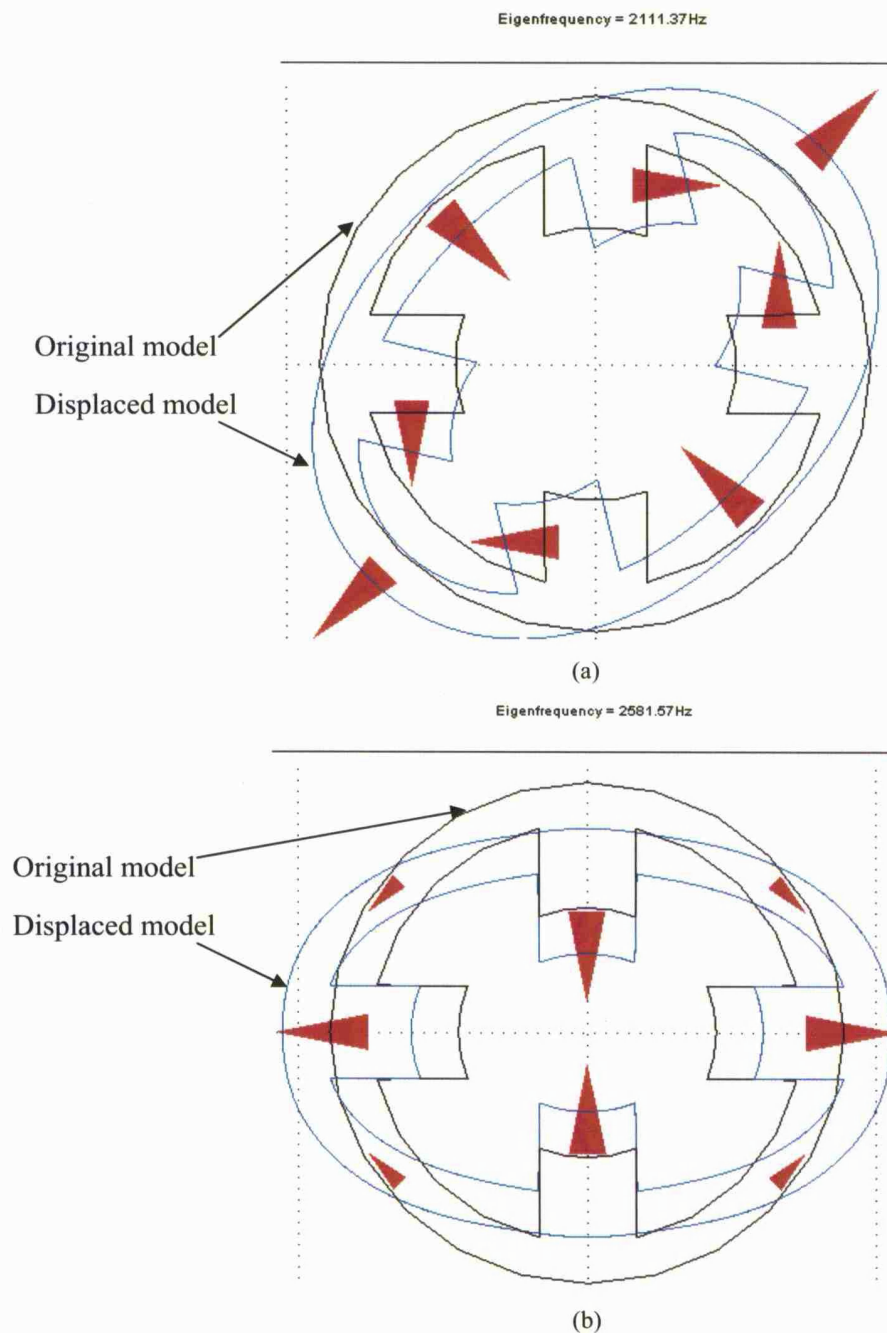


Figure 4.3: Vibration mode 2 of round-shaped flux switching motor

Figure 4.3 shows the result of the first two lowest resonant frequencies extracted, having a vibration mode shape of mode 2 ($m=2$) [23] with a corresponding resonant frequency of 2111.37Hz and 2581.57Hz respectively. Cone-shaped arrows indicate direction of displacements. Displaced model is magnified. This analysis from the finite element analysis does not show exactly how much displacement has occurred in this ovalisation. Figure 4.3(a) could suggest that this could be one of the vibration mode which could not be measured due to the obstruction of the pillars on the actual

motor, as described in section 3.2.1. Figure 4.3(b) confirms the measured vibration mode 2 of 2496Hz in section 3.2.

The same mechanical resonant frequency extraction analysis was then performed on the polygon-shaped FSM stator model. The model was simply supported on 4 edges, and constraint in the z-direction as shown in Figure 4.4(b), because in reality the stator is clamped axially by an end-cap which is fastened by 4 nuts onto the impeller housing as shown in Figure 4.5. The impeller housing sits onto the vacuum cleaner housing which has wheels and does not provide any stiff constraints in the x- and y- directions. The material constants used are: $E = 201\text{GPa}$, $\rho = 7930\text{kg/m}^3$ and $\nu = 0.28$.

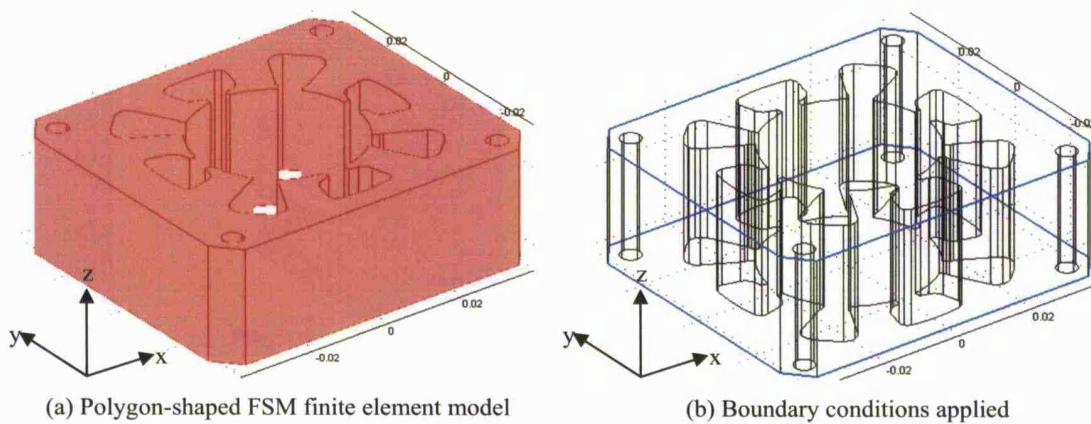


Figure 4.4: Polygon-shaped FSM model in FEMLAB



Figure 4.5: Photo of actual polygon-shaped flux switching motor with supports

Eigenfrequency = 3442.31Hz

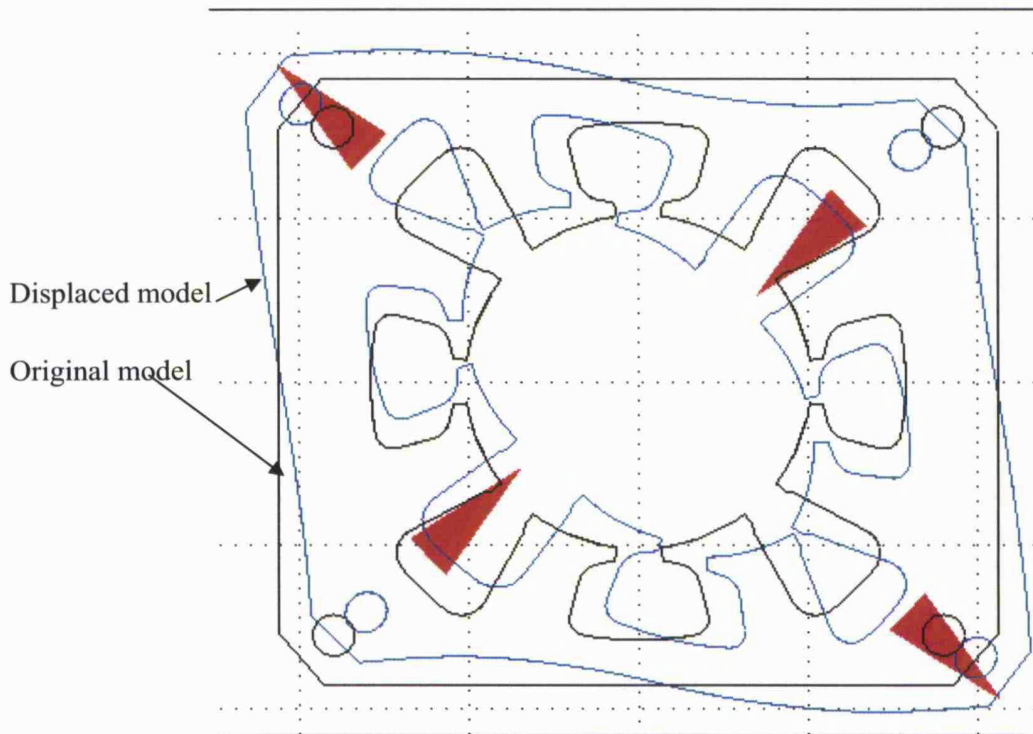


Figure 4.6: Vibration at 3442.31Hz of mode 2

It could be seen in Figure 4.6, the predicted mechanical resonant frequency (or called eigenfrequency by the finite element package) at mode 2 from the finite element package is 3442.31Hz. The finite element analysis does not show exactly how much displacement has occurred in this displacement.

	Measured mechanical resonant frequency in vibration mode 2	Finite element predicted mechanical resonant frequency in vibration mode 2	Percentage error
Round-shaped FSM	2496Hz	2581.57Hz	3.43%
Polygon-shaped FSM	3500Hz	3442.31Hz	1.65%

Table 4.1: Comparison of measured and finite element predicted mechanical resonant frequency

From Table 4.1, it shows that the finite element prediction of the mechanical resonant frequency of vibration mode 2 ($m=2$) for both the round-shaped and polygon-shaped FSM were

close to the measured mechanical resonant frequency results from Table 3.1. However, the mechanical finite element models were modeled as lump models, not as laminated models. This could be why the presence of inconsistencies in the results. Some work has been known that the effective Young's Modulus value for laminated steel should be less than the commonly used value [17] applied to lump models. In addition to that, the shear moduli effect between laminations could be modeled by employing lower in-plane shear modulus, G_{xy} , of the lamination [18]. Furthermore, the windings on the stator were not modeled, which could introduce damping onto the whole system, or even treated as additional mass. In [18], the effects of winding were modeled taking into account of the end-windings, and concluded that the mass of the winding compensates the influence of the stiffness of the winding on the mechanical resonant frequencies, hence the overall effect of windings on the mechanical resonant frequencies is relatively insignificant. Employing these extra points into the mechanical resonant frequency analysis of FEMLAB might substantially bring the predicted value closer to the measured value. It also verifies the believe that finite element natural frequency prediction is very accurate, as pointed out in [23], who has also made numerous research using finite element analysis.

4.3 Mechanical resonant frequency prediction of electrical machines using algebraic analysis

Previous studies have been concerned on predicting accurately the mechanical resonant frequency of round-shaped stator cores [19,20,21] and [22]. More recent studies emphasized that different approaches is required on machines with the stator yoke's thickness-to-mean radius ratio exceeding 0.2 [19]. Girgis and Verma in [19] and Ellison and Yang [22] used energy approaches in order to predict the natural frequencies of the stator core, involving huge matrices, depending on accuracy.

Authors from [19] and [22] computes the kinetic energy and potential (or strain) energy of the stator core using the expressions for a cylindrical shell of length L and inner radius r_1 , and outer radius r_0 according to the three-dimensional theory of elasticity respectively.

$$K.E. = \frac{\rho}{2} \int_{z=0}^{z=L} \int_{\phi=0}^{\phi=2\pi} \int_{r=r_1}^{r=r_0} \left[\left(\frac{\partial u}{\partial t} \right)^2 + \left(\frac{\partial v}{\partial t} \right)^2 + \left(\frac{\partial w}{\partial t} \right)^2 \right] r \cdot dr \cdot d\phi \cdot dz \text{ ----- (4.1)}$$

$$P.E. = \frac{1}{2} \int_{z=0}^{z=L} \int_{\phi=0}^{\phi=2\pi} \int_{r=r_1}^{r=r_0} [\sigma_r \epsilon_r + \sigma_\phi \epsilon_\phi + \sigma_z \epsilon_z + \tau_{r\phi} \gamma_{r\phi} + \tau_{rz} \gamma_{rz} + \tau_{\phi z} \gamma_{\phi z}] r \cdot dr \cdot d\phi \cdot dz \text{ ---- (4.2)}$$

The energy components of the teeth, windings and cooling ribs were treated as cantilevers attached to the body of the stator. The displacements are approximated to finite double power series:

$$u = \sum_{i=1}^P \sum_{j=1}^Q (a_{ij} \cos m\phi) z^{i-1} r^j \quad (4.3)$$

$$v = \sum_{i=1}^P \sum_{j=1}^Q (b_{ij} \sin m\phi) z^{i-1} r^j \quad (4.4)$$

$$w = \sum_{i=1}^P \sum_{j=1}^Q (c_{ij} \cos m\phi) z^{i-1} r^j \quad (4.5)$$

where a_{ij} , b_{ij} and c_{ij} are unknown coefficients which serve as the generalized coordinates of the system. P and Q are two integers which determine the size of the mathematical model representing the vibrating system, and determines the accuracy of the calculations of the mechanical resonant frequencies.

From (4.3), (4.4) and (4.5), the total kinetic and strain energies of the stator can be expressed in terms of generalized coordinates, and then they were substituted into the well-known Lagrange's equation for a conservative system shown in equation (4.6).

$$\frac{d}{dt} \left(\frac{\partial T}{\partial \dot{x}} \right) + \frac{\partial U}{\partial x} = 0 \quad (4.6)$$

Substitution into the Lagrange's equation leads to a set of homogeneous equations, where its coefficients forms a matrix of the form below, where K and M are the stiffness and mass coefficient matrices respectively, \ddot{X} and X are the acceleration and displacement vectors respectively.

$$[K][\ddot{X}] - \omega^2[M][X] = 0 \quad (4.7)$$

Solving the matrix equation yields the mechanical resonant frequencies and vibration modes, which were also termed the eigenvalues and eigenmodes respectively. Details of the analysis can be found in [19].

Instead of going through the whole process of computing the mechanical resonant frequency of the stator core as done in [19] - [21], derived simple formulae are used here to predict the mechanical resonant frequencies of the round-shaped stator core. Simple formulae derived by Jordan, Frohne and Uner are compiled by Yang in [23] that approximate the mechanical resonant frequency of a single-ring type stator. Effects of shear, rotary inertia, teeth and winding were also taken into account.

The mechanical resonant frequency for a circumferential vibration mode of $m = 0$ mentioned in [23] is

$$f_{[m=0]} = \frac{1}{2\pi R_m} \left(\frac{E}{\rho \Delta} \right)^{\frac{1}{2}} \text{ [Hz]} \text{----- (4.8)}$$

Δ : mass addition factor for displacement, where $\Delta = 1 + \frac{G_z + G_w + G_B}{G_j}$

For a circumferential vibration mode of $m = 1$, the approximate mechanical resonant frequency mentioned in [23] is

$$f_{[m=1]} = f_{[m=0]} \left(\frac{2}{1 + a^2 \frac{\Delta_m}{\Delta}} \right)^{\frac{1}{2}} \text{ [Hz]}, \text{----- (4.9)}$$

where $a = \frac{h}{2\sqrt{3}R_m}$; $\Delta_m = 1 + \frac{Z_{st}B_z}{2\pi I_m R_m}$ called the mass addition factor for rotation;

$$B_z = A_z^* I_z^3 \left\{ \frac{1}{3} + \frac{h}{2l_z} + \left(\frac{h}{2l_z} \right)^2 \right\}; A_z^* = A_z \left(\frac{G_z + G_w + G_B}{G_z} \right)$$

The approximate mechanical resonant frequency of any mode equal or above 2 is given by

$$f_{[m \geq 2]} = \frac{f_{[m=0]} a m (m^2 - 1) \phi_m}{\sqrt{m^2 + 1}} \text{ [Hz]}, \text{----- (4.10)}$$

$$\text{where } \phi_m = \left\{ 1 + \frac{a^2 (m^2 - 1) \left[m^2 \left(4 + \frac{\Delta_m}{\Delta} \right) + 3 \right]}{m^2 + 1} \right\}^{\frac{1}{2}} \text{ as mentioned in [23].}$$

Since the most common vibration mode is during ovalisation of the stator, i.e. when $m = 2$,

$$\therefore f_{[m=2]} = \frac{2.685 a f_{[m=0]}}{\left[1 + 0.61 a^2 \left(19 + 4 \frac{\Delta_m}{\Delta} \right) \right]^{\frac{1}{2}}}, \text{----- (4.11)}$$

Colby, Mottier and Miller in [24] have derived simple frequency equations for the fundamental mode, $m=2$, of a uniform cylindrical shell for a four-phase switched reluctance motor, where its deflection is assumed to be due solely to bending neglecting the effect of direct axial tension or compression and of shear and assumed that the stator yoke's radial thickness is very small in comparison with its ring radii that deflection theory of straight beams can be applied as stated by Roark and Young in [25]. The strain energy considered a plain ring deflected due to a

vertical load, while its kinetic energy assumes that the ring is deformed into an ellipse initially. The frequency equation derived for a vibration mode of 2, invoking energy conservation, is given as:

$$\omega^2 = \frac{2(1.0445)^2 Et^2}{(1.625)\pi\rho R_m^4} \text{-----} \quad (4.12)$$

In [26], Kirkhope derived a simple frequency equation for the in-plane vibration of thick circular rings, accounting for effects of transverse shear and rotary inertia, but no consideration of teeth and windings. Kirkhope in this paper provides a correction factor to the original frequency equation derived by Hoffe in [27] that neglected extensional shear and rotatory energy contributions. The equation employing Kirkhope's correction factor is:

$$\omega^2 = \frac{E I_m}{\rho A R_m^4} \left(\frac{k^2(k^2 - 1)^2}{k^2 + 1} \right) \left(\frac{1}{1 + k^2 \alpha} \right) \text{-----} \quad (4.13)$$

$$\alpha = \frac{I_m E}{G K_{rec} A_{esa, yoke} R_m^2}, K_{rec} = \frac{10(1 + \nu)}{12 + 11\nu} \text{ for rectangular cross sections [28]}$$

All these equations mentioned above were derived by assuming a round shape stator core. Studies on how the different shapes of the stator influences the mechanical resonant frequency of the stator core and the vibration mode shapes it will produce has also being done [29].

4.4 Implementation of simple algebraic frequency equation

In this section, equations (4.11), (4.12) and (4.13) were implemented to predict the mechanical resonant frequency of the round-shaped FSM stator lamination as shown in Figure 4.7. It has its dimensions tabulated in Table 4.2.

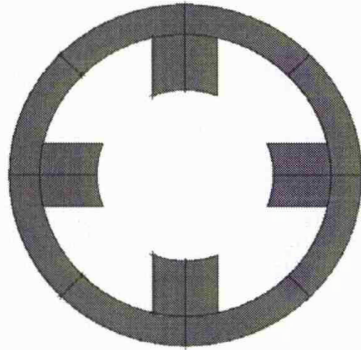


Figure 4.7: Stator ring of flux switching motor

Stator geometric dimensions:	
Outer diameter	89mm
Inner diameter	44.5mm
Yoke thickness	7.25mm
Tooth length	14.5mm
Tooth width	16.5mm
Stator yoke pole arc angle	43.5°
Stator stack length	70mm
Material constants of stator:	
Young's Modulus	201GPa
Density	7930kgm ⁻³
Poisson's ratio	0.28
Shear Modulus	84GPa

Table 4.2: Geometric dimensions and material constants

The implementation of the frequency equations (4.11), (4.12) and (4.13) were done in the electromagnetic finite element package, OPERA. OPERA uses the given geometrical dimensions to compute the necessary geometrical parameters, and then substitutes these parameters into the frequency equations in order to compute a theoretical resonant frequency at a specified vibration mode shape, m . During this implementation, all the frequencies extracted is for the vibration mode shape of $m=2$, because that is the fundamental mode shape of the vibration, which usually has the largest vibration amplitude and possessing the lowest mechanical resonant frequency of an object.

Table 4.3 below, tabulates the results of the resonant frequencies calculated from OPERA by implementing the 3 simple algebraic frequency equations (4.11), (4.12) and (4.13).

Equation number	Frequency calculated for vibration mode 2, f [Hz]
(4.11)	2136.52
(4.12)	2273.14
(4.13)	2654.32

Table 4.3: Calculated mechanical resonant frequencies for mode 2

Measured value [Hz]	From equation (4.11) [Hz]	From equation (4.12) [Hz]	From equation (4.13) [Hz]
2496	2136.52	2273.14	2654.32
Percentage errors	14.40%	8.93%	6.34%

Table 4.4: Comparison of measured and calculated mechanical resonant frequencies for vibration mode 2

Table 4.4 tabulates the percentage error between the mode-2 mechanical resonant frequencies computed by equations (4.11), (4.12) and (4.13) and the measured result of 2496Hz. Equations (4.12) and (4.13) gave results well within an error of 10%. Even though equation (4.11) considers extensional shear and rotary energy contributions, it is still derived from the assumption that the stator core is a thin-circular ring, which in recent studies pointed out that it may not be suffice to give accurate results on electrical machine stators having a yoke thickness-to-mean radius ratio exceeding 0.2, hence resulting an error of 14% instead. Equation (4.12) is also derived for thin-rings, where its assumed that the stator yoke thickness is very insignificant compared to its stator yoke mean radius. Equation (4.13), which is derived for thick rings, seems to be more in favour with the obtained experimental resonant frequency. Weight of the windings and insulation were neglected in the calculations, which could have contributed to the inconsistency of the computed results. Furthermore, all 3 equations do not take into account the effects of end-shields, which could increase stiffness of the motor assembly.

Finite element predicted vibration mode 2 frequency [Hz]	From equation (4.11) [Hz]	From equation (4.12) [Hz]	From equation (4.13) [Hz]
2581.57	2136.52	2273.14	2654.32
Percentage errors	17.24%	11.95%	2.82%

Table 4.5: Comparison between finite element prediction and algebraic prediction

Table 4.5 compares the finite element predicted vibration mode 2 frequency with the calculated vibration mode 2 frequency from equations (4.11), (4.12) and (4.13). Again, equation (4.13) gave a close prediction of the mechanical resonant frequency.

Hence, it can be concluded that equation (4.13) is more favourable to be used in order to predict the mechanical resonant frequency of the electrical motor stator. Although it can be argued that, some finite element packages can perform both electromagnetic and mechanical finite element analysis at the same time, it is less time consuming and less tedious by implementing the algebraic frequency equations into the electromagnetic finite element package during the electromagnetic design stage.

Next, an attempt to use equation (4.13) to predict the mechanical resonant frequency of vibration mode 2 was done on the polygon-shaped FSM. Because the polygon-shaped stator has 3 sides with different distances from the centre to the sides' mid-points, a few possible combinations of the inner radius (r_1 and r_2) and outer radius (r_3 , r_4 and r_5), as shown in Figure 4.8 that makes up a ring stator, could be fitted in and use equation (4.13) to compute their mechanical resonant frequencies. Figure 4.9 shows one example of a ring stator with the combination of r_1 and r_5 . Implementation results and comparisons with measured and finite element predicted values are shown in Table 4.6.

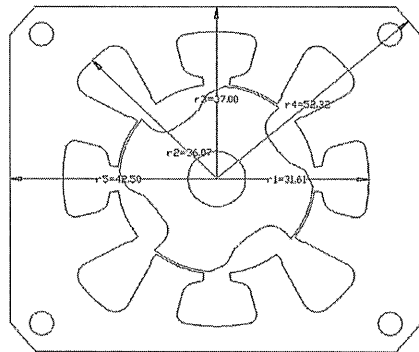


Figure 4.8: Geometric parameters for frequency equation calculation
Dimensions in millimeters. Figure not to scale.

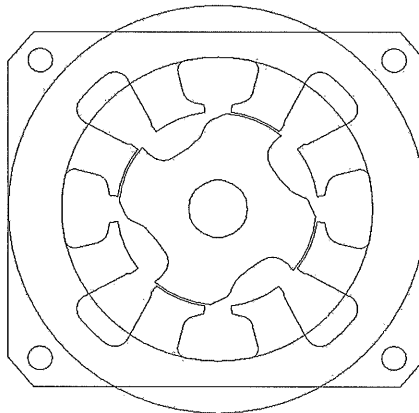


Figure 4.9: An example of a stator ring with the combination of r_1 and r_5 .

Inner radius [mm]	Outer radius [mm]	Mechanical resonant frequency, f [Hz], at mode 2	Measured vibration mode 2 frequency [Hz]	Percentage error compared with measured value	Finite element predicted vibration mode 2 frequency [Hz]	Percentage error compared with finite element predicted value
r1	r3	2870.00	3500	18%	3442.31	16.63%
r1	r4	7369.50	3500	111%	3442.31	114%
r1	r5	4969.96	3500	42%	3442.31	44.38%
r2	r3	432.09	3500	87.65%	3442.31	87.45%
r2	r4	5213.69	3500	48.96%	3442.31	51.46%
r2	r5	2049.97	3500	41.43%	3442.31	40.45%
Ave_Ir [mm]	Ave_Or [mm]	$Ave_Ir = \frac{r1+r2}{2}$, $Ave_Or = \frac{r3+r4+r5}{3}$				
33.84	43.94	4185.83	3500	19.6%	3442.31	21.6%

Young's Modulus of steel, $E=201\text{ GPa}$, Density of steel, $\rho=7930\text{ kgm}^{-3}$

Table 4.6: Table of predicted mechanical resonant frequencies with equivalent stator ring geometry

Table 4.6 tabulates the results of the mechanical resonant frequency for vibration mode 2, calculated for the polygon-shaped FSM using equation (4.13) and using 7 different combinations of the inner and outer radii of the polygon-shaped FSM. It also shows comparisons between the calculated value with the measured value obtained from Table 3.1 and finite element predicted value from Figure 4.6.

Unfortunately, not one combination of the inner and outer radii of the polygon-shaped FSM could give a satisfactory prediction of the mechanical resonant frequency at vibration mode 2. An obvious reason would be that, since equation (4.13) was derived from thick rings, it can only be suitably used to predict the mechanical resonant frequency of round-shaped stator laminations.

4.5 Summary

From Table 4.1 the mechanical finite element package predicted the vibration resonant frequencies for the round-shaped and polygon-shaped FSM close enough to the measured mechanical resonant frequencies for a vibration mode of 2. Mismatch of results, could probably be due to mismatch in constraints on the finite element model, and windings wound on the stator were not considered in the modeling or calculation. Windings could act as dampers, and were suggested to be additional mass to the stator. Weight of end-caps that hold the stator could be modeled as extra forces on the laminations.

The use of simplified frequency equations to predict the resonant frequencies of round-shaped stator laminations was implemented into OPERA. Three of the simplified frequency equations were implemented into OPERA, where 2 of them gave values of calculated resonant frequencies of $m=2$,

well within a 10% error as shown in Table 4.3. The simplified frequency equation derived for thick-rings, equation (4.13), is more favorable and considered more accurate, since its predicted value of 2654.32Hz is close to experimental and finite element predicted results as shown in Table 4.4 and Table 4.5.

As shown in Table 4.6, the calculated mechanical resonant frequencies of the polygon-shaped stator for mode 2, using equation (4.13), does not at all predict the measured mechanical resonant frequency and finite element predicted mechanical resonant respectively. This suggests that the frequency equations for round-shaped stators can not be used as simple approximate equations to predict the mechanical resonant frequencies of any other shapes. The 700Hz vibration frequency, as observed in Figure 3.16 and Figure 3.17, was not extracted in finite element. This could suggest that the 700Hz wasn't induced by the motor, but of the vibration of the motor housings since the housing has smaller stiffness than the motor lamination.

The vibration mode shape and its corresponding mechanical resonant frequency that were predicted by the mechanical finite element analysis were more favourable than to the derived algebraic equations. However, these algebraic equations could serve to give a vague but important idea of what the mechanical resonant frequency could be during the electromagnetic design stage.

Some work on derivation of the polygon-shaped stator laminations could be made, starting from predicting resonant frequencies for box structures using plate theories, as done in [30,31]. These frequency equations are derived from energy methods involving matrix calculations and solving tedious partial differentiations, which could not be simply implemented in electromagnetic finite element packages for the objective to predict the stator lamination profile's mechanical resonant frequencies during the electromagnetic design stage. Simpler frequency equations could be derived for straightforward implementations, as done for round-shaped stator structures, in order to give a rough idea of the resonant frequencies during the electromagnetic design stage.

Chapter 5

THE PERMANENT MAGNET FLUX SWITCHING MOTOR: THE INTERNAL ROTOR VERSION

5.1 Introduction

This chapter and the preceding chapter will present the design and development of an alternative brushless permanent magnet motor used in low energy consumption fan applications, known as the Permanent Magnet Flux Switching Motor (PMFSM). The PMFSM, derived from the Flux Switching Motor (FSM) with a conventional field winding described in [1] and also seen in previous chapters, retains the robustness and ruggedness of the flux switching motor and switched reluctance motor, and benefits from the permanent magnets to improve efficiency, because having no field windings, no additional power is needed to produce field flux.

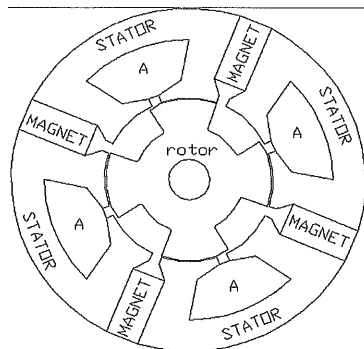


Figure 5.1: A permanent magnet flux switching motor, PMFSM.

Slots denoted as 'A' are armature winding slots

The PMFSM is to be introduced as an alternative to the classical brushless DC (BLDC) as a high efficiency, low-cost brushless motor. BLDCs have long since existed and many studies have been done which showed promising improvement of efficiency and reliability because of the use of permanent magnets [32], [33]. However, most of the placements of the permanent magnets in BLDCs are on the rotor pole surface, embedded in the rotor poles or be the rotor on its own. Unlike the BLDC, the PMFSM has its permanent magnets placed as part of the stator, which basically replaces the conventional field windings in the FSM, and interacts with a fully pitched armature winding as shown in Figure 5.1. Similar stator structures were presented in [34] introducing the flux-switch phenomenon in an alternator. Other authors in [35] have employed similar permanent

magnet and stator configurations on a 4/6 doubly salient permanent magnet motor. Some tests results were published in [36] for a motor with permanent magnets in the stator.

An Internal Rotor version and an External Rotor version of the PMFSM will be presented in this and the preceding chapter respectively. Both versions of the PMFSM have permanent magnets as part of the stator structure which also contains armature windings, and a rotor which is a simple steel, salient pole structure. The permanent magnets used are ferrite magnets, due to its low cost advantage. Both versions of the PMFSM have the same permanent magnet configuration. The main aim is to produce a trapezoidal back-EMF waveform in order to have smooth running torque when square-wave armature current is applied which consequently leads to reduction in vibration and acoustic noise. Self-start capability in the desired direction was achieved by modifying the rotor lamination profile to give the required amount of asymmetry. However, the PMFSM will possess different vibration characteristics from the vibration investigations seen in the previous chapters, because of the significant difference on the stator structure.

The electromagnetic finite element package, Vector Fields OPERA, was used to assist in producing a stator lamination and magnet configuration that can produce a trapezoidal back-EMF waveform, while a spreadsheet was used to predict the dynamic performance of the PMFSMs with DC armature current applied. Simulation and experimental results will show that both the proposed PMFSMs can be more efficient and less noisy when compared with an existing 3-phase BLDC and induction motor. Before the design of the new PMFSM commences, the evolution of the PMFSM from the FSM is illustrated next.

5.2 Evolution of the PMFSM

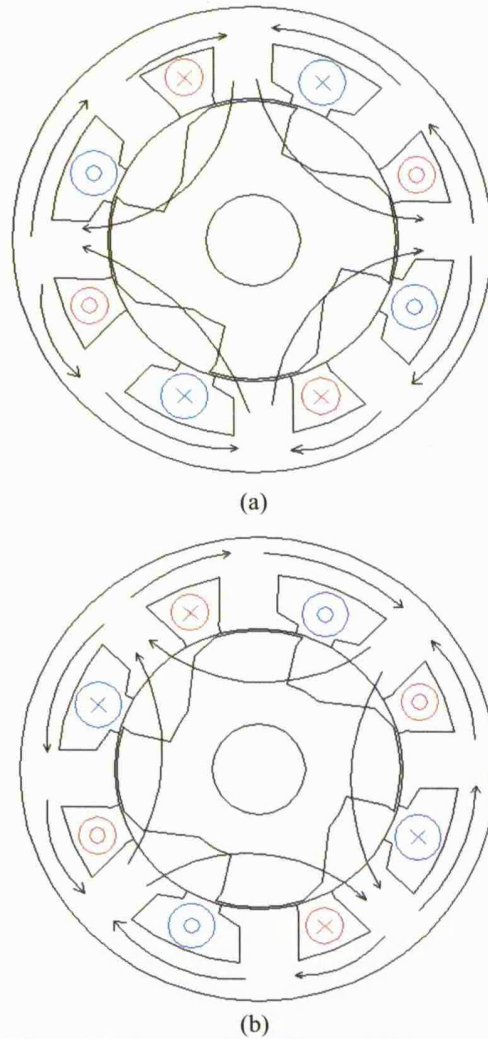


Figure 5.2: A conventional flux switching motor.

(Blue conductor: Armature winding, Red conductor: Field winding. Arrows show total flux direction.)

Figure 5.2 shows a conventional flux switching motor with both field and one of the bifilar armature windings energized on the stator lamination. Figure 5.2(a) has one direction of armature current applied, Figure 5.2(b) has the armature current applied in an opposite polarity from Figure 5.2(a). During normal operation of the flux switching motor as described in [1], regardless of the change in armature flux direction, there are 4 sections on the stator back iron behind the field winding slots where the flux direction does not change, and has its unique direction, as shown in Figure 5.2. It was then proposed that these 4 sections of the stator back iron be replaced by permanent magnets, magnetized in the same unique directions as shown in Figure 5.3, to give the permanent magnet flux switching motor, PMFSM.

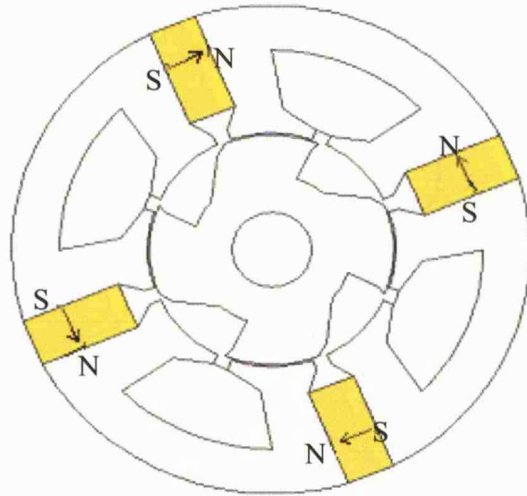


Figure 5.3: Proposed permanent magnet configuration

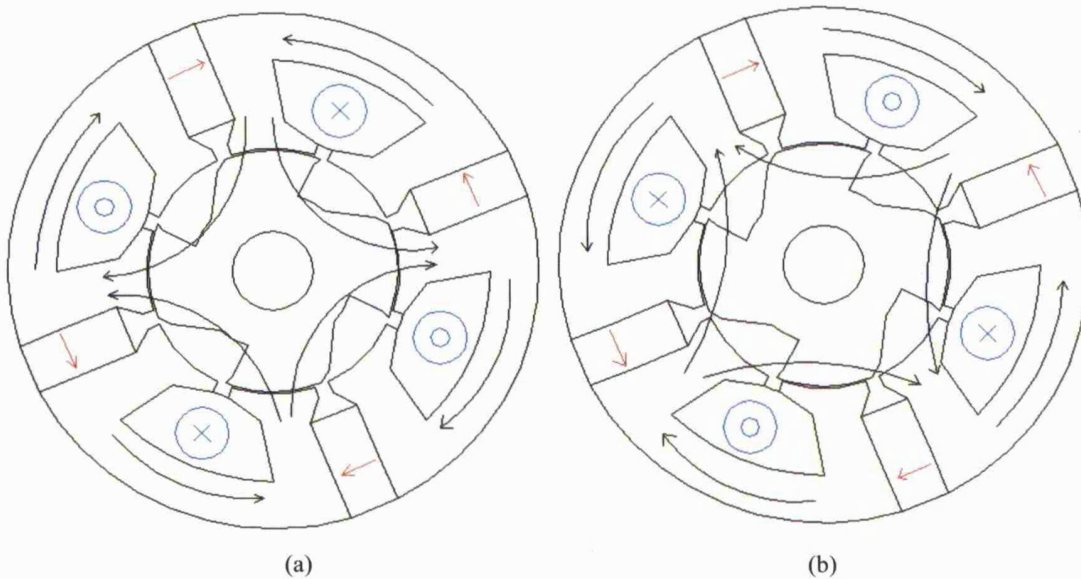


Figure 5.4: A permanent magnet flux switching motor

(Blue conductor: Armature winding. Red arrows: Magnet magnetization direction. Black arrows show total flux direction.)

The principle operation of the flux switching motor with the new permanent magnet configuration is the same as described in [1] having the armature windings wound as bifilar windings to give a low cost electronic circuit. Figure 5.4(a) and (b) show the flux directions of the permanent magnet configuration, with one of the bifilar armature windings energized. Comparing the flux directions in Figure 5.4(a) and (b) with the ones in Figure 5.2(a) and (b) respectively, it can be seen that the flux directions are identical, further verifying the concept of replacing the field windings by permanent magnets placed as part of the stator profile.

5.3 Electromagnetic finite element design

The electromagnetic finite element package used is called Vector Fields OPERA. From the electromagnetic finite element package, one can simulate and compute the average flux and then produce the back-EMF waveform. According to Faraday's Law, the back-EMF voltage due to the permanent magnet flux is

$$e = -N \frac{d\psi}{dt} \quad (5.1)$$

The armature current is predicted using equation (5.2),

$$i_{n+1} = i_n + (V_s - i_n R - e_a) \frac{\Delta t}{L_n} \quad (5.2)$$

$$\text{where } L_n = \frac{\psi_{n, F_{2n}} - \psi_{n, F_{1n}}}{F_{2n} - F_{1n}} \quad (5.3)$$

where Δt is the time interval; L_n is the n th machine inductance at n th rotor angle; F_{2n} is the total MMF of magnitude F_2 applied to windings at n th rotor angle; $\psi_{n, F_{2n}}$ is the flux linkage magnitude due to F_2 at n th rotor angle; F_{1n} is the total MMF of magnitude F_1 applied to windings at n th rotor angle; $\psi_{n, F_{1n}}$ is the flux linkage magnitude due to F_1 at n th rotor angle; R is the armature winding resistance; V_s is the supply voltage; e_a is the back EMF voltage of armature; i_n : n th current for n th rotor angle. In the spreadsheet, e_a was obtained in MATLAB using the armature flux computed in OPERA and the equation

$$e_a = 6Nn_{rpm} \frac{d\psi}{d\theta} \quad (5.4)$$

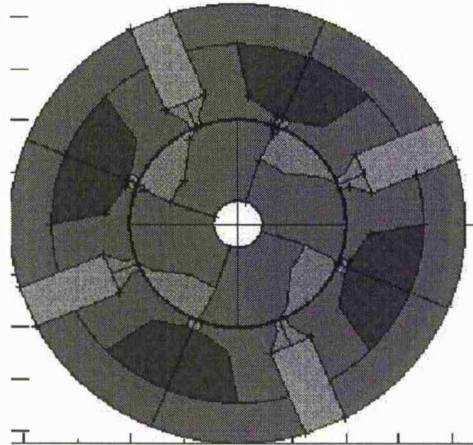
and then fed into the spreadsheet.

The spreadsheet, however, was not capable of predicting the iron loss during running operation, as all losses are assumed to be contributed by copper loss.

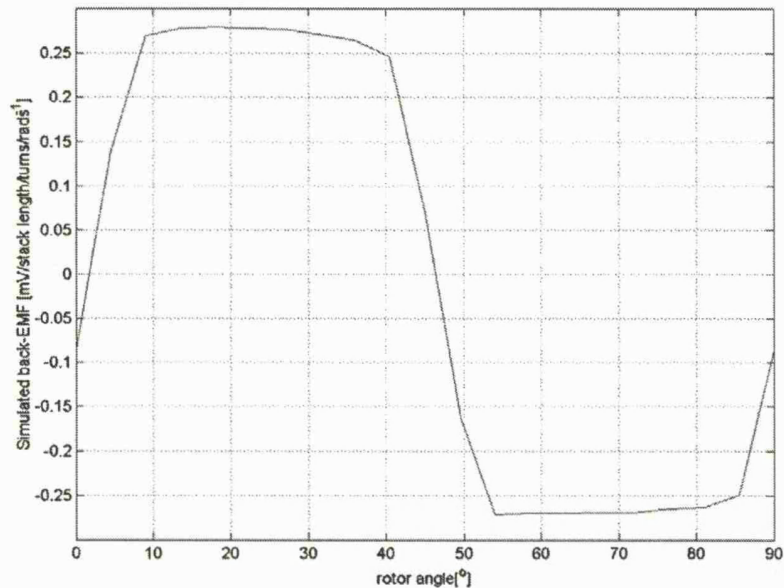
5.4 Design of the internal rotor permanent-magnet flux switching motor

Different lamination profiles were modeled and the shapes of their back-EMF waveforms were predicted. The direction of magnetization of the permanent magnets used in the simulation was the same as shown in Figure 5.3.

Figure 5.5(a) shows the internal rotor PMFSM, referred here as INTPMFSM 1.



(a): INTPMFSM 1 at rotor position of 0°

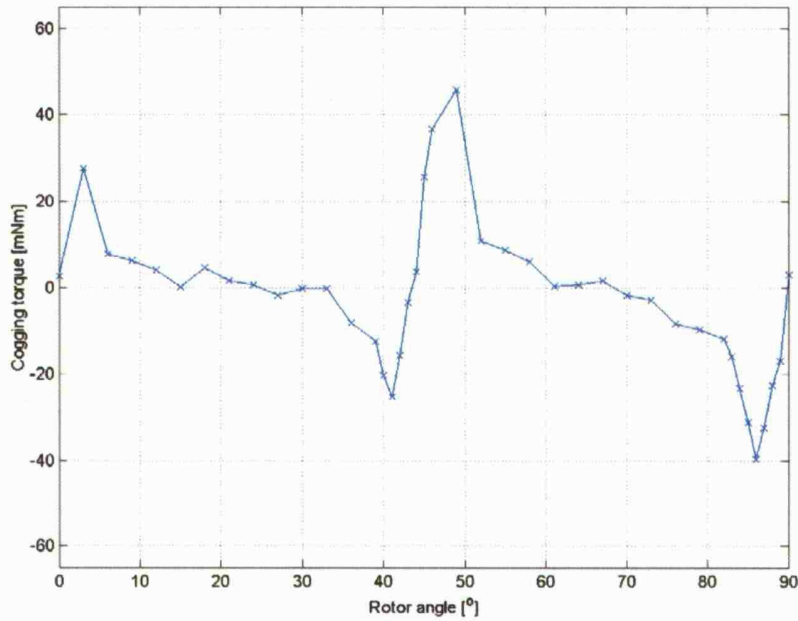


(b) Simulated back-EMF waveform

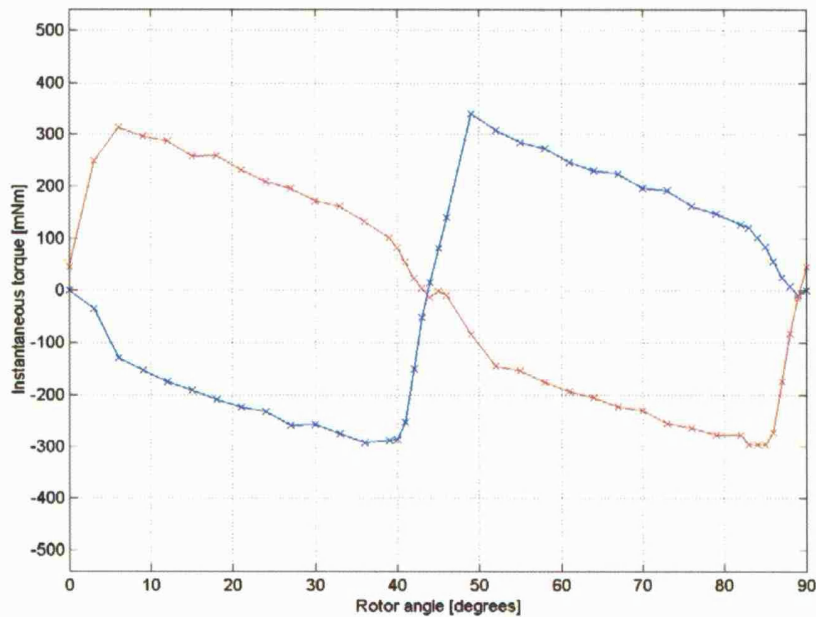
Figure 5.5: Back-emf of INTPMFSM 1

It can be seen from Figure 5.5(a) that the stator has a stiff lamination structure, with a thick back iron and thick stator teeth. This could increase stiffness, and also decrease iron losses at the back iron. To ensure the machine is able to start, the design was checked to ensure that the profile of the armature static torque (due to positive and negative MMF respectively) versus rotor angle did not have coincident zero torque regions.

Here, the instantaneous torque waveforms with DC armature current were investigated on INTPMFSM 1. Asymmetric airgap is introduced by modifying the rotor lamination profile. In the simulation, *the positive torque is taken to be counter-clockwise torque and vice versa.*



(a) Cogging torque for INTPMFSM 1

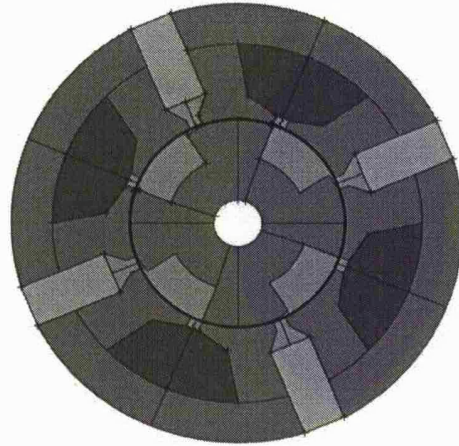


(b) Simulated at DC Armature MMF 400A-turns(blue line) and -400A-turns(red line)

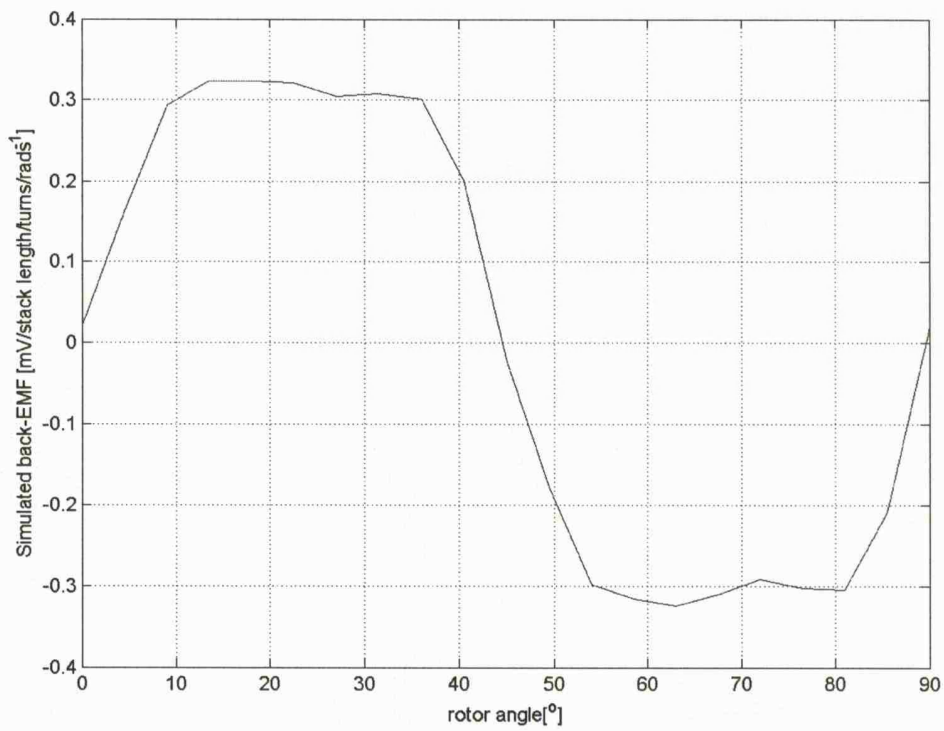
Figure 5.6: Simulated torque waveforms for INTPMFSM 1

In Figure 5.6(a) and Figure 5.6(b) show the cogging torque and the instantaneous torque when positive or negative DC armature current is applied for INTPMFSM 1 respectively. In Figure 5.6(a), there is a rotor position at 43° where the rotor rests when no armature current is applied. At this rotor position in Figure 5.6(b), the instantaneous is near zero. This indicates that there is a chance INTPMFSM 1 will not start, even with armature current is applied if the rotor rests at this rotor position.

Consequently, the rotor lamination profile of the proposed internal rotor design, INTPMFSM 1, had to be reconfigured. The rotor lamination of INTPMFSM 1 was further modified. The final design is as shown in Figure 5.7(a).

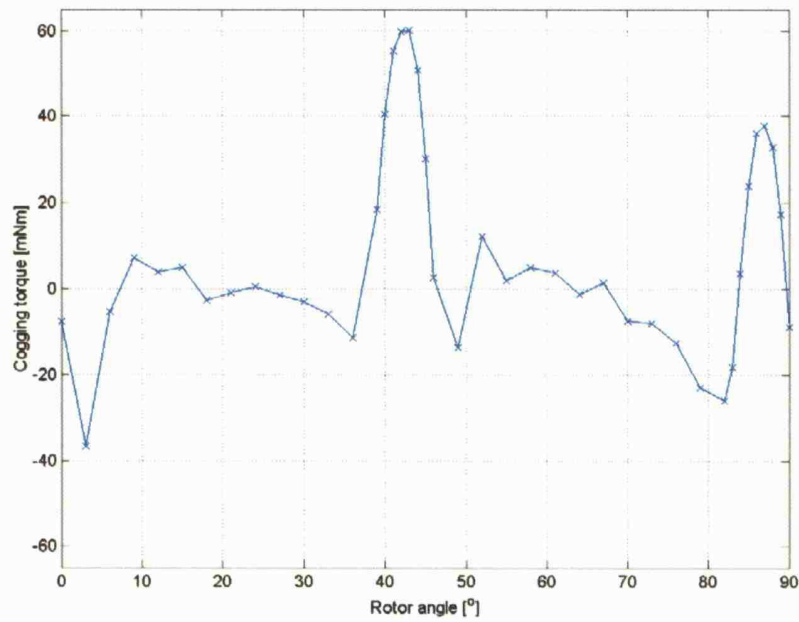


(a) INTPMFSM 2 at rotor position of 0°

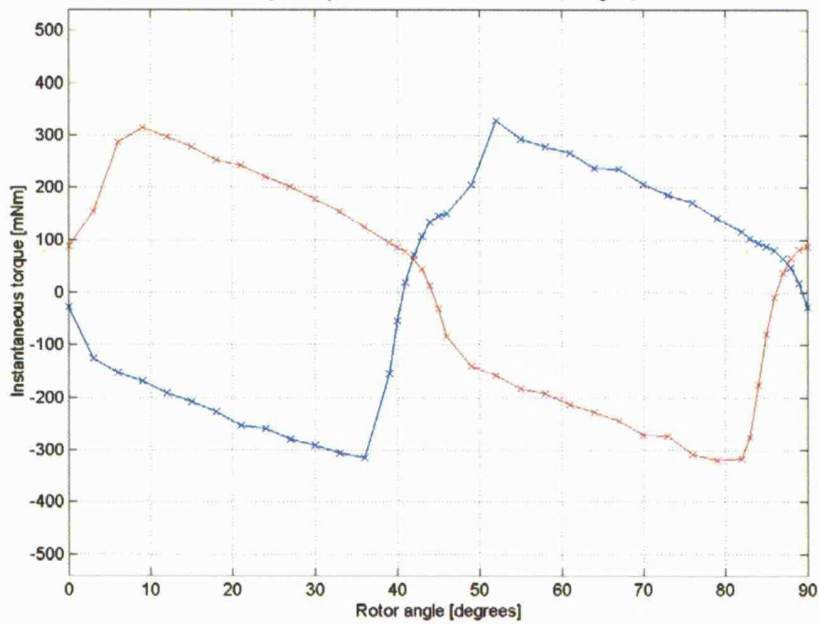


(b) Simulated back-EMF for INTPMFSM2

Figure 5.7: Modified INTPMFSM 2



(a) Cogging torque for INTPMFSM 2



(b) Instantaneous torque for internal rotor

Simulated at DC armature MMF 400A-turns (Blue line) and -400A-turns (Red line)

Figure 5.8: Simulated torque waveforms for INTPMFSM 2

Figure 5.8(a) and (b) show the cogging torque and the instantaneous torque when positive or negative DC armature current is applied respectively. Figure 5.8(a) shows that the rotor rests at rotor positions where cogging torque is zero. Figure 5.8(b) shows that at the rotor positions where the rotor rests, a positive instantaneous torque exists regardless of the polarity of DC armature

current applied, indicating that the rotor will definitely be able to move out of its resting positions. Furthermore, this final design retains the desired trapezoidal back-EMF waveform, as shown in Figure 5.7(b). This was chosen to be the proposed internal rotor PMFSM design, referred to as INTPMFSM 2.

Table 5.1 gives a comparison of the performance among the induction motor, 3-phase BLDC and the internal rotor design (INTPMFSM 2). The maximum running speed of the 3-phase BLDC was 1731rpm. It clearly shows that the internal rotor design (INTPMFSM 2) is capable to perform better than the induction motor and the BLDC at the varying speeds.

Table 5.1: Comparison of performance among IM, BLDC, and INTPMFSM 2

	Average speed [rpm]	Average voltage applied [V]	Average input power [W]	Average output power [W]
INTPMFSM 2 (Predicted)	708	33	1.58	1.19
	1352	68	10.43	8.26
	1731	125	23.43	17.34
	2168	240	62.21	34.07
3-phase Brushless DC (Measured)	708	240	9.00	1.19
	1352	240	16.6	8.26
	1731	240	24.6	17.34
Induction motor (Measured)	981	240	36.43	3.15
	1350	240	54.57	8.23
	1733	240	74.45	17.40
	2168	240	86.31	34.07

From the spreadsheet simulation, the suggested armature winding diameter to be used is 0.2mm, 476-turns for each bifilar strand in the internal rotor PMFSM (INTPMFSM 2), where each strand has 2 coils in series wounded in the same direction.

5.5 CAD design

The final CAD design and some explanation of certain aspects of the parts is given, with the dimensioned drawings presented in Appendix E. All the CAD designs of most of the motor parts were done in ProEngineer Wildfire. The end-caps and stator housings have to fit into the existing fan housing, with a limited axial length of 118.25mm. The outer diameter of the stator housing cannot exceed 90mm. Furthermore, the existing gap between the existing stator housing and fan blade housing has to maintain at 11.85mm. By using the same housing, it was hoped that a valid acoustic comparison could be achieved between fans powered by different motors. Assembly procedures were somewhat tedious as stator laminations were loose pieces, and keeping the stator laminations concentric as a circle is of great challenge.

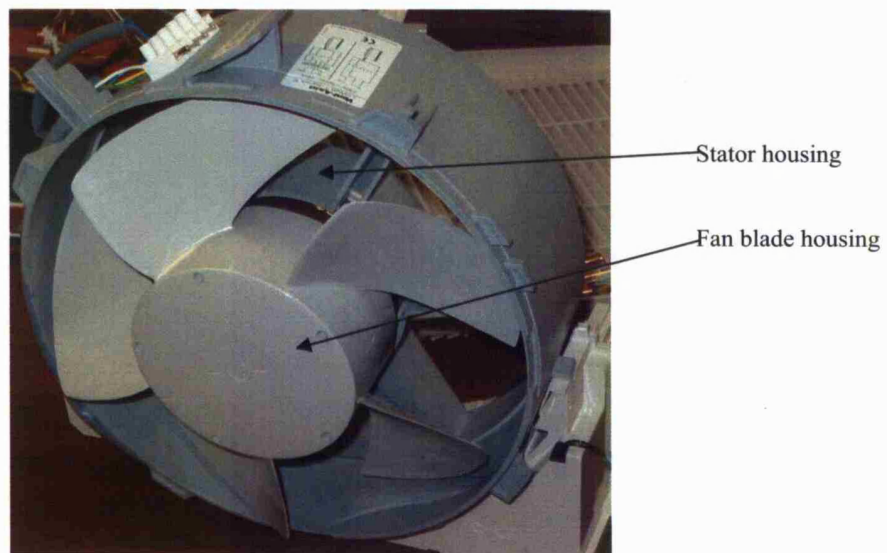


Figure 5.9: Existing ventilation fan with 3-phase brushless DC motor

Table 5.2 below shows some of the main dimensions of INTPMFSM 2. Figure 5.10 show the winding configuration for INTPMFSM 2.

Table 5.2: Main dimensions for INTPMFSM 2
All dimensions subject to ± 0.01 mm, unless stated otherwise.

	External rotor 3-phase Brushless DC BLDC	Internal rotor PMFSM INTPMFSM 2
Stator outer diameter [mm]	75.98	85
Stator inner diameter [mm]	24.2	40.6
Rotor outer diameter [mm]	92.3	40
Rotor inner diameter [mm]	76.75	Shaft diameter
Airgap [mm]	0.385	0.3
Stack length [mm]	25.5	26
Shaft diameter [mm]	8	10
Number of stator poles	6	8
Number of rotor poles	6	4
Volume of all magnets [mm ³]	54856.36	14205.6
Number of turns per strand of bifilar winding, N	Not known	476
Number of coils in series per strand of bifilar winding	Not known	2
Number of coils in parallel	Not known	1
Winding diameter [mm]	Not known	0.2
Winding packing factor	Not known	0.125

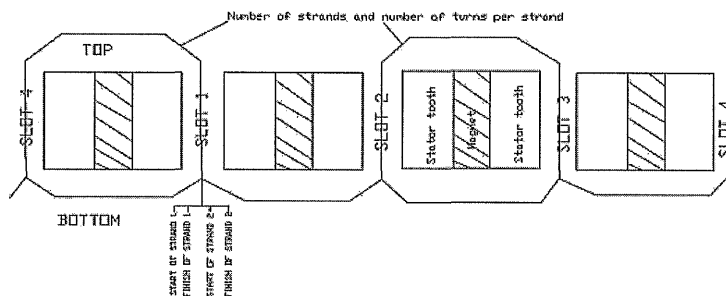


Figure 5.10: Winding configuration for PMFSM

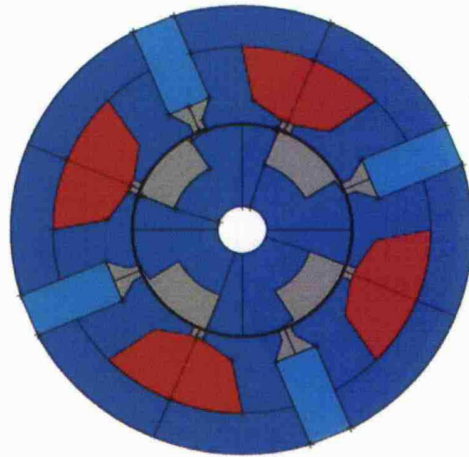


Figure 5.11: Internal rotor PMFSM, INTPMFSM 2

In the CAD drawings, the sharp edges of the stator laminations shown in Figure 5.11 were rounded off with 0.1mm radius. This in practice could reduce the concentration of high flux density, which then reduces hysteresis loss.

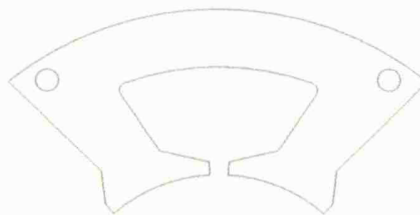


Figure 5.12: Stator lamination of INTPMFSM 2

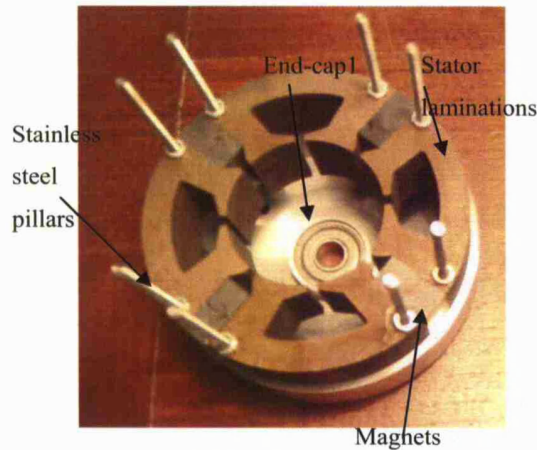


Figure 5.13: Partly assembled INTPMFSM 2

Extra holes were made on the stator lamination of INTPMFSM 2, as shown in Figure 5.12, in order to slide the laminations into place through stainless steel pillars. The stainless steel pillars were screwed into the end-cap, so that when the stator laminations were slid through the pillars, the magnets and laminations will be in a concentric circle as shown in Figure 5.13.

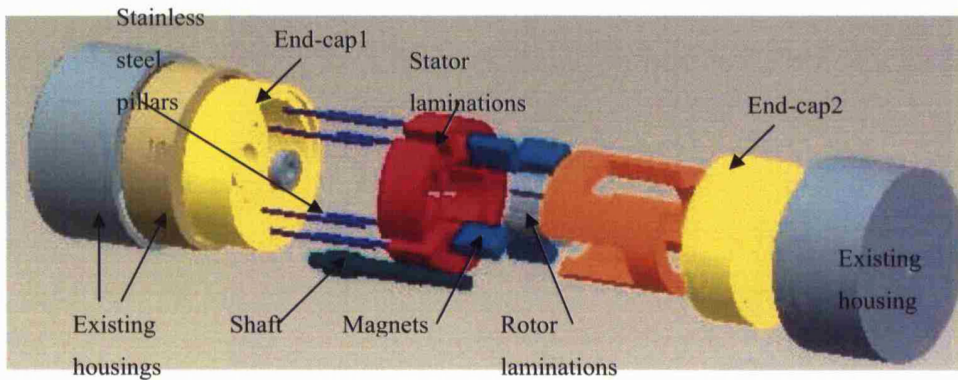


Figure 5.14: Exploded CAD drawing of INTPMFSM 2

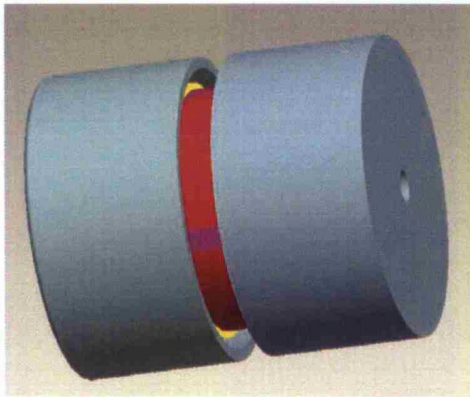


Figure 5.15: Assembled view with existing components

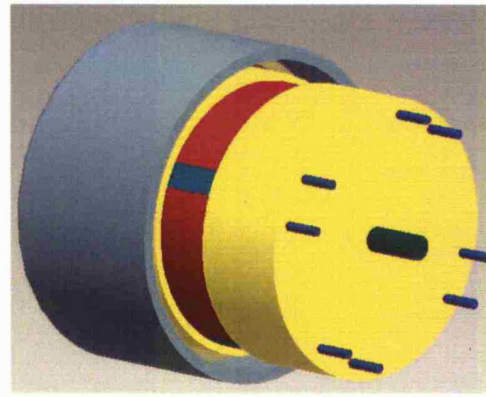


Figure 5.16: Assembled view of INTPMFSM 2

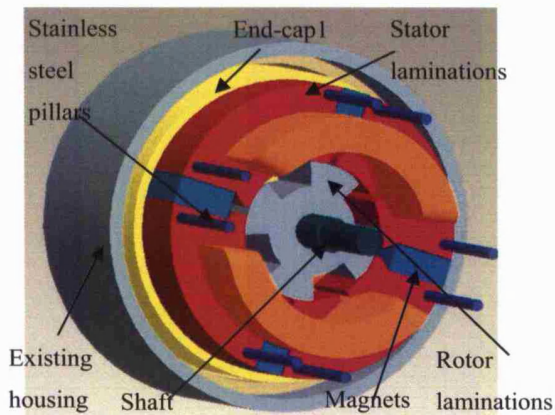


Figure 5.17: View showing rotor-shaft assembly with other components

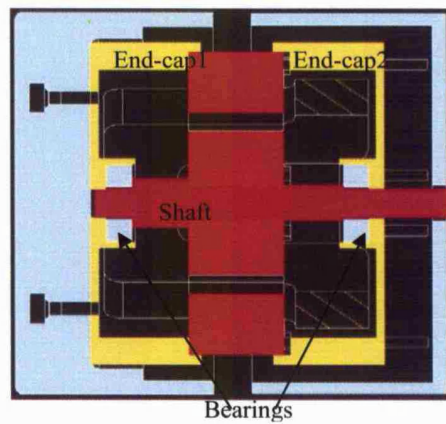


Figure 5.18: Assembled section view of INTPMFSM 2

For INTPMFSM 2, the shaft had multiple flanges to locate the bearing positions and rotor lamination position. Both end-caps are securely fastened axially by 8 stainless steel pillars with nuts at the top end-cap (end-cap2). The bottom end-cap (end-cap1) is fastened onto the existing housing which once housed the existing BLDC.

Photos of the final prototype assembly are shown in Appendix F. Some problems that occurred during and after the assembly of both the prototypes were such as loose fastening of the fan blade housing to the shaft, sensor circuit board replacement on the INTPMFSM 2.

For INTPMFSM 2, the shaft was not long enough to have the fan blade housing securely fastened onto the shaft. Hence, it was then decided to abandon the whole opto-sensor circuit board in order to make more space to securely fasten the fan blade housing onto the shaft. A reflective sensor OPB706B was used, in replacement of the opto-sensor, which was fastened onto the side of the stator housing and having the fan blade housing itself acting as the sensor interrupter, with both reflective and non-reflective tapes on it spanning every 45° apart between each similar tape, as shown in Figure 5.19. The fan blade housing was fixed onto a 30mm long, 20mm diameter boss which has two 3mm grub screws to fasten the fan blade housing onto the shaft. In addition to this, the distance between the sensor and the fan blade housing has to be within a range so that the sensor signal can provide a distinct 5V-amplitude pulsating signal. The reflective sensor circuit schematic is shown below in Figure 5.20.

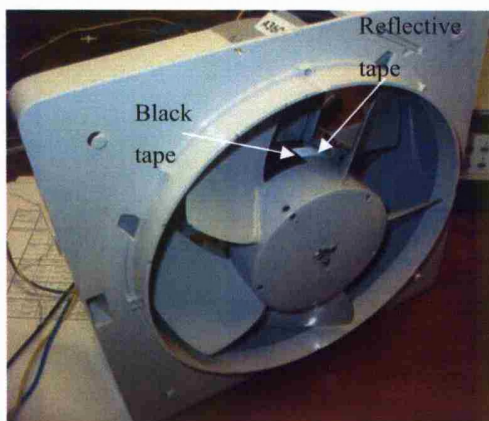


Figure 5.19: Fan blade with reflective and non-reflective tapes to act as sensor interrupter

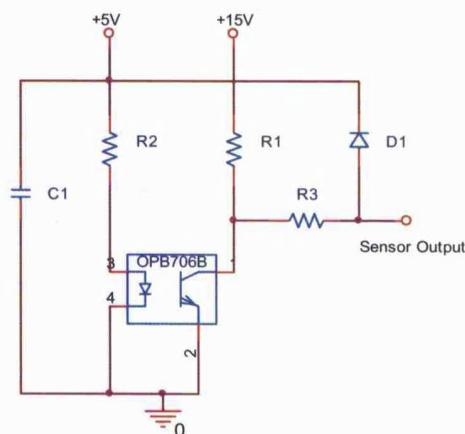


Figure 5.20: Opto-sensor circuit schematic.
For this application, $C1= 100\mu\text{F}$, $R2=120\Omega$,
 $R1=15\text{k}\Omega$. $R3=1\text{k}\Omega$.

In Figure 5.20, R1 and R2 determine the operating current of the transmitter and the receiver respectively. R3 is to limit the output current to the PIC microcontroller. D1 is there to clamp the output sensor voltage from 15V to 5V. C1 is to ensure a stable 5V supply to the transmitter.

5.6 Experimental tests on the internal rotor PMFSM, INTPMFSM 2

The investigation of the performance and acoustic noise on INTPMFSM 2 was carried out experimentally and results are presented here. Furthermore, comparisons of the dynamic performance between the existing 3-phase BLDC, induction motor and INTPMFSM 2 will also be shown. The power converter drive that drives INTPMFSM 2 consists of two power switches as shown in Figure 5.21. Armature 1 and Armature 2 combines to create bifilar windings, magnetically coupled to one another. Dots indicate the start of winding direction of the windings.

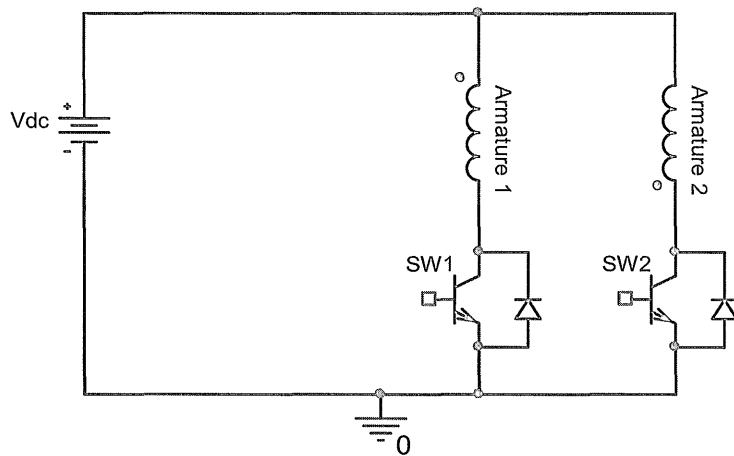
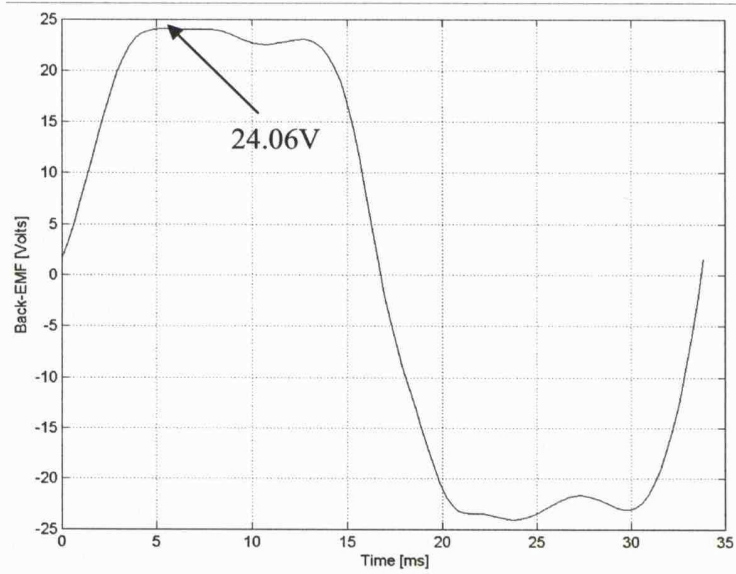
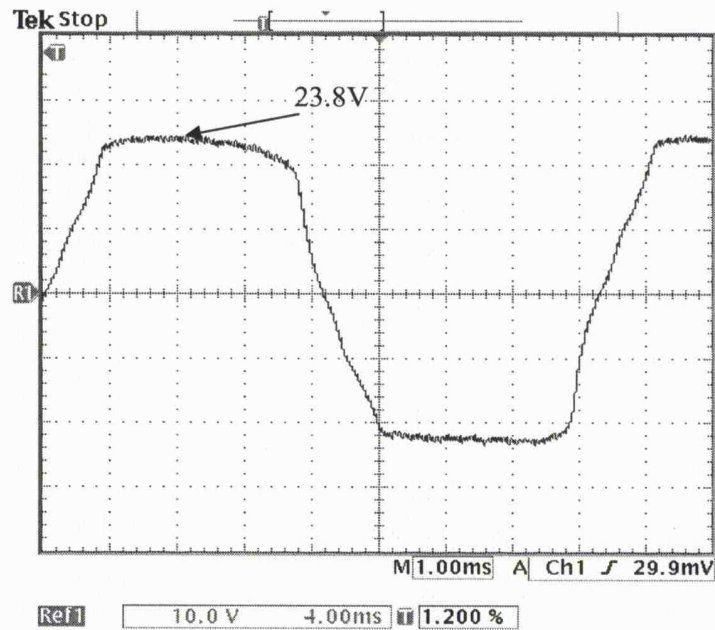


Figure 5.21: Power converter schematic driving both PMFSM prototypes



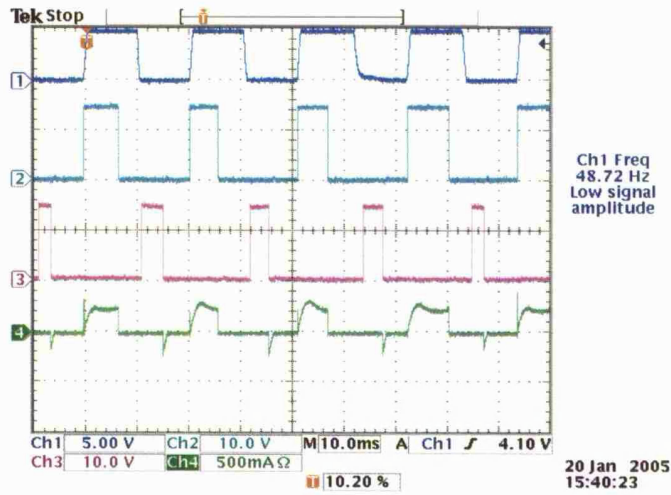
(a) Simulated back EMF



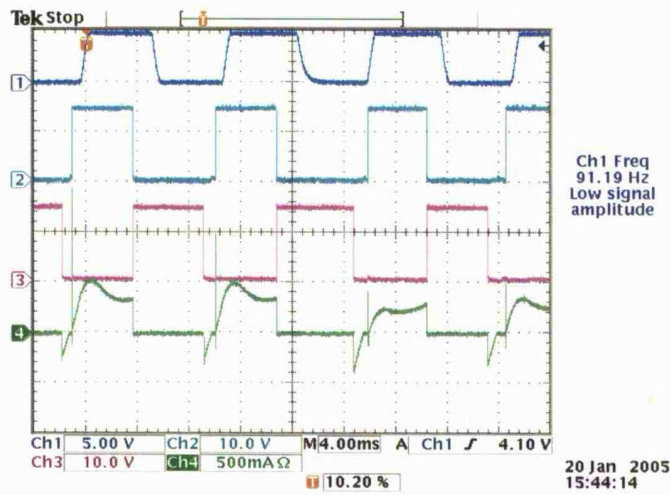
(b) Experimental back EMF

Figure 5.22: Comparison of back EMF from simulation and experiment of INTPMFSM 2 at 443rpm

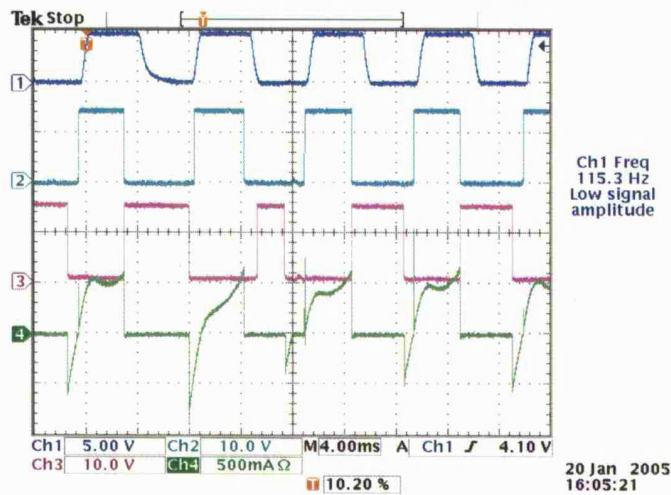
Figure 5.22(a) shows the back-EMF waveform from simulation of INTPMFSM 2 at 443rpm, whereas Figure 5.22(b) was obtained when the rotor was spun at approximately 443rpm. They show good agreement with each other.



(a) Waveforms at 715rpm, 54Vdc, Power input = 7.20W



(b) Waveforms at 1359rpm, 76.62Vdc, Power input=24.63W



(c) Waveforms at 1735rpm, 132.6Vdc, Power input=62W

Channel 1: Sensor; Channel 2: Switch 1; Channel 3: Switch 2; Channel 4: Armature current (0.5A/div)

Figure 5.23: Waveforms of INTPMFSM 2 at 3 different speeds

	Existing BLDC			Internal rotor PMFSM, INTPMFSM 2 (Predicted)			Internal rotor PMFSM, INTPMFSM 2 (Measured)		
Average speeds [rpm]	1735	1352	708	1731	1352	708	1735	1339	715
Average voltage applied [V]	240	240	240	125	68	33	132.6	76.62	54
Average input power [W]	24.6	16.6	9	23.43	10.43	1.58	62	24.63	7.20
Average output power [W]	17.46	8.26	1.19	17.34	8.26	1.19	17.46	8.03	1.22
Sound power [dB]	60.7	54	43	No available simulation			69.2	62	53

Table 5.3: Comparisons of results between BLDC and INTPMFSM 2

From Table 5.3, initial experimental results from the internal rotor PMFSM show that it is more efficient than the BLDC at low speeds of 715rpm. However, at higher speeds of 1735rpm, the armature current of INTPMFSM 2 was increasing at turn-off as shown in Figure 5.23(c), indicating that negative torque was being produced. The turned on angle should be advanced to obtain better efficiency. The current was not smooth as well, as significantly seen in Figure 5.23(b), probably due to small DC link capacitance. Furthermore, the experimental results were not very close to the predicted results. Measurement on the winding mean length of turn was done, and was found that the mean length of turn on the actual motor, about 168mm, was longer than the predicted result which was 121mm. This suggests that copper loss in the actual motor will be larger than predicted.

	Existing BLDC			Internal rotor PMFSM, INTPMFSM 2 (Predicted)			Internal rotor PMFSM, INTPMFSM 2 (Measured)		
Average speeds [rpm]	1735	1352	708	1731	1339	715	1735	1339	715
Average voltage applied [V]	240	240	240	132.6	76.6	54	132.6	76.62	54
Average input power [W]	24.6	16.6	9	28.65	13.35	7.61	62	24.63	7.20
Average output power [W]	17.46	8.26	1.19	17.34	8.03	1.22	17.46	8.03	1.22
Sound power [dB]	60.7	54	43	No available simulation			69.2	62	53

Table 5.4: Comparisons of results between BLDC and INTPMFSM 2 with modified predicted results

In Table 5.4, with a value of the mean length of turn closed to the actual value applied to the spreadsheet, predicted results were closer to the experimental results, particularly at low speed. There are still mismatch between predicted and measured results. Iron losses and temperature rise in the windings, that were neglected in the simulation, could be the reason why the mismatch and why more power was consumed by the motor, since iron losses is proportional to the rate of change of flux density which increases with speed, and at higher speeds, current increases which heats the windings further, and hence increasing the resistance of the winding, and then consequently increasing copper losses.

Unfortunately, INTPMFSM 2 is noisier than the BLDC. This could be due to the eccentricity of the rotor, which is easily observed. INTPMFSM 2 also had loose laminations as the end-caps could have failed to hold them securely.

5.7 Summary

In conclusion, the internal rotor version of the PMFSM has been designed, built and tested. Table 5.4 shows that the internal rotor PMFSM is capable of consuming less input power than the existing BLDC at low speeds, and more improvement can be done in power electronic drive control and mechanical assembly in order to improve efficiency at higher speeds, and reducing vibration and noise respectively. The preceding chapter will show the design and test on the external rotor version of the PMFSM, which is expected to consume much less input power than the BLDC and the internal rotor PMFSM.

Chapter 6

THE PERMANENT-MAGNET FLUX SWITCHING MOTOR: THE EXTERNAL ROTOR VERSION

6.1 Introduction

This chapter illustrates the design and prototype development of the external rotor version of the PMFSM, as shown in Figure 6.1, that will compete with the existing brushless DC and induction motor for fan applications. Again, the main aim is to increase efficiency using permanent magnets, and to produce a trapezoidal armature back-EMF waveform so that when square-wave armature current is applied, smooth running torque can be produced in order to reduce noise and vibration. It is expected that the external rotor PMFSM will be more efficient than the internal rotor PMFSM, because an external rotor configuration produces a larger airgap volume. It is also believed that the external rotor configuration can have its stator held more securely towards the centre of the machine, which will increase the stiffness of the stator part. Furthermore, any permanent magnet leakage flux will be confined within the motor, reducing the loss of flux. However, another challenge will be keeping the centre of external rotor part aligned with the axis of the shaft, in order to minimize rotor eccentricity, which could be a dominant source of vibration, rather than the stator being the dominant source of vibration. The electromagnetic finite element package mentioned in section 5.3 was used to assist in modeling different lamination profiles and predict the shape of the back-EMF. The direction of magnetization of the ferrite permanent magnets used in the simulation is the same as shown in Figure 5.3(a).

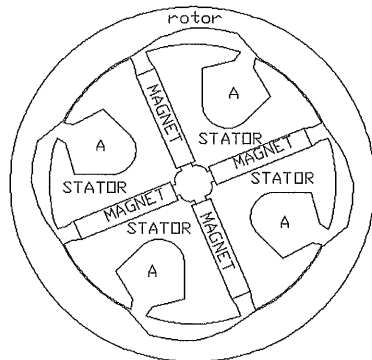
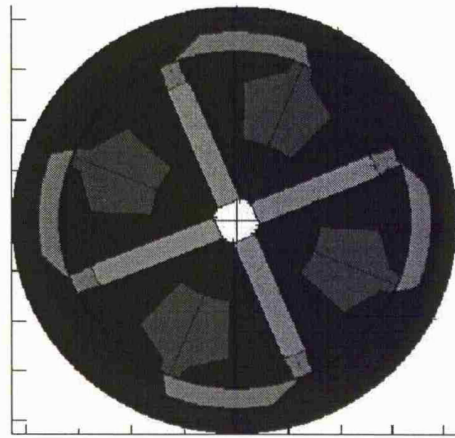


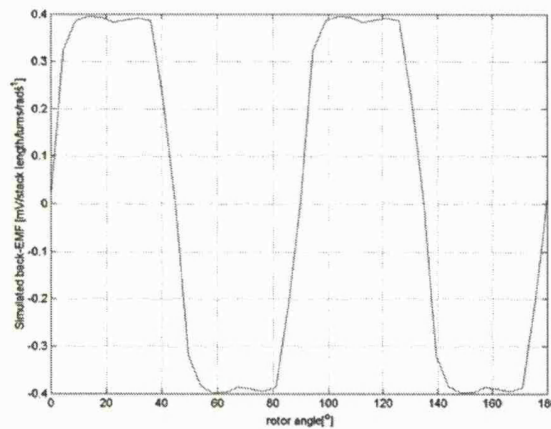
Figure 6.1: External rotor version of PMFSM
Slots denoted as 'A' are armature winding slots

6.2 Design of the external rotor permanent-magnet flux switching motor

Different lamination profiles were modeled and the shapes of their back-EMF waveforms were predicted. For the external rotor PMFSM, the initially proposed machine is shown in Figure 6.2(a) below. This design is referred to as EXTPMFSM 1.



(a) EXTPMFSM 1 at rotor position of 0°

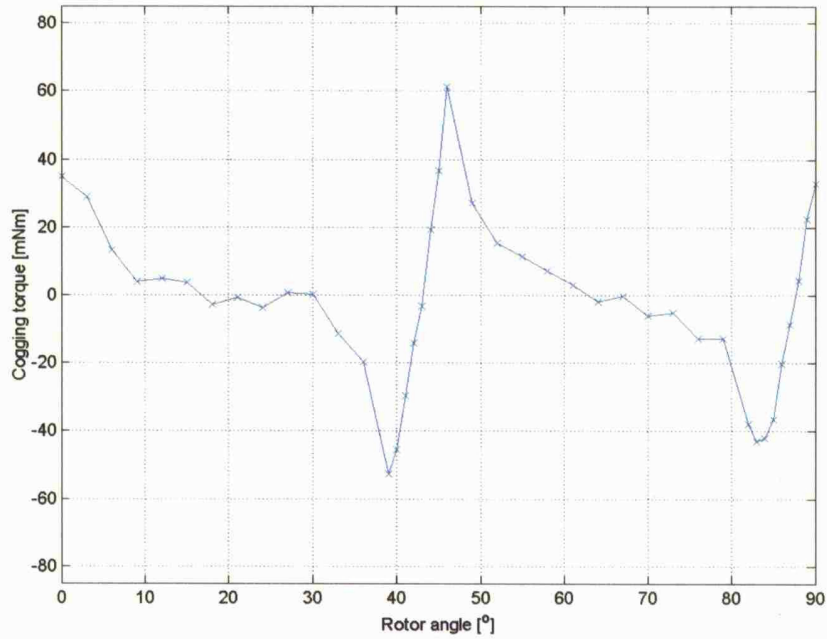


(b) Simulated back-EMF waveform

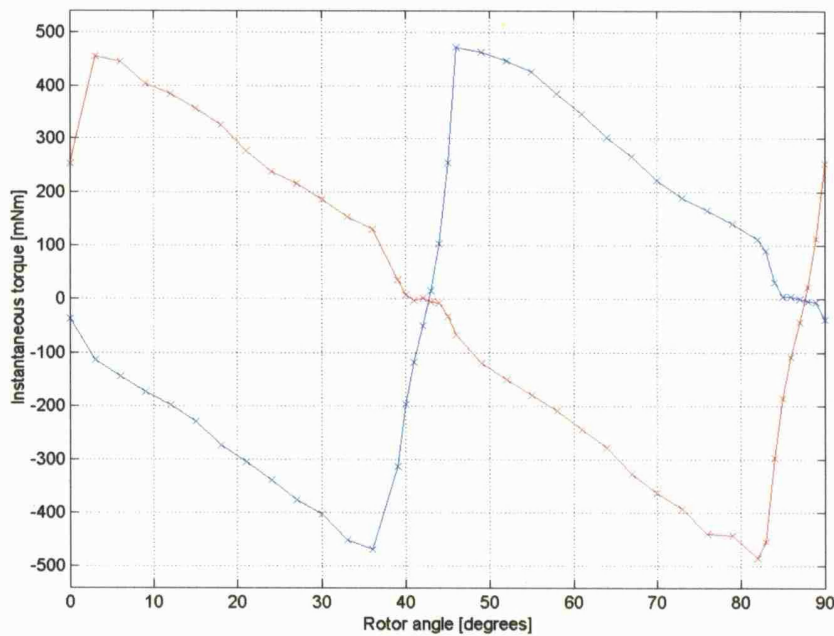
Figure 6.2: Back-emf and armature flux of EXTPMFSM 1

Next, to ensure the machines are able to start, the designs were checked to ensure that the profile of the armature static torque (due to positive and negative MMF respectively) versus rotor angle did not have coincident zero torque regions. Similarly, the instantaneous torque waveforms with and without armature current were investigated on EXTPMFSM 1. Asymmetric airgap is introduced by modifying the rotor lamination profile. *The positive torque is taken to be counter-clockwise torque and vice versa.* For external rotor design, the static torque computation at each rotor position has to be carefully dealt with. It is because during the torque calculation using Maxwell's stress tensor method, the external rotor is rotating at the outer side of the integral line,

hence it was concluded to assign a negative sign on the calculated torque results. Details of how this conclusion was made are shown in Appendix C. It highlights the importance of investigating the equipotential lines and flux density distribution, in order to further verify the direction of positive torque for any design.



(a) Cogging torque of EXTPMFSM1

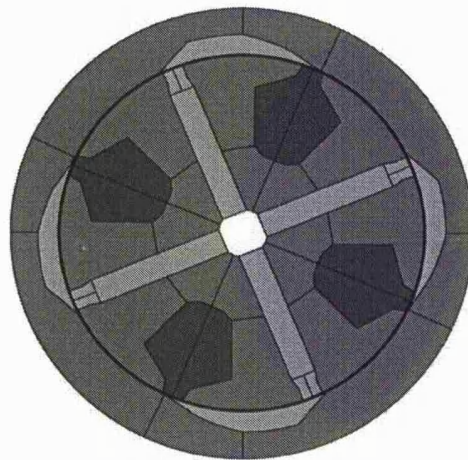


(b) Armature MMF = 400A-turns (blue line); -400A-turns (red line)

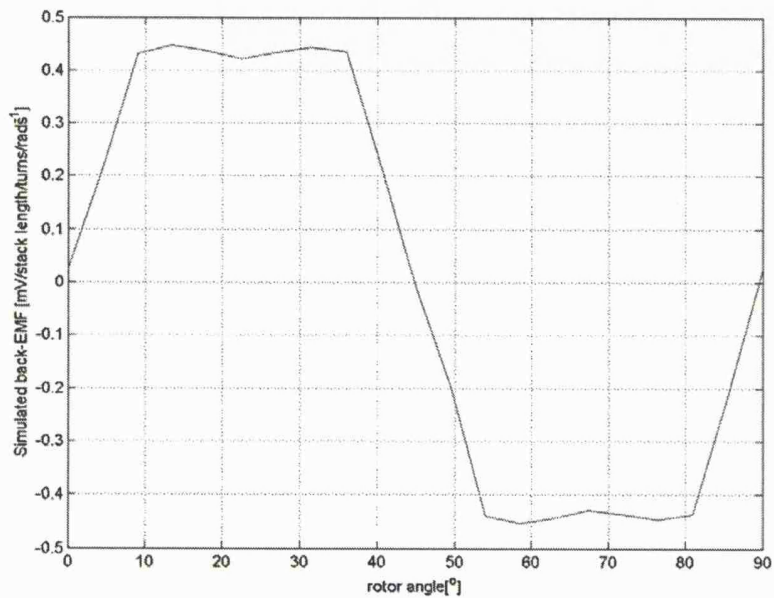
Figure 6.3: Simulated torque waveforms for EXTPMFSM 1

In Figure 6.3(a) and (b) show the cogging torque and the instantaneous torque when positive or negative DC armature current is applied for EXTPMFSM 1 respectively. In Figure 6.3(a), there is a rotor position at 43° where the rotor rests when no armature current is applied. At this rotor position in Figure 6.3(b), the instantaneous is near zero. This indicates that there is a chance EXTPMFSM 1 will not start, even with armature current is applied if the rotor rests at this rotor position.

Consequently, the rotor lamination profile of the proposed external rotor design, EXTPMFSM 1, had to be reconfigured. Figure 6.4(a) shows the modified final design of the external rotor design, EXTPMFSM 2.

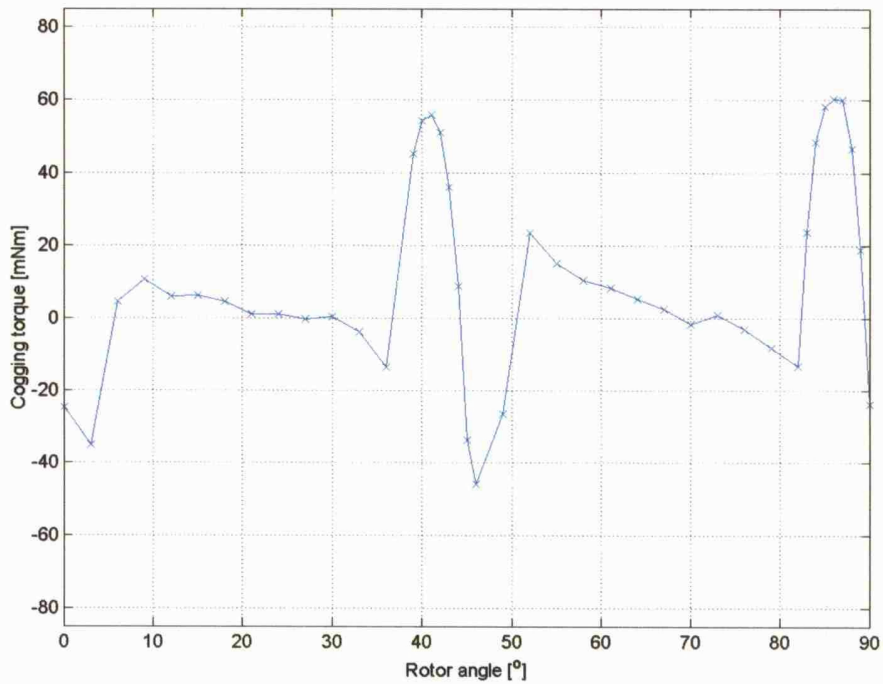


(a) EXTPMFSM 2 at rotor position of 0°

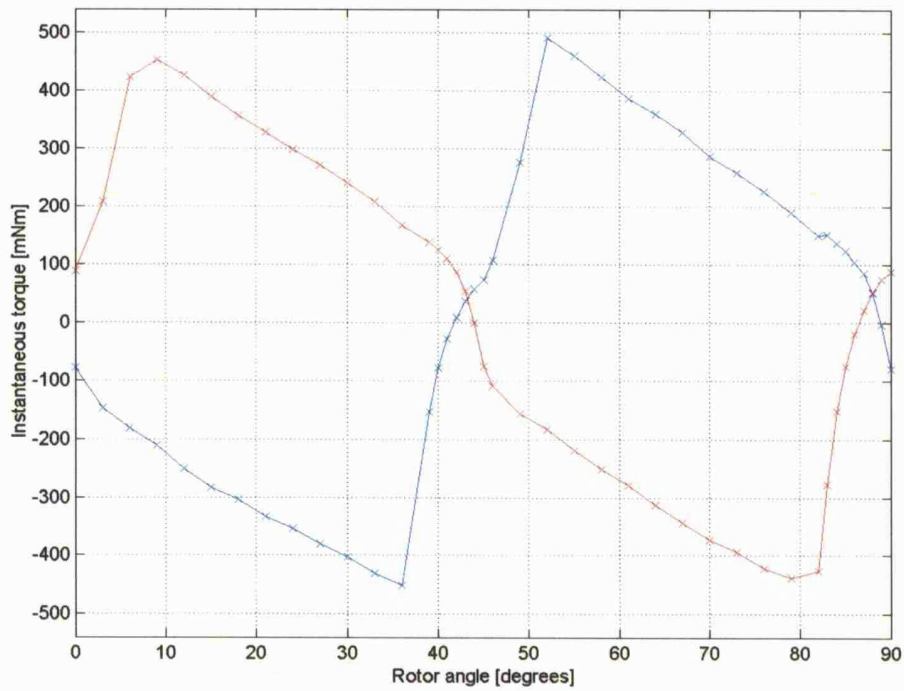


(b) Simulated back-EMF waveform

Figure 6.4: Modified EXTPMFSM 2



(a) Cogging torque for external rotor



(b) Instantaneous torque for external rotor.

Simulated at 400A-turns (Blue line) and -400A-turns (Red line)

Figure 6.5: Simulated instantaneous torque and back-EMF waveform for EXTPMFSM 2

Figure 6.5(a) and (b) show the cogging torque and the instantaneous torque when positive or negative DC armature current is applied respectively. Figure 6.5 (a) shows that the rotor rests at

rotor positions where cogging torque is zero. Figure 6.5 (b) shows that at the rotor positions where the rotor rests, a positive instantaneous torque exists regardless of the polarity of DC armature current applied, indicating that the rotor will definitely be able to move out of its resting positions. Hence, it is conclusive again that, the rotor will definitely be able to move out of this position. Moreover, Figure 6.4(b) shows that this final design lamination retains the desired trapezoidal back-EMF waveform as well. This machine lamination profile was then proposed for the external rotor design, and referred to as EXTPMFSM 2.

Table 6.1 gives a comparison of the predicted performance of EXTPMFSM 2 among the induction motor, 3-phase BLDC and INTPMFSM 2. It clearly shows that the external rotor design (EXTPMFSM 2) is capable to perform better than the induction motor and the BLDC at the varying speeds. Furthermore, as expected, EXTPMFSM 2 is simulated to be more efficient than INTPMFSM 2.

Table 6.1: Comparison of performance among IM, BLDC, INTPMFSM 2 and EXTPMFSM 2

	Average speed [rpm]	Average voltage applied [V]	Average input power [W]	Average output power [W]
EXTPMFSM 2 (Predicted)	708	38	1.57	1.19
	1352	76	10.09	8.26
	1731	119	20.59	17.34
	2168	240	69.82	34.07
INTPMFSM 2 (Measured)	715	54	7.20	1.22
	1339	76.62	24.63	8.03
	1735	132.6	62	17.46
3-phase Brushless DC (Measured)	708	240	9.00	1.19
	1352	240	16.6	8.26
	1731	240	24.6	17.34
Induction motor (Measured)	981	240	36.43	3.15
	1350	240	54.57	8.23
	1733	240	74.45	17.40
	2168	240	86.31	34.07

From the spreadsheet simulation, the suggested armature winding diameter to be used is 0.2mm and 402-turns for each bifilar strand in the external rotor PMFSM (EXTPMFSM 2), where each strand has 2 coils in series wound in the same direction. The winding configuration is exactly the same as for the internal rotor PMFSM as shown in Figure 5.10.

6.3 CAD design

The final CAD design and some brief explanation of certain aspects of the parts of the EXTPMFSM 2 are given, with the dimensioned drawings in Appendix E. Similar design constraints as briefed in section 5.5 are to be met. Table 6.2 below shows some of the main dimensions of EXTPMFSM 2 compared with the existing BLDC.

Table 6.2: Main dimensions for EXTPMFSM 2
All dimensions subject to ± 0.01 mm, unless stated otherwise.

	External rotor 3-phase Brushless DC BLDC	External rotor PMFSM EXTPMFSM 2
Stator outer diameter [mm]	75.98	66.9
Stator inner diameter [mm]	24.2	Shaft diameter
Rotor outer diameter [mm]	92.3	85
Rotor inner diameter [mm]	76.75	67.5
Airgap [mm]	0.385	0.3
Stack length [mm]	25.5	26
Shaft diameter [mm]	8	8
Number of stator poles	6	8
Number of rotor poles	6	4
Volume of all magnets [mm ³]	54856.36	10952.5
Number of turns per strand of bifilar winding, N	Not known	402
Number of coils in series per strand of bifilar winding	Not known	2
Number of coils in parallel	Not known	1
Winding diameter [mm]	Not known	0.2
Winding packing factor	Not known	0.125

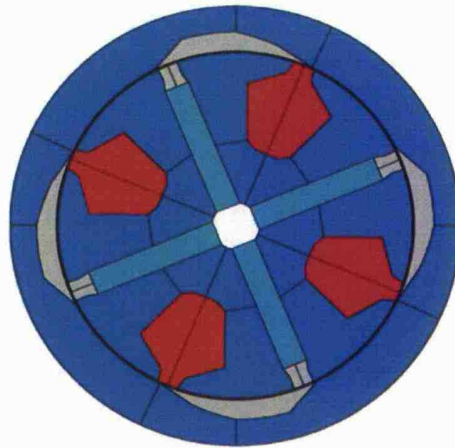


Figure 6.6: External rotor PMFSM, EXTPMFSM 2

In the CAD drawings, the sharp edges of the stator laminations shown in Figure 6.6 were rounded off with 0.1mm radius. This in practice could reduce the concentration of high flux density, which then reduces hysteresis loss.

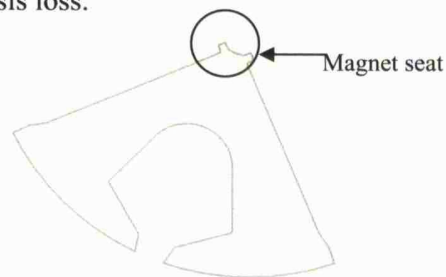


Figure 6.7: Stator lamination of EXTPMFSM 2

Extra magnet 'seats' were to be made for the stator lamination of EXTPMFSM 2 at its end nearest to the shaft, as shown in Figure 6.7 to prevent the magnets from touching the shaft.

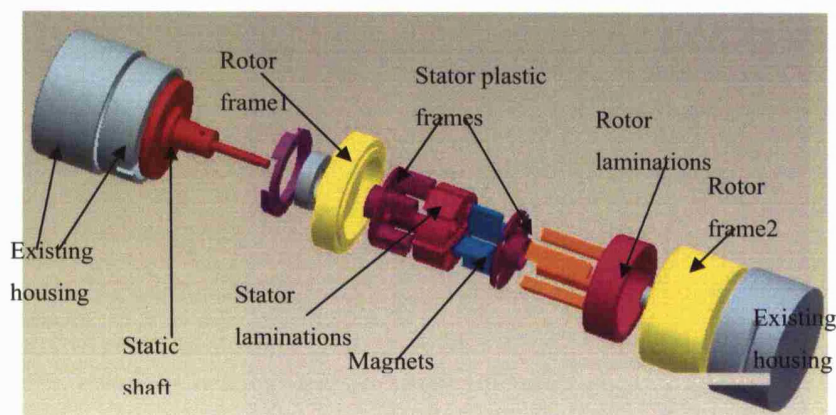


Figure 6.8: Exploded CAD drawing of EXTPMFSM 2

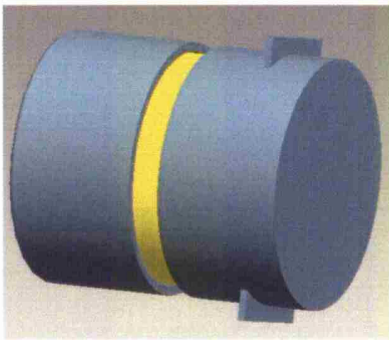


Figure 6.9: Assembled view

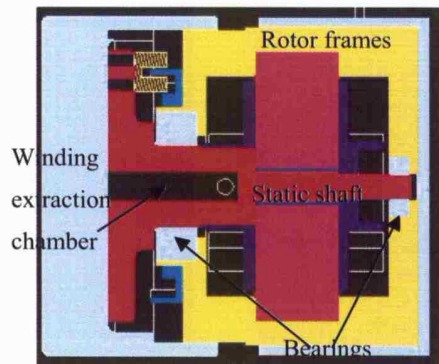


Figure 6.10: Assembled section view inside the EXTPMFSM 2

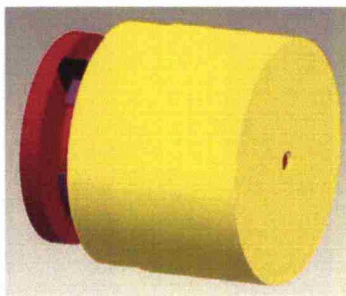


Figure 6.11: Assembled EXTPMFSM 2 without existing housings

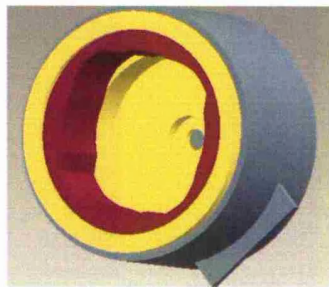


Figure 6.12: Assembled rotor and rotor frames with fan blade housing

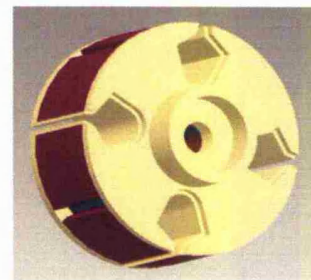


Figure 6.13: Assembled stator laminations, magnets and frames

For EXTPMFSM 2, the static shaft, as its name suggests, does not rotate. Its flanges are to locate the positions of the bearings and the position of the stator lamination assembly shown in Figure 6.13. The stator lamination assembly will be fastened tightly onto the threaded portion on the tip of the static shaft with a nut. Rotor frame2, in Figure 6.8, contains the external rotor laminations tightly fitted and glued in it. Both the rotor frames are then fastened together with screws. The winding extraction chamber, shown in Figure 6.10, allows the coil windings to be connected to the power converter outside the machine, hence additional holes were to be made on the existing housings.

Photos of the final prototype assembly are shown in Appendix F. Some problems that occurred during and after the assembly of the prototype were such as problems inserting the windings in the external rotor motor and ‘clicking’ noise while hand-spinning EXTPMFSM 2.

While assembling EXTPMFSM 2, a few obstructions were encountered while inserting the coils windings into the static shaft and assembling the rotor onto the shaft. Initially, the 5mm hole, as shown in Figure 6.14, on the static shaft’s 23mm-diameter shoulder was made in right-angles to allow the windings inserted and taken out through the middle of the shaft, but these were not possible as the right-angled corner caught on to the winding and took off some insulation. Hence, the corners of the holes were modified to have 45° slopes, and the section encircled in Figure

6.14(a) was removed, which finally allowed the smooth insertion of the winding and extended the winding out through the middle of the shaft as shown in Figure 6.14(b).

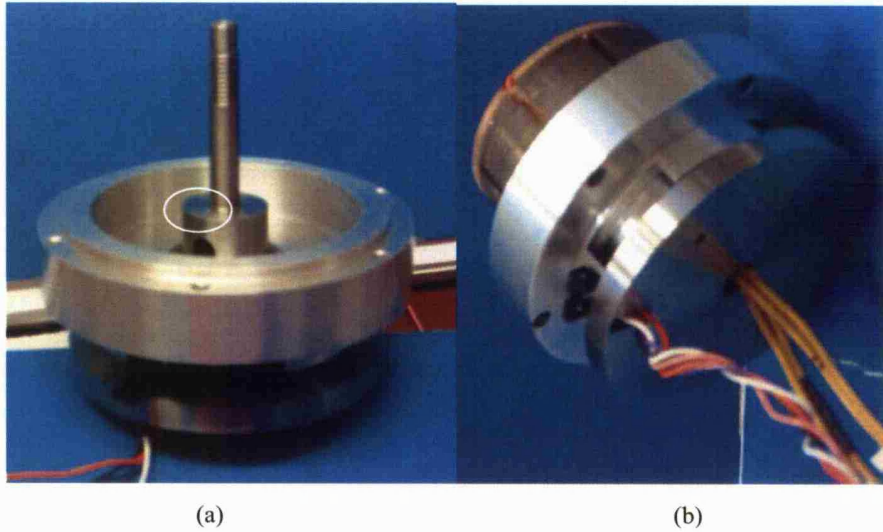


Figure 6.14: Static shaft for EXTPMFSM 2 design without modification

Next, after assembling the rotor lamination and its frame onto the shaft, a ‘clicking’ noise was heard while rotating the rotor part by hand. It was found that some of the stator laminations were moving radially to close the airgap between the stator and rotor when the rotor lamination was at a position shorting the magnet paths as shown in Figure 6.15. Using a metal screw driver and moving it around the stator to short the magnet flux path, was enough to generate force to feel or even observe stator laminations moving radially outwards.

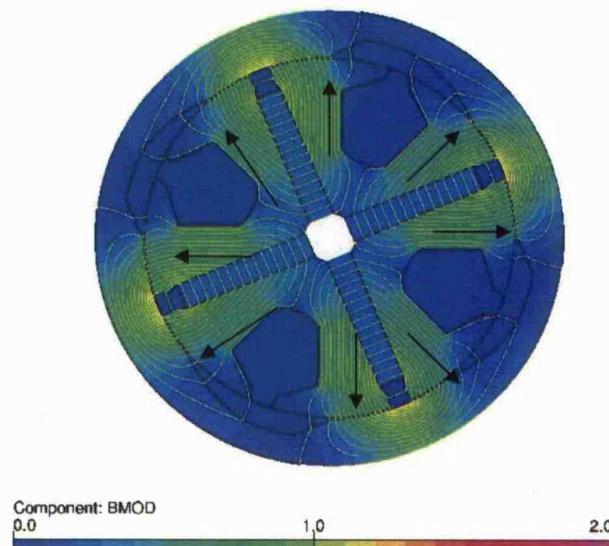


Figure 6.15: Rotor position when rotor shorts magnet flux paths
Arrows indicate likely radially movement. Arrow lengths have no indication of magnitude.

BMOD: Flux density modulus

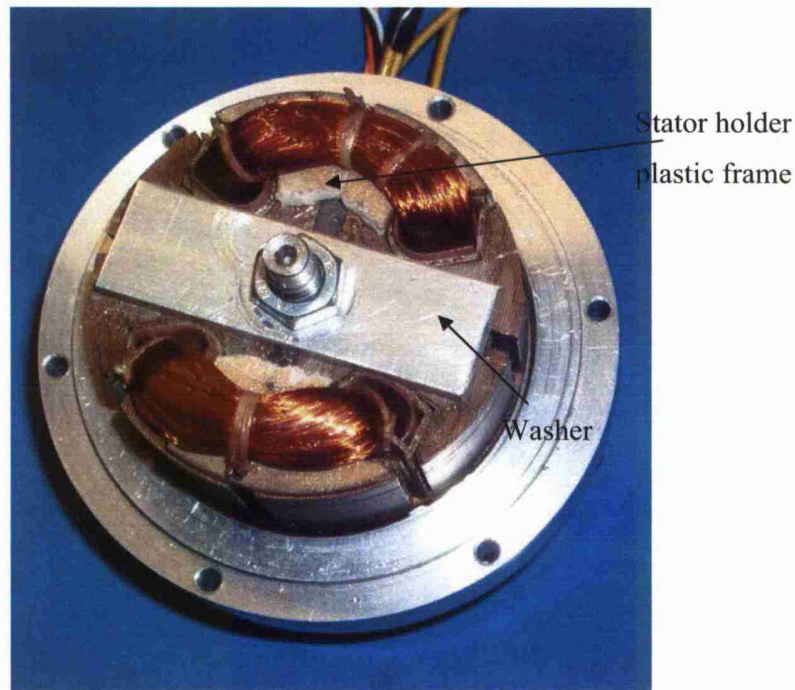
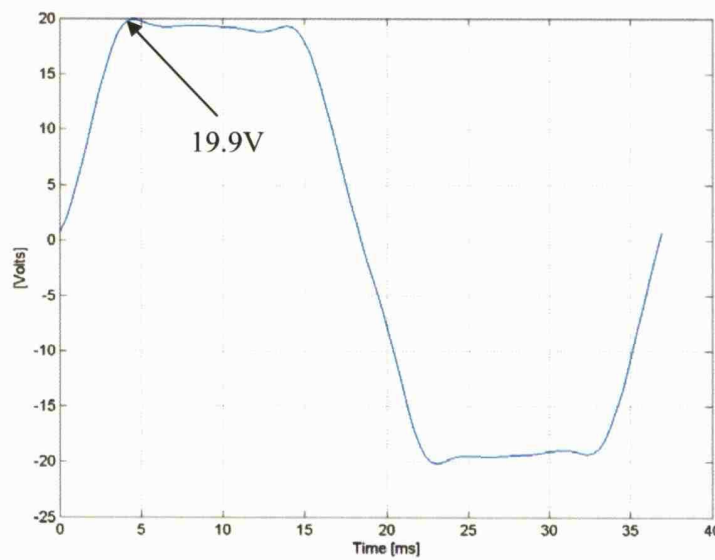


Figure 6.16: Partly assembled external rotor PMFSM with additional washer and nut

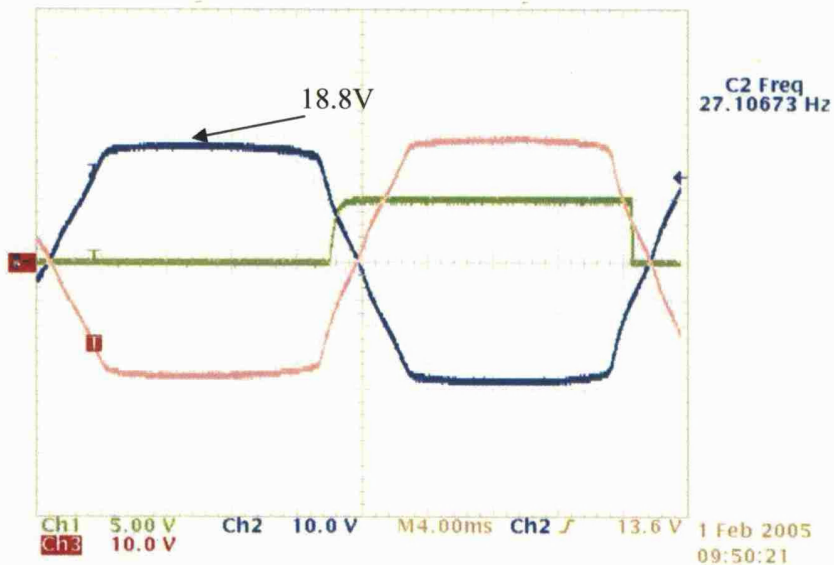
This meant that the plastic frames were not strong enough as thought it could be to hold the stator laminations from displacing radially outwards. It was then suggested to clamp the laminations axially between the static shaft flange and a washer of some sort that would be able to clamp onto a significant area of the stator lamination, tightening it with a nut as shown in Figure 6.16. Note that the static shaft flange and washer are made from aluminium and are in contact with the laminations directly. Furthermore, before tightening the nut, the stator laminations were ensured to be kept at the correct diameter. The work here was done by hand and not with machinery. With this done, the clicking noise was eliminated while the rotor was spinning around the stator. However, with this achieved, the airgap was made to be 0.4mm as the outer diameter of the stator lamination is 66.7mm instead of 66.9mm.

6.4 Experimental tests on the external rotor PMFSM, EXTPMFSM 2

The same power converter drive as shown in Figure 5.21 that drives the internal rotor PMFSM is used to drive EXTPMFSM2. Both armature windings are combined to create bifilar windings, magnetically coupled to one another.



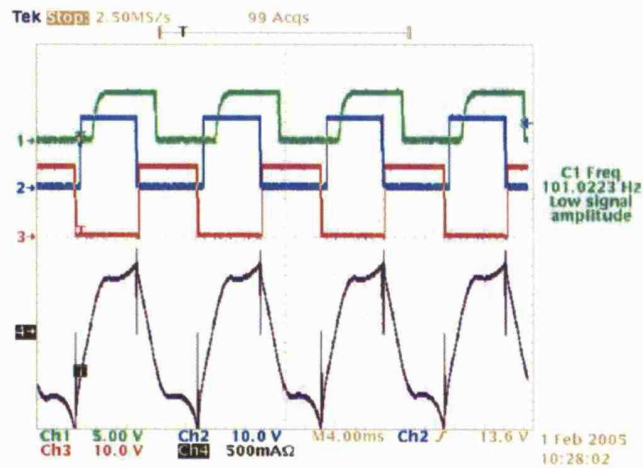
(a) Simulated back-EMF at 406rpm



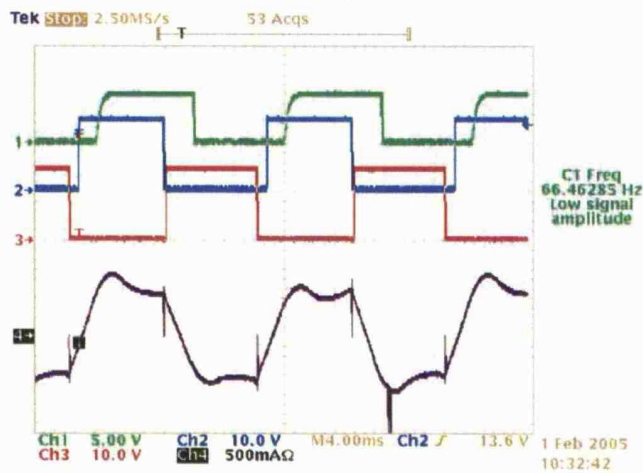
(b) Experimental back-EMF spinned at 406rpm

Figure 6.17: Simulated and experimental back-EMF waveform for EXTPMFSM 2

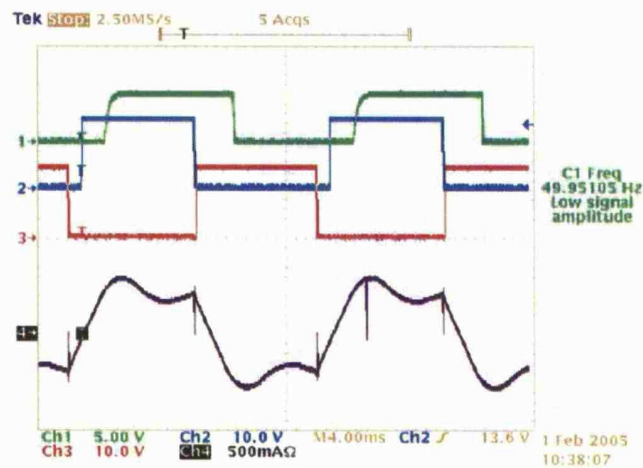
Figure 6.17(a) and (b) show the simulated and experimental back-EMF of EXTPMFSM 2, at 406rpm. Note that Figure 6.17(a) was simulated with 0.4mm airgap. They both show good similarity.



(a) Waveforms at 1500rpm, 131.8Vdc, Power input=70W



(b) Waveforms at 1000rpm, 72.3Vdc, Power input=33W



(c) Waveforms at 750rpm, 56.9Vdc, Power input=26.4W

Channel 1: Sensor; Channel 2: Switch 1; Channel 3: Switch 2; Channel 4: Armature current (0.5A/div)

Figure 6.18: Waveforms of EXTPMFSM 2 at 3 different speeds

	BLDC			External rotor PMFSM, EXTPMFSM 2 (Predicted)			External rotor PMFSM, EXTPMFSM 2 (Measured)		
Average speed [rpm]	1735	1352	708	1735	1352	708	1500	1000	750
Average voltage applied [V]	240	240	240	90	61	26	131.8	72.3	56.9
Average input power [W]	24.6	16.6	9	25.22	11.12	1.84	70	33	26.4
Average output power [W]	17.46	8.26	1.19	17.34	8.26	1.22	11.28	3.34	1.41
Sound power [dB]	60.7	54	43	No available simulation			59.4	57.1	45.9

Table 6.3: Comparison of experimental results between BLDC and EXTPMFSM 2

From Table 6.3, initial experimental results from EXTPMFSM 2 show that it is not as efficient as it was designed to be. At speeds of 1500rpm, 1000rpm, and 750rpm, the EXTPMFSM 2 was practically drawing almost 50% more power than the BLDC. The prediction of the EXTPMFSM 2 is not consistent with the measured result as shown in Table 6.3, which will be first addressed. Some investigation went into measuring the resistance of the windings per bifilar strand. It turned out that the predicted mean length of turn of 114mm in the spreadsheet was small. Making rough measurements on the actual motor, the mean length of turn should be about 145mm, which is then applied to the spreadsheet. Table 6.4 on the next page shows a set of new predicted results for EXTPMFSM 2 with the new mean length of turn value applied.

	BLDC			External rotor PMFSM, EXTPMFSM 2 (Predicted)			External rotor PMFSM, EXTPMFSM 2 (Measured)		
Average speed [rpm]	1735	1352	708	1500	1000	750	1500	1000	750
Average voltage applied [V]	240	240	240	131.8	72.3	56.9	131.8	72.3	56.9
Average input power [W]	24.6	16.6	9	69.43	27.75	20.36	70	33	26.4
Average output power [W]	17.46	8.26	1.19	11.28	3.34	1.41	11.28	3.34	1.41
Sound power [dB]	60.7	54	43	No available simulation			59.4	57.1	45.9

Table 6.4: Comparison of results between BLDC and EXTPMFSM 2 with modified predicted results

From Table 6.4, the predicted results are closer to the experimental results than what was predicted. This evidently suggests that, on the built EXTPMFSM 2 with 0.4mm airgap length,

copper loss is one of the major setbacks due to the increase in the mean length of turn. The mean length of turn was increased, as the length between armature winding slots were designed to be longer in order to have thicker stator teeth, in the aim to achieve better stiffness. In addition, the plastic frame, as shown in Figure 6.16, that holds the laminations also increased the height of the end-winding. Furthermore, iron losses and winding temperature rise could have contributed to the extra power consumption. EXTPMFSM 2 had a higher sound power at low speeds. This could indicate that the stator lamination holder material is not strong enough. A metallic and non-magnetic material, such as stainless steel, could be used instead to hold the stator lamination. Table 6.4 also points out that EXTPMFSM 2 can potentially be quieter than the 3-phase BLDC, because the sound power readings are almost similar.

	BLDC			INTPMFSM 2			EXTPMFSM 2		
Average speed [rpm]	1735	1352	708	1735	1339	715	1500	1000	750
Average voltage applied [V]	240	240	240	132.6	76.62	54	131.8	72.3	56.9
Average input power [W]	24.6	16.6	9	62	24.63	7.20	70	33	26.4
Average output power [W]	17.46	8.26	1.19	17.46	8.03	1.22	11.28	3.34	1.41
Sound power [dB]	60.7	54	43	69.2	62	53	59.4	57.1	45.9

Table 6.5: Summary of performance comparison between BLDC, INTPMFSM 2 and EXTPMFSM 2

Table 6.5 summarises the measured performance results of the BLDC, INTPMFSM 2 and EXTPMFSM 2. The results from INTPMFSM 2 and EXTPMFSM 2 were also compared with the performance of the existing induction motor use in the same fan application in Table 6.6.

	Induction motor (IM)			INTPMFSM 2			EXTPMFSM 2		
Average speed [rpm]	1733	1350	981	1735	1339	715	1500	1000	750
Average voltage applied [V]	240	240	240	132.6	76.62	54	131.8	72.3	56.9
Average input power [W]	74.45	54.57	36.43	62	24.63	7.20	70	33	26.4
Average output power [W]	17.40	8.23	3.15	17.46	8.03	1.22	11.28	3.34	1.41
Sound power [dB]	68.8	62.4	58	69.2	62	53	59.4	57.1	45.9

Table 6.6: Comparison of experimental results between IM, INTPMFSM 2 and EXTPMFSM 2

It will be obvious that INTPMFSM 2 draws far less input power than the induction motor at low speed, as shown in Table 6.6, since INTPMFSM 2 draws less input power than the existing BLDC as well. At higher speeds, even though INTPMFSM 2 draws more input power than the

BLDC, INTPMFSM 2 is still drawing less input power than the induction motor for the same application. EXTPMFSM 2, however, consumes more input power than the BLDC at all speeds investigated, but consumes less input power than the induction motor. In terms of cost, both INTPMFSM 2 and EXTPMFSM 2 use only 2 switches in its power converter drive as shown in Figure 5.21, reducing costs of the package compared with the 6 switch BLDC drive. Therefore, from the commercial aspect point of view, INTPMFSM 2 and EXTPMFSM 2 will be more favourable than the more expensive 3-phase BLDC drive. EXTPMFSM 2 however has another advantage, where its construction is able to potentially reduce vibration and acoustic noise as shown in Table 6.5 and Table 6.6, due to its noise level as low as the existing BLDC, and being quieter than the IM and INTPMFSM 2. Commercial 9-inch ventilation fans with variable speeds tend to be used in large, public-used halls. Some applications has the lowest speed as the default speed for ventilating purposes when buildings are not in use, in order to save energy. With this application in mind, both the INTPMFSM 2 and EXTPMFSM 2 can be more superior to the BLDC in terms of costs, and more superior to the induction motor in terms of consumed input power, and additionally EXTPMFSM 2 can reduce vibration and acoustic noise.

6.5 Summary for the internal rotor and external rotor PMFSM

In conclusion, two new permanent magnet flux switching motors of an internal rotor version and an external rotor version respectively have been designed, manufactured, assembled and tested. The ability to self-start in the desired direction has been successfully implemented too.

It has been shown that the internal rotor PMFSM (INTPMFSM 2), with its present experimental results shown, has compared favourably with the 3-phase BLDC and induction motor for ventilation fans. At low speeds of approximately 700rpm, it consumes 29% less input power than the more expensive BLDC. At higher speeds above 1000rpm, INTPMFSM 2 was between the efficiency of the BLDC and induction motor. Further modification to the design of the magnetic circuit and the control of the armature excitation can improve its efficiency.

On the external rotor PMFSM (EXTPMFSM 2), the present experimental results show that it was also between the efficiency of the BLDC and induction motor. Its high input power at low speed of approximately 700rpm was basically due to high coil winding mean length of turn, which resulted in high copper loss, decreasing the efficiency of EXTPMFSM 2. Furthermore, iron loss, which is proportional to motor speed, and the rising of armature winding temperature could have also contributed in the increase of power consumption on both the machines.

However, it is worth pointing out that EXTPMFSM 2 is quieter than INTPMFSM 2, and almost as quiet as the existing BLDC. This evidently suggests that the assembling and construction

of EXTPMFSM 2 can potentially reduce vibration and acoustic noise. A stronger material should be used to hold the stator lamination of EXTPMFSM 2 in order to make it run quieter.

Another crucial point to note is that, both the PMFSMs offer a very low cost electronic controller with only one third of the power switches of the BLDC. With further design improvements, the permanent magnet flux switching motors will provide a low cost, low noise alternative to the BLDC in energy efficient applications.

Chapter 7

CONCLUSION AND FUTURE WORKS

7.1 Conclusion

The thesis has presented the work on investigating the vibration and noise of a classical brushless DC motor (BLDC) and the flux switching motor (FSM), and the design of two 8/4 permanent magnet flux switching motors (PMFSM) as alternatives to the BLDC for a similar fan application. Chapter 2 presented the investigation on an external rotor version BLDC to show the effect of the 3-stage commutation method to reduce vibration during the static test, as shown in Figure 2.11 and Figure 2.12. The main reason the 3-stage commutation method was not effective while the motor was running, was because the dominant noise and vibration were of aerodynamic origin, namely the fan blade passing frequency and its harmonics, as shown in Figure 2.16. Moreover, dominant vibration source could also be due to the vibration of the permanent magnet external rotor, instead of the inner stator structure, since the external rotor structure is more flexible than the stator, and the permanent magnet flux was stronger than the flux produced by the windings.

Static vibration test and dynamic test were then performed on a round-shaped and a polygon-shaped Flux Switching Motor (FSM) of internal rotor configurations, to determine their mechanical resonant frequencies, where results are shown in Table 3.1 in Chapter 3. Furthermore, from the acoustic noise investigation, the noise source of the round-shaped FSM was traced to the motor's housing, which could be induced by the vibration of the motor lamination. On the polygon-shaped FSM, a high-pitch whistling noise was the dominant noise component, and it is believed to be of aerodynamic origin, since the voltage pulse elimination did not significantly reduced the whistling noise subjectively. This was because most components of the siren tone coincided with the motor-speed-dependent harmonics as shown in Figure 3.26. In addition to that, this chapter showed the possibility of determining the vibration mode shape of the flux switching motor experimentally.

Mechanical finite element analysis was then performed to predict the mechanical resonant frequencies of the round-shaped and polygon-shaped FSMs presented in Chapter 3. As shown in Table 4.1, the predicted mechanical resonant frequencies coincided fairly well with the measured results. Furthermore, algebraic frequency equations derived from past literatures were used to predict the resonant frequencies of round-shaped and polygon-shaped FSM stator laminations. From three algebraic equations, it was concluded that equation (4.13) that considered the stator

lamination as a thick circular ring would be more favourable to be used to predict the mechanical resonant frequency of round-shaped stators as shown in Table 4.4 showing the possibility of predicting the mechanical resonant frequencies of a motor during its electromagnetic design stage. However, equation (4.13) was not suitable enough to predict the mechanical resonant frequency of the polygon-shaped FSM.

Finally, with the aim of introducing a high efficient, low noise and low cost motor compared to the BLDC and field-excited flux switching motor, Chapter 5 and 6 presented the design and construction of two 8/4 permanent-magnet flux switching motor (PMFSM) prototypes. Both the internal rotor version and external rotor version PMFSMs were designed and built, and have self-starting ability. The internal rotor PMFSM drew the least input power at low speeds of approximately 700rpm, 29% less than the existing BLDC at the same speed. However, both the internal rotor and external rotor PMFSM, have efficiencies between the BLDC and induction motor at higher speeds above 1000rpm. Increase in copper loss, iron loss and winding temperature were blamed to have contributed the extra consumption of input power at these higher speeds. However, both PMFSMs will be more favourable in the consumer market than the BLDC due to the reduction of costs of the power electronic drive for the PMFSMs that perform as well as the BLDC. One more aspect worth pointing out is that the external rotor PMFSM is quieter than the internal rotor PMFSM, and almost as quiet as the existing BLDC. Evidently suggests that with more systematic assembling and construction of the external rotor PMFSM, it can potentially reduce vibration and acoustic noise.

7.2 Future works

Future development could still be done from the work presented in this thesis. Finding a better solution to hold the loose stator laminations of the PMFSM could reduce vibration and noise. Metallic and non-magnetic materials should be chosen to manufacture these lamination holders. More work can be done in predicting the iron loss and winding temperature effect which were neglected during the design stage of the permanent magnet flux switching motors. Better understanding of what and how the dominant source of vibration of motors of external rotor versions could be done too. Furthermore, similar vibration and noise tests done on complete stator laminations can be performed on the permanent flux switching motor with loose stator laminations, in order to find out if there are any significant differences in vibration and noise characteristics. Mechanical finite element modeling on the PMFSM would be interesting to explore due to its unique stator structure.

The mechanical finite element analysis done in Chapter 4 regarded the stator laminations as lump models. The additional effect of employing lower in-plane shear modulus, G_{xy} , in laminated objects, as pointed out in [18], could be applied in these analyses in order to obtain better approximation and more accurate results. Windings on the stator teeth could play a role in influencing the mechanical resonant frequency of the stator structure as well. Furthermore, modeling of supports on the motor lamination is still going to be another challenge to explore. Modeling supports as extra forces or weights can be explored.

Further studies could also be conducted in deriving simple algebraic frequency equations to predict the mechanical resonant frequencies of polygon-shaped stator laminations. Some studies have gone into predicting mechanical resonant frequencies of box structures using tedious matrix approaches and invoking the energy conservation principle [30, 31]. Having these simple algebraic frequency equations can be useful during electromagnetic design stages, where the designer can have some knowledge of how good the motor design would be in terms of mechanical reliability.

REFERENCES

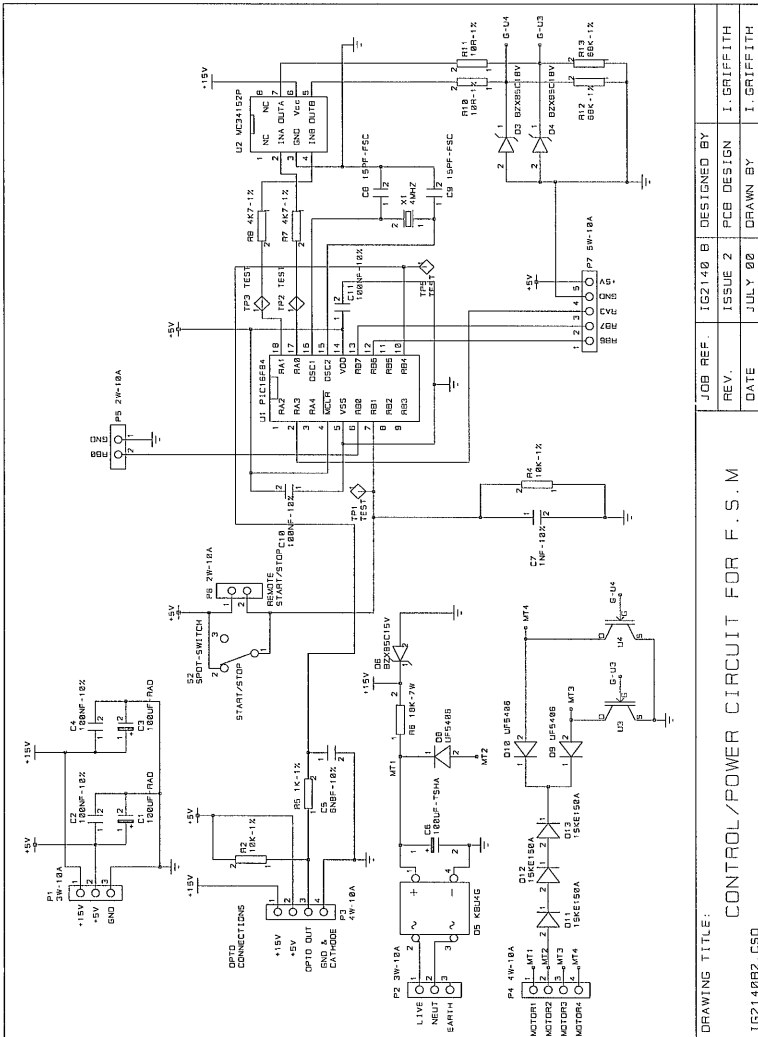
-
- 1) Charles Pollock, Mark Wallace, "The flux switching motor, a dc motor without magnets or brushes", Conference Record IAS Annual Meeting (IEEE Industry Applications Society), Vol. 3, 1999, pp 1980-1987
 - 2) [Http://www.uk.comsol.com](http://www.uk.comsol.com), COMSOL (UK) Ltd.
 - 3) <http://www.vectorfields.co.uk>, Vector Fields Ltd.
 - 4) T. J. E. Miller, "Switched Reluctance Motors and their Control", *Monographs in Electrical and Electronic Engineering 31*, Magna Physics Publishing, Oxford Science Publications, 1993, ISBN: 0-19-859387-2
 - 5) H. R. Bolton, Y. Shakweh, "Performance prediction of Laws's relay actuator", *IEEE Proceedings, Vol. 137, Part. B, No. 1, January 1999, pp 1-13*
 - 6) Derrick E. Cameron, Jeffrey H. Lang, Stephen D. Umans, "The origin and reduction of acoustic noise in doubly salient variable-reluctance motors", *IEEE Transactions on Industry Applications, Vol. 28, No. 6, November/December 1992, pp 1250-1255.*
 - 7) C. Pollock, C. Y. Wu, "Time domain analysis of vibration and acoustic noise in the switched reluctance drive", *IEE 6th International Conference on Electrical Machines and Drives, 1993, pp 558-563.*
 - 8) B. Ploner, F. Herz, "New design measures to reduce siren tones caused by centrifugal fans in rotating machines", *Brown Boveri Review, Vol. 56, 1969, pp 280-287.*
 - 9) D.A. Bies, C. H. Hansen, "Engineering Noise Control", Unwin Hyman Ltd., ISBN: 0-04-620021-5
 - 10) Mark Brackley, Charles Pollock, "Analysis and reduction of acoustic noise from a brushless d. c. drive", *IEEE Transactions on Industry Applications, Vol. 36, No. 3, 2000, pp 772-777*
 - 11) C. Y. Wu, C. Pollock, "Analysis and Reduction of Vibration and Acoustic Noise in the Switched Reluctance Drive", *IEEE Transactions on Industry Applications, Vol. 31, No. 1, Jan/Feb 1995, pp 91-98*
 - 12) C. Pollock, C. Y. Wu, "Acoustic noise cancellation techniques for Switched Reluctance Drives", *Proceedings of the IEEE IAS Society Annual Meeting, Orlando, USA, October 1996, pp 448-455*
 - 13) B. S. Rahman, D. K. Lieu, "The origin of permanent magnet induced vibration in electric machines", *Transactions of the ASME Journal of Vibration and Acoustics, Vol. 113, No. 4, October 1991, pp 476-481*

-
- 14) G. H. Jang, D. K. Lieu, "Vibration reduction in electric machine by magnet interlacing", *IEEE Transactions on Magnetics*, Vol. 28, No. 5, September 1992, pp 3024-3026
 - 15) G. H. Jang, D. K. Lieu, "The effect of magnet geometry on electric motor vibration", *IEEE Transactions on Magnetics*, Vol. 27, No. 6, November 1991, pp 5202-5204
 - 16) W. Cai, P. Pillay, Z. Tang, A. Omekanda, "Vibration measurements in the switched reluctance motor", *Conference Record of the 2001 IEEE Industry Applications Conference, 36th IAS Annual Meeting, Sept 30-Oct. 4, 2001, Chicago, Illinois, USA*, pp 11-17
 - 17) Zhangjun Tang, Pragsen Pillay, Avoki, M Omekanda, Chen Li, Cetin Cetinkaya, "Young's Modulus for laminated machines structures with particular reference to switched reluctance motor vibrations", *IEEE Transactions on Industry Applications*, Vol. 40, No. 3, May/June 2004, pp 748-753
 - 18) S. A. Long, Z. Q. Zhu, D. Howe, "Vibration behaviour of stators of switched reluctance motors", *IEE Proceedings, Electric Power Applications*, Vol. 148, No. 3, May 2001, pp 257-264
 - 19) R.S. Girgis, S. P. Verma, Dr.-Ing, "Method for accurate determination of resonant frequencies and vibration behaviour of stators of electrical machines", *IEE Proceedings*, Vol. 128, Pt. B, No. 1, January 1981, pp 1-11
 - 20) S. P. Verma, Dr. Ing, "Experimental verification of resonant frequencies and vibration behaviour of stators of electrical machines – Part 1: Models, experimental procedure and apparatus", *IEE Proceedings*, Vol. 128, Pt. B, No. 1, January 1981, pp 12-21.
 - 21) S. P. Verma, Dr. Ing, R. S. Girgis, "Experimental verification of resonant frequencies and vibration behaviour of stators of electrical machines – Part 2: Experimental investigations and results", *IEE Proceedings*, Vol. 128, Pt. B, No. 1, January 1981, pp 22-32.
 - 22) A. J. Ellison, S. J. Yang, "Natural frequencies of stators of small electric machines", *Proceedings of the IEE*, Vol. 118, No. 1, January 1971, pp 185-190.
 - 23) S. J. Yang, "Low-noise electrical motors", Clarendon Press, Oxford Science Publications, 1981, ISBN: 0-19-859332-5
 - 24) Roy S. Colby, Francois M. Mottier, Timothy J. E. Miller, "Vibration modes and acoustic noise in a four-phase switched reluctance motor", *IEEE Transactions on Industry Applications*, Vol. 32, No. 6, Nov/Dec 1996, pp 1357-1364
 - 25) Raymond J. Roark, "Formulas for stress and strain, 3rd Edition", 1954, McGraw-Hill Book Company Inc.
 - 26) J. Kirkhope, "Simple frequency expression for the in-plane vibration of thick circular rings", *Journal of the Acoustic Society of America*, Vol. 59, No. 1, January 1976, pp 86-88

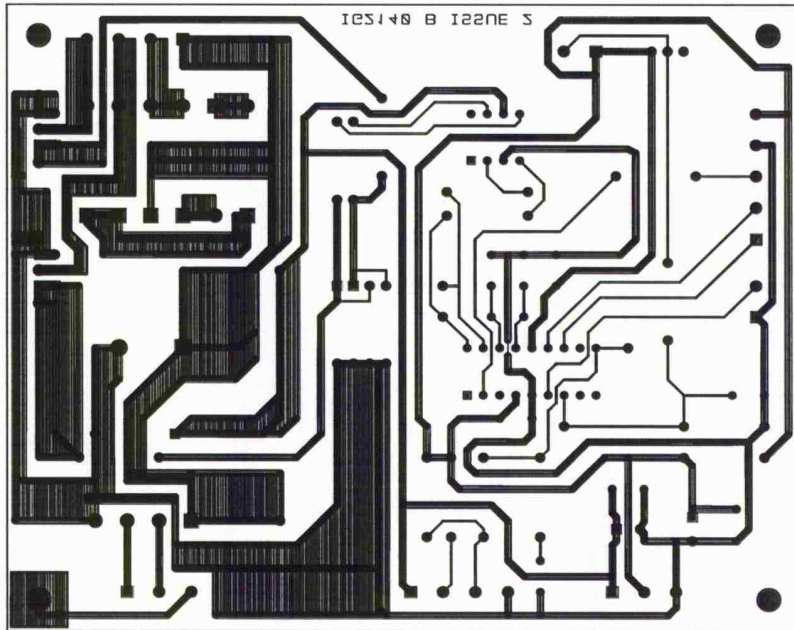
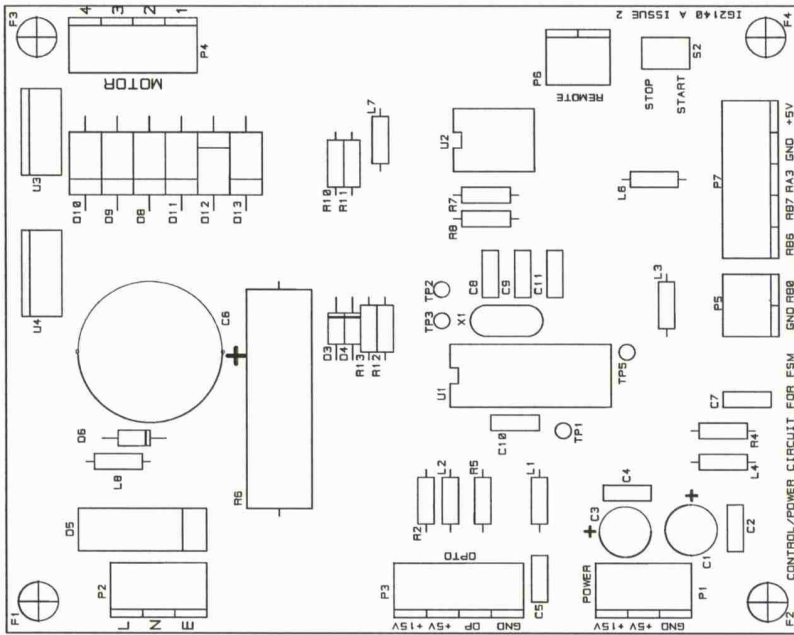
-
- 27) R. HOFFE, "The bending vibration of a circular ring", *Crelle J. Math*, 73, 158, (1871)
- 28) G. R. COWPER, "The shear coefficient in Timoshenko's Beam Theory", *Transactions of the ASME, Journal of Applied Mechanics, Series E, Vol. 83, June 1966*, pp 335-340
- 29) A. STASSIS, A. M. MICHAELIDES, "The design of low vibration doubly salient motors", *Electric Machines and Power Systems, Vol. 27, 1999*, pp 967-981
- 30) S. M. DICKINSON, G. B. WARBURTON, "Vibration of box-type structures", *Journal Mechanical Engineering Science, Vol. 9, No. 4, 1967*, pp 325-335
- 31) R. J. HOOKER, D. J. O'BRIEN, "Natural frequencies of box-type structures by a finite-element method", *Transactions of the ASME, Journal of Applied Mechanics, June 1974*, pp 363-365
- 32) T. KENJO, S. NAGAMORI, "Permanent magnet and brushless DC motors", Clarendon Press, Oxford Science Publications, 1985
- 33) TIMOTHY J. E. MILLER, "Brushless permanent-magnet motor drives", *Power Engineering Journal, January 1988*, pp 55-60
- 34) S. E. RAUCH, L. J. JOHNSON, "Design principles of flux-switch alternators", *Transactions of the American Institute of Electrical Engineers, Part 3, Power Apparatus and Systems, Vol. 74, 1955*, pp 1261-1268
- 35) XIAOGANG LUO, DINYU QIN, THOMAS A. LIPO, "A novel two phase doubly salient permanent magnet motor", *Conference Records of the 1996 IEEE Industry Applications Society 31st IAS Annual Meeting, San Diego, California, October 1996*, pp 808-815
- 36) F. LEONARDI, T. MATSUO, Y. LI, T. A. LIPO, P. MCCLEER, "Design considerations and test results for a doubly salient PM motor with flux control", *Conference Record of the 1996 IEEE Industry Applications Society 31st IAS Annual Meeting, San Diego, California, October 6-10, 1996, Vol. 1*, pp 458-463

Appendix A

Power Circuit Board



DRAWING TITLE:		CONTROL/POWER CIRCUIT FOR F. S. M	
JOB REF.	162140 B	DESIGNED BY	I. GRIFFITH
REV.	ISSUE 2	PCB DESIGN	I. GRIFFITH
DATE	JULY 08	DRAWN BY	I. GRIFFITH



Appendix B

A-weighting post-processing of noise in MATLAB

This appendix illustrates how the post-processing of the noise data was done in MATLAB, which is to apply A-weightings in the frequency domain.

The data values for the variables 'dBA' and 'freq' below are extracted from 'Engineering Noise Control' by D.A. Bies and C.H. Hansen, page 53, ISBN: 0-04-620021-5. These data are fitted with a polynomial of the 6th degree, having the frequency-axis in the logarithmic scale. With the raw noise data extracted into the variables 'spl' and 'f', where they represent the linear dB RMS sound power level [dB] and frequency [Hz] respectively, A-weightings were applied according to equation 1.2 at the frequencies stored in 'f'.

The code used in MATLAB to apply A-weighting is shown below. Variable 'm' is the number of data in 'f'.

```
dBA=[-70.4 -63.4 -56.7 -50.5 -44.7 -39.4 -34.6 -30.2 -26.2 -22.5 -19.1 -16.1 -13.4 -10.9 -8.6 -6.6 -  
4.2 -3.2 -1.9 -0.8 0.0 0.6 1 1.2 1.3 1.2 1 0.5 -0.1 -1.1 -2.5 -4.3 -6.6 -9.3];  
freq=[10 12.5 16 20 25 31.5 40 50 63 80 100 125 160 200 250 315 400 500 630 800 1000 1250  
1600 2000 2500 3150 4000 5000 6300 8000 10000 12500 16000 20000];  
dBAfit=polyfit(log10(freq),dBA,6);  
for k=2:m  
    dba(k)=spl(k)+polyval(dBAfit,log10(f(k))); % Implementing equation 1.2  
end
```

Appendix C

Determining the torque direction for external rotor PMFSM

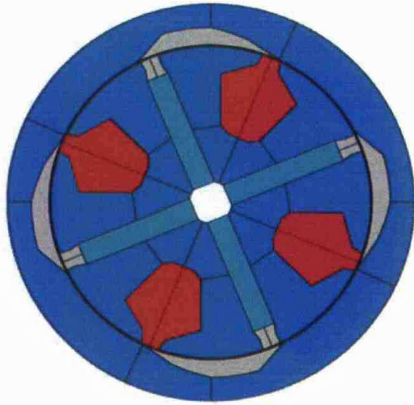


Figure C.1: External rotor topology

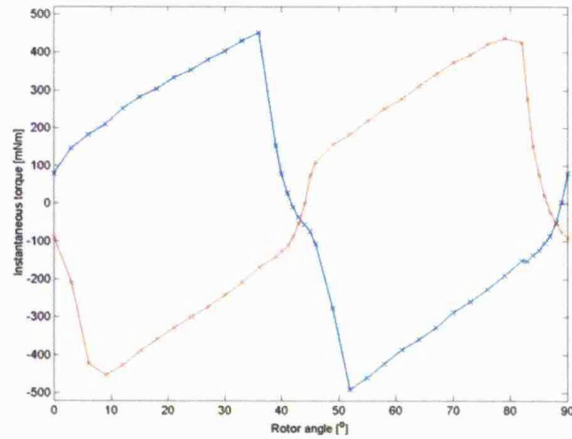


Figure C.2: Blue line is 400At, red line is -400At

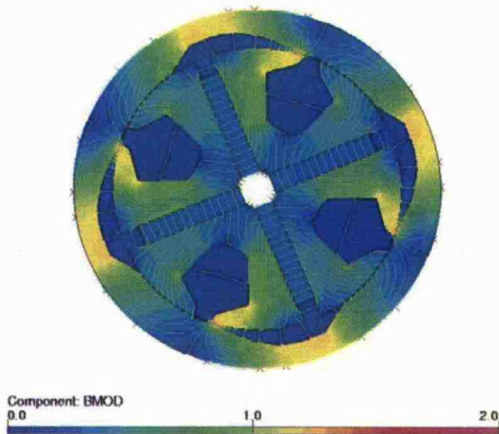


Figure C.3: -400At at 9°

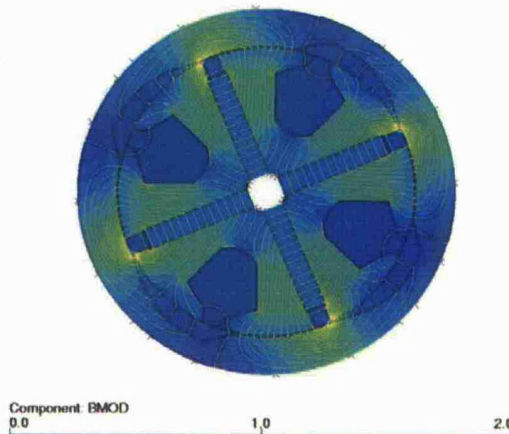


Figure C.4: 400At at 52°

It should be noted first that counter-clockwise torque is positive and vice versa.

For this particular rotor configuration, the intersection point of the instantaneous torque is negative as shown in Figure C.2. It was then put forward to investigate flux lines to verify the direction of torque produced. As observed in Figure C.3 and Figure C.4, both show that a positive torque is produced at the particular angle of interest.

This suggests that the computed instantaneous torque in the electromagnetic FE should be inverted in sign convention as the calculation of torque using the Maxwell stress equation is done when the external rotor was rotating on the outer side of the integral line in the middle of the airgap. Hence, after inversion, the result of Figure C.2 should be as shown in Figure C.5.

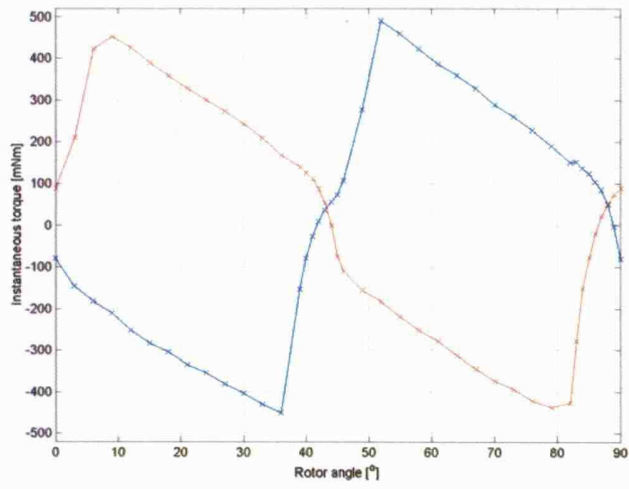


Figure C.5: Correct instantaneous torque waveform for external rotor design

Appendix D

Ferrite magnet BH curves

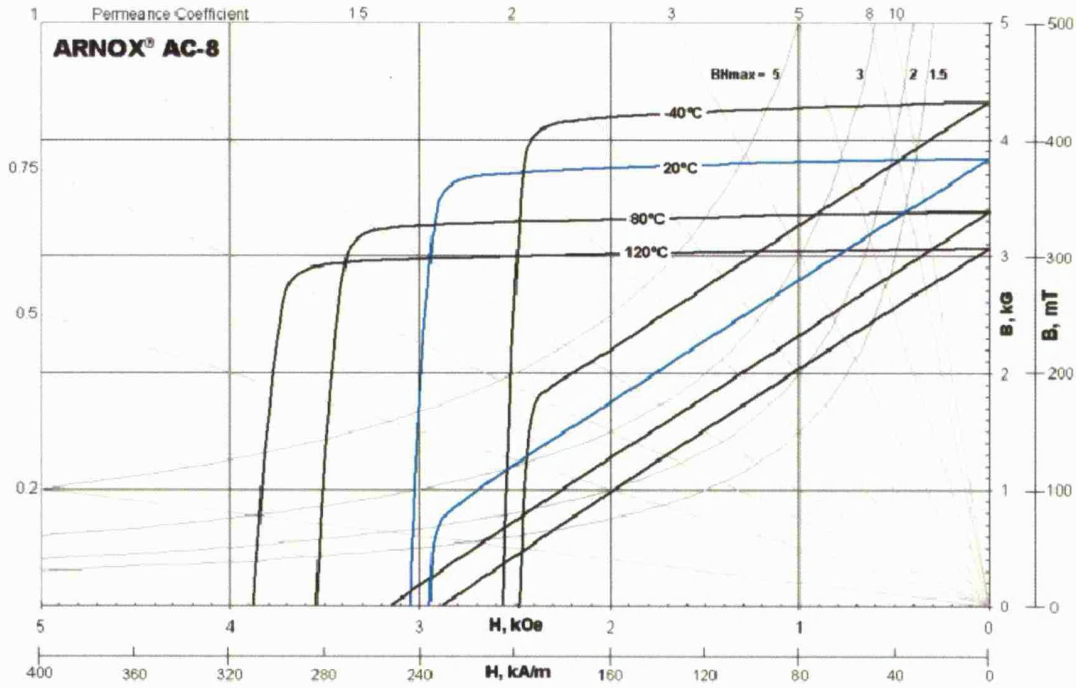


Figure D.1: BH Curves for ARNOX-AC8 permanent magnets

Magnetic and material characteristics, typical values 20°C									
Normal Peak Energy Product, BHmax		Residual Induction, Br		Coercive Force, Hc		Intrinsic Coercive Force, Hci		Density	
MGOe	kJ/m ³	G	mT	Oe	kA/m	Oe	kA/m	Lbs/cu.in.	g/cc
3.5	27.9	3850	385	2950	235	3050	243	0.177	4.9

Table D.1: Courtesy of Arnold Magnetics Limited

Appendix E

New Permanent-magnet Flux Switching Motor CAD drawings

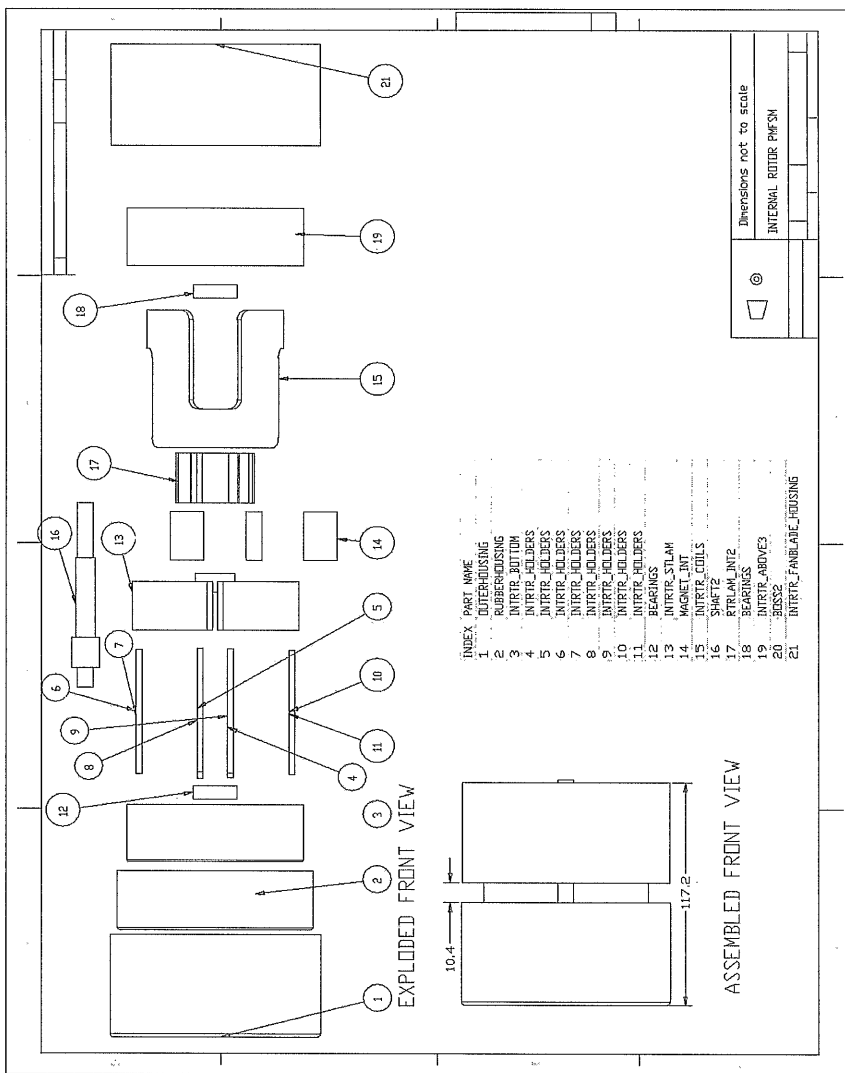
In this appendix, CAD drawings are being present for the design of the new permanent magnet flux switching motor (PMFSM), namely INTPMFSM 2 and EXTPMFSM 2. A list of the names of the parts of the internal rotor PMFSM and the external rotor PMFSM respectively are given in Table E.1.

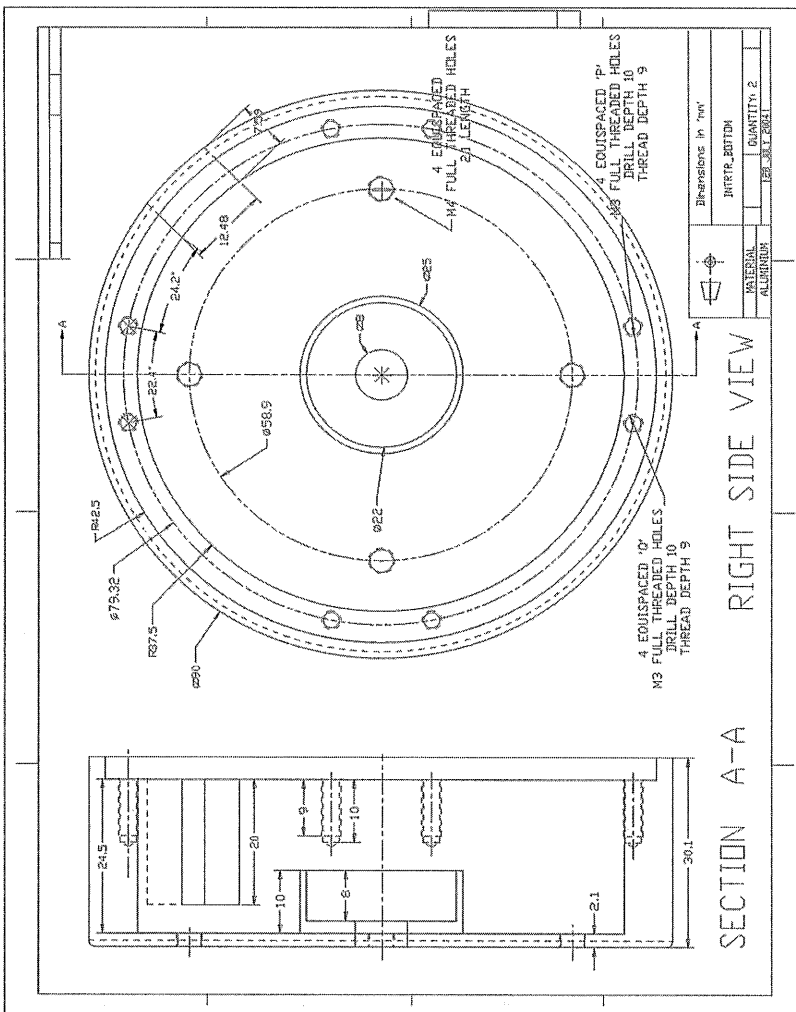
Internal rotor PMFSM part names	External rotor PMFSM part names
INTRTR_ABOVE3	EXTRTR_STFRAME
INTRTR_BOTTOM	EXTRTR_STFRAME2
INTRTR_SENSORINTERRUPTOR	EXTRTR_SENSORINTERRUPTER
INTRTR_STLAM	EXTRTR_STATOR
RTRLAM_INT	EXTRTR_ROTOR
SHAFT2	SHAFT
MAGNET_INT	EXTRTR_MAGNETS
INTRTR_HOLDERS	

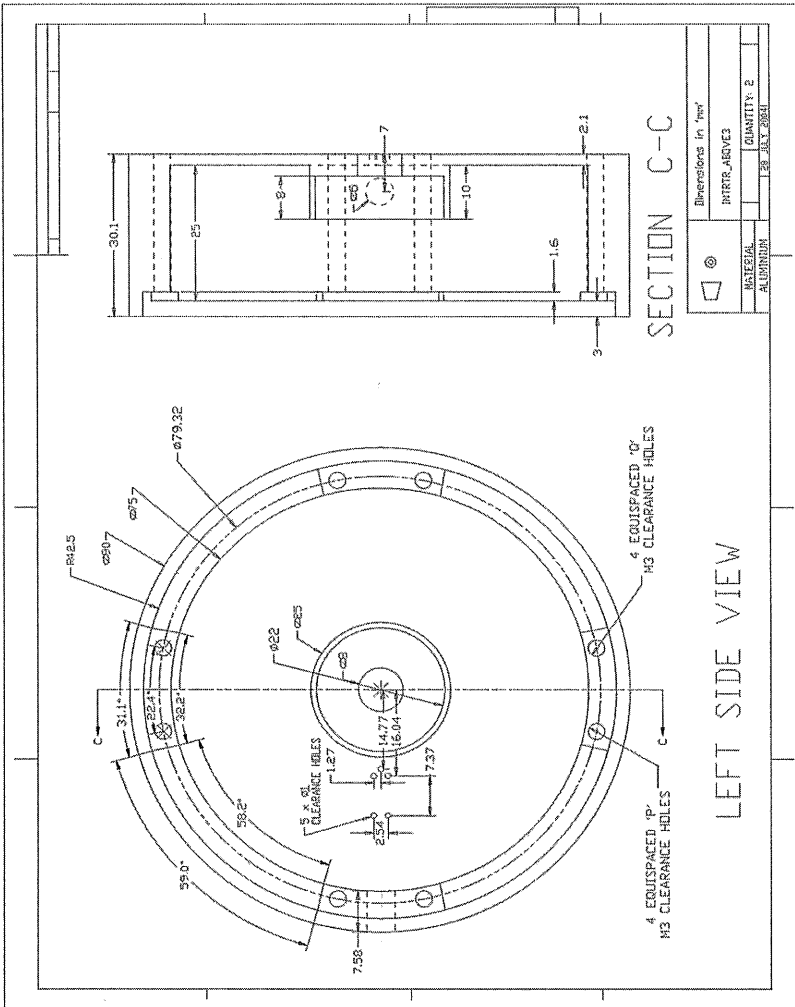
Table E.1: Part names in CAD drawings for INTPMFSM 2 and EXTPMFSM 2

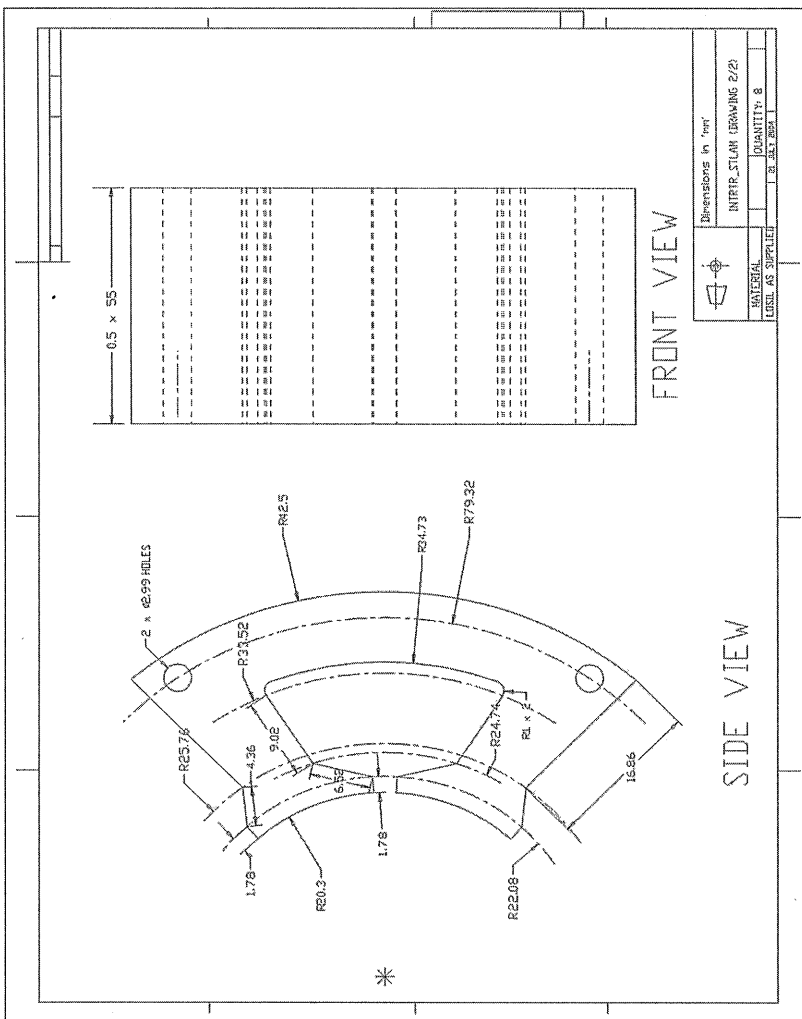
Please note that, one wave/crinkle washer is installed in each motor.

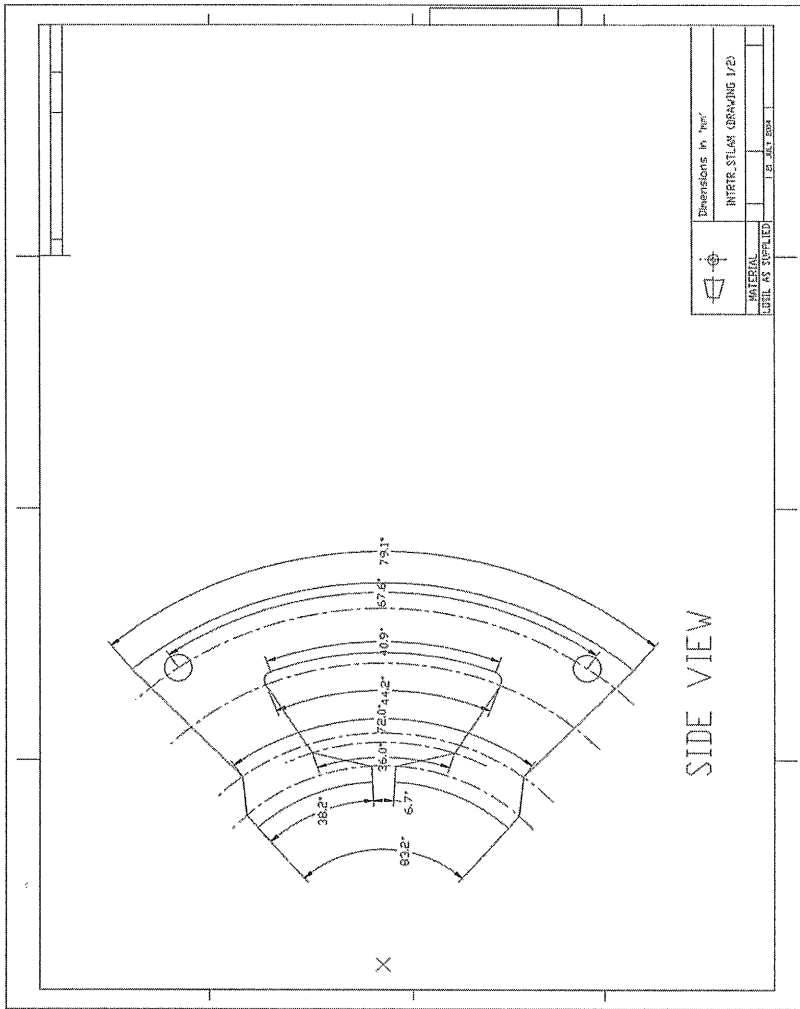
The permanent magnets were supplied by Arnoldmagnetic Ltd. The parts named EXTRTR_STFRAME and EXTRTR_STFRAME2 were made by IMI Rapid Prototyping Ltd. Steel laminations were manufactured by Di-Sparks Ltd. The rest of the assembly parts were made in the Engineering Department workshop.

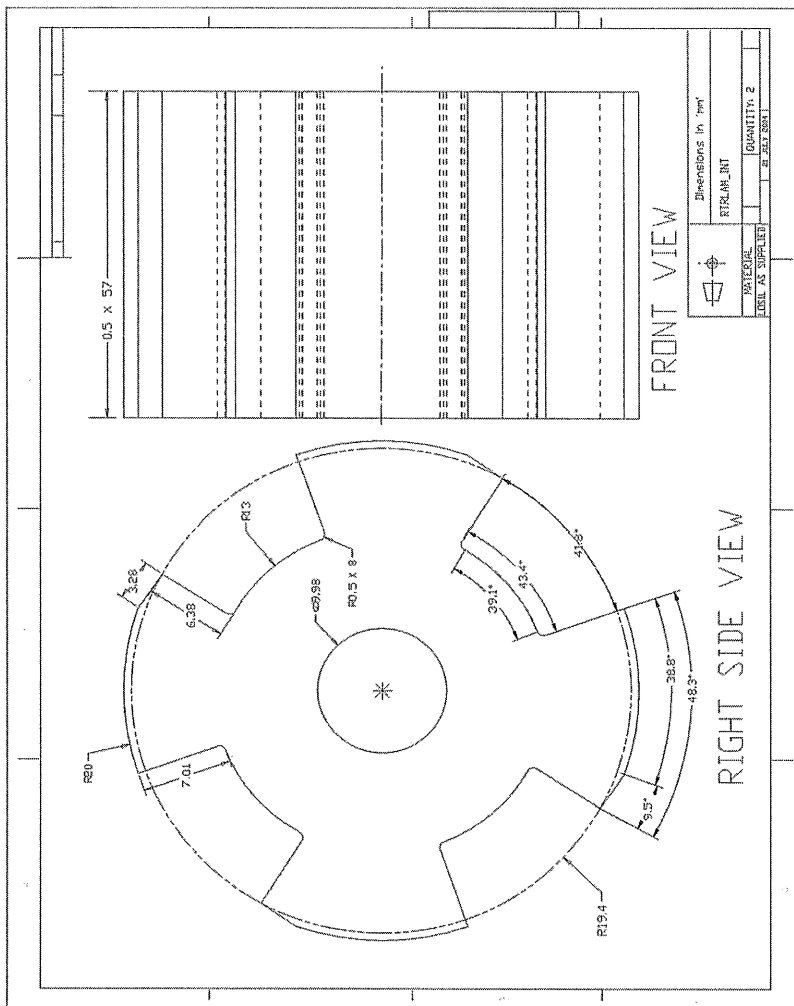


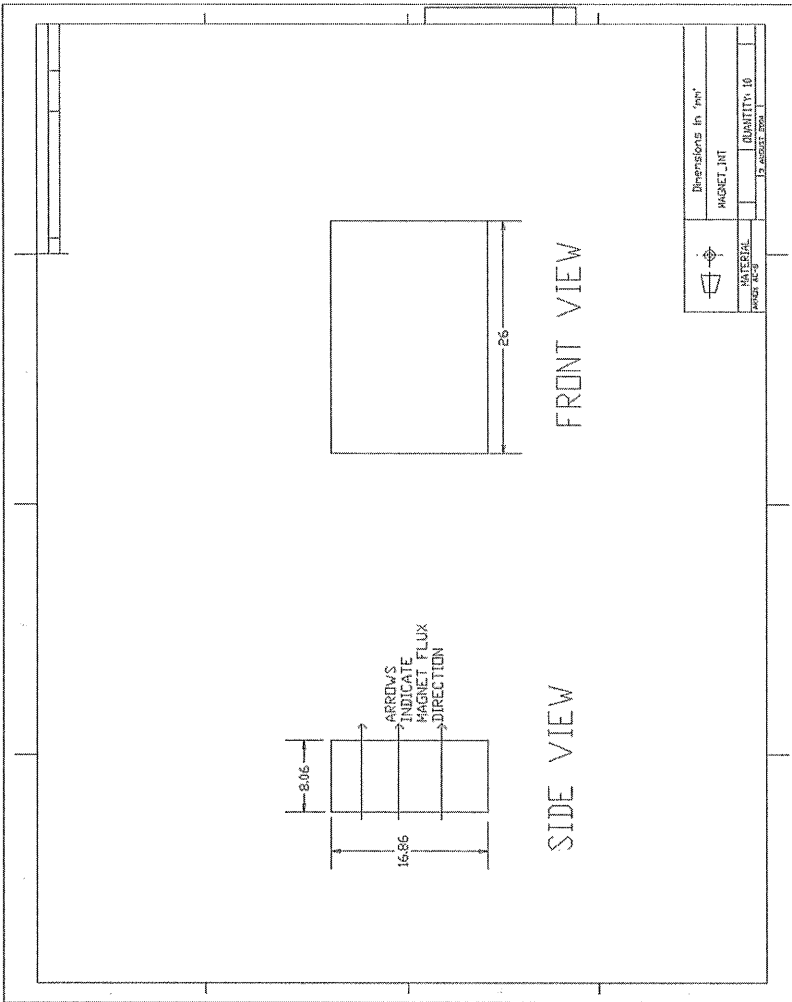


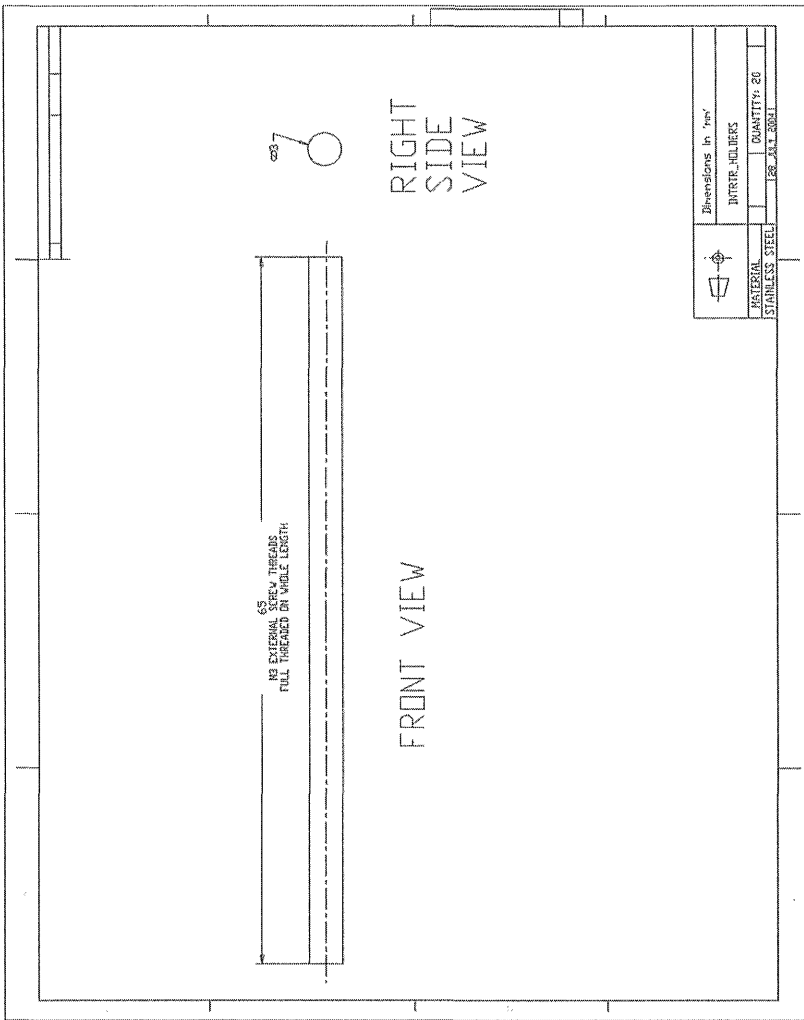


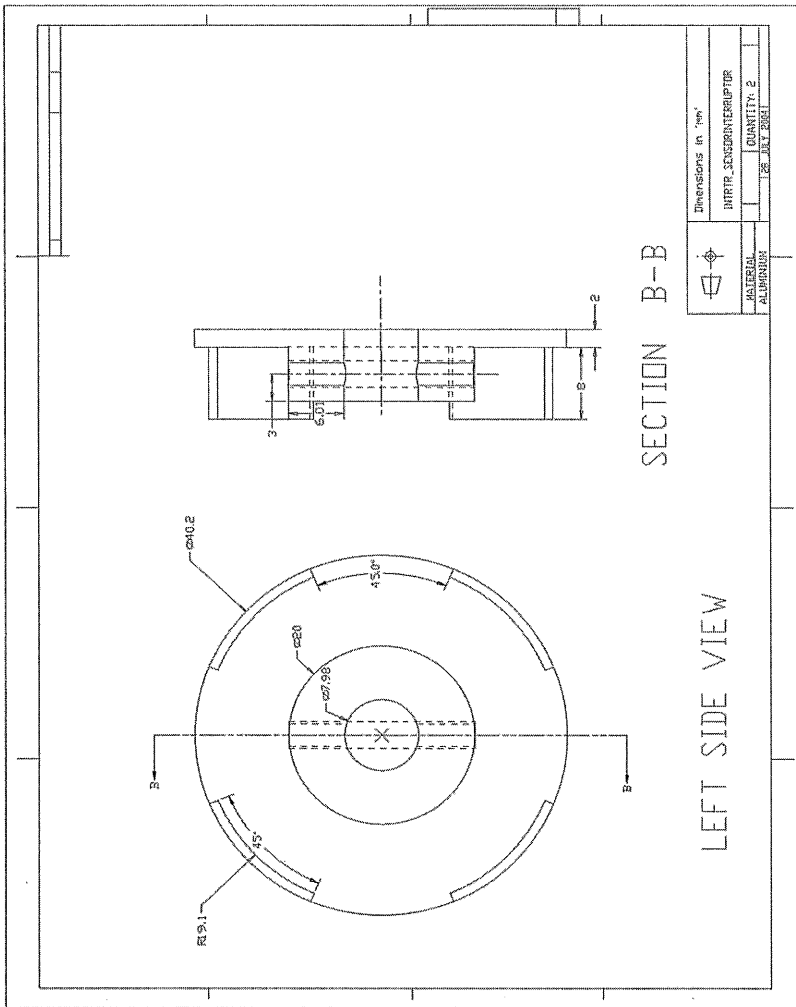


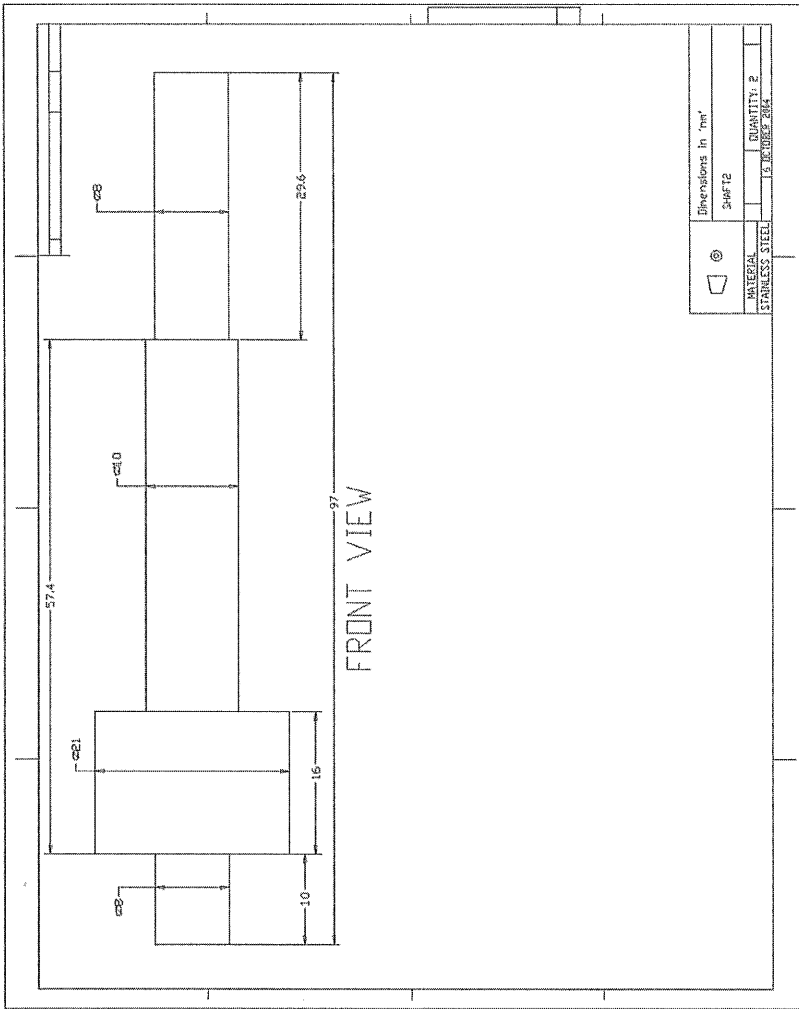




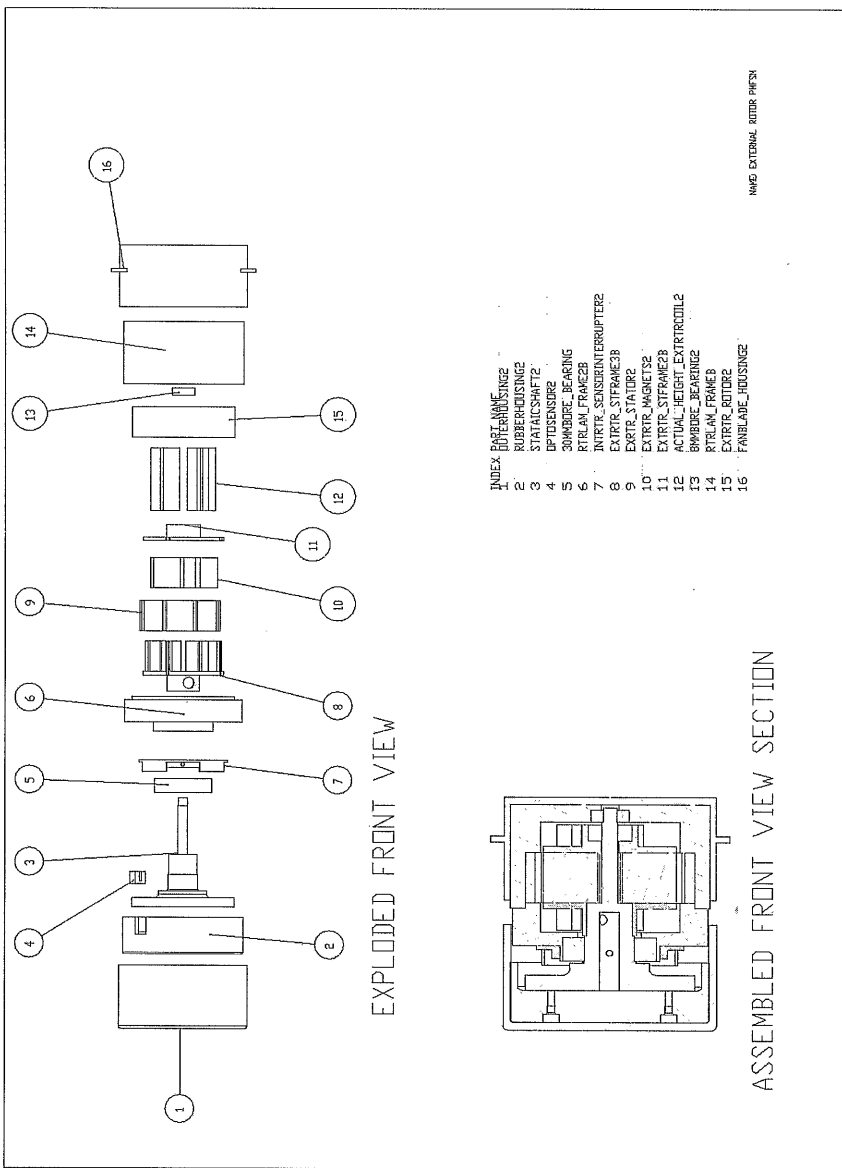


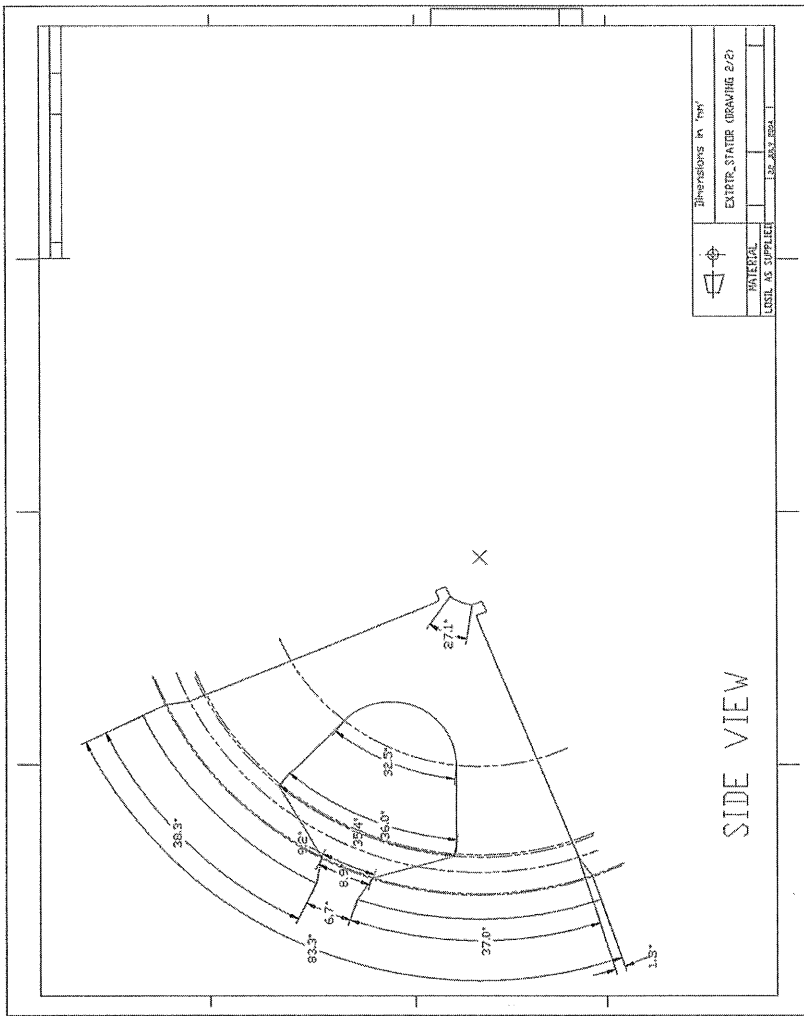


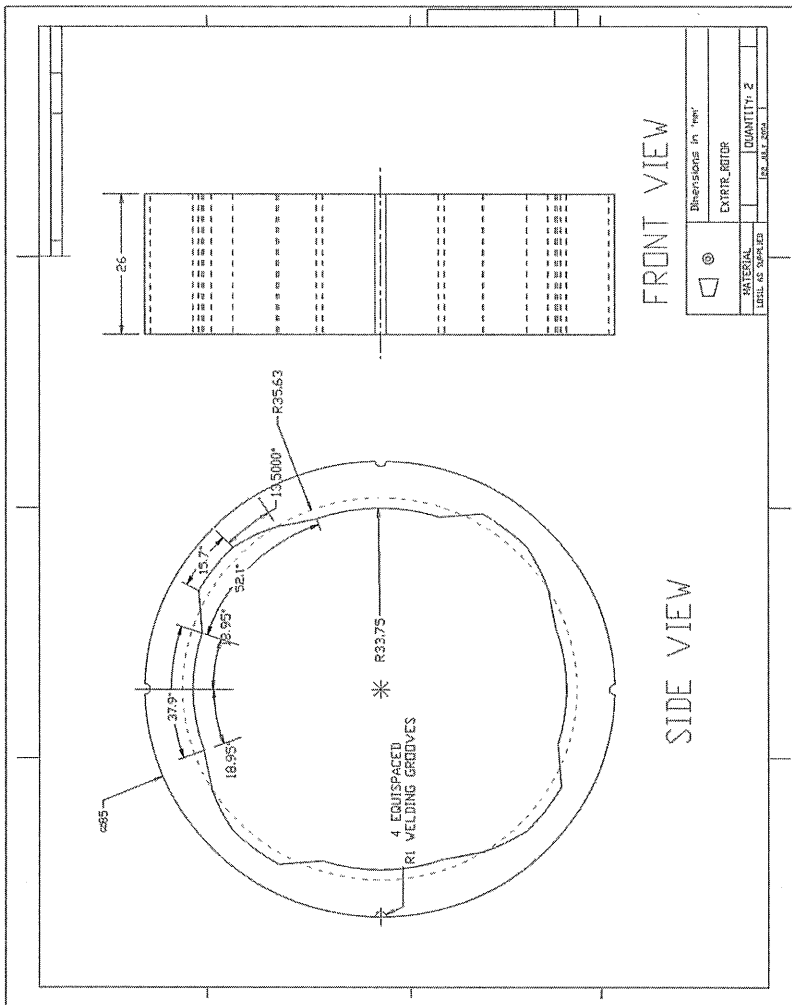


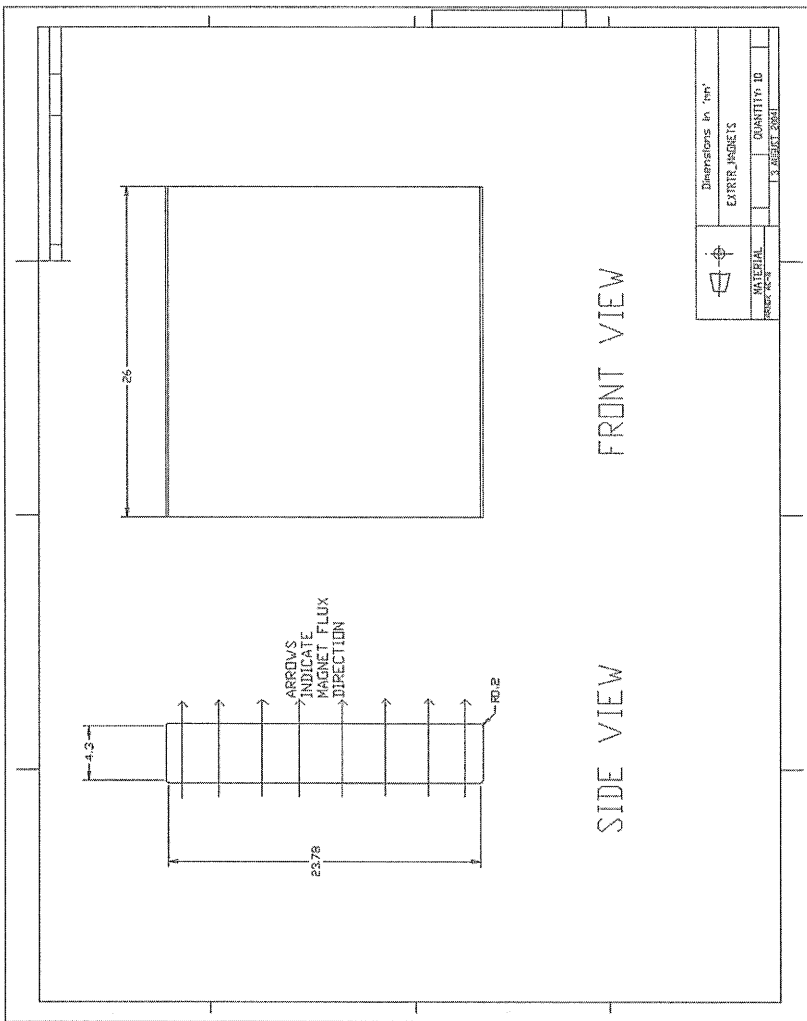


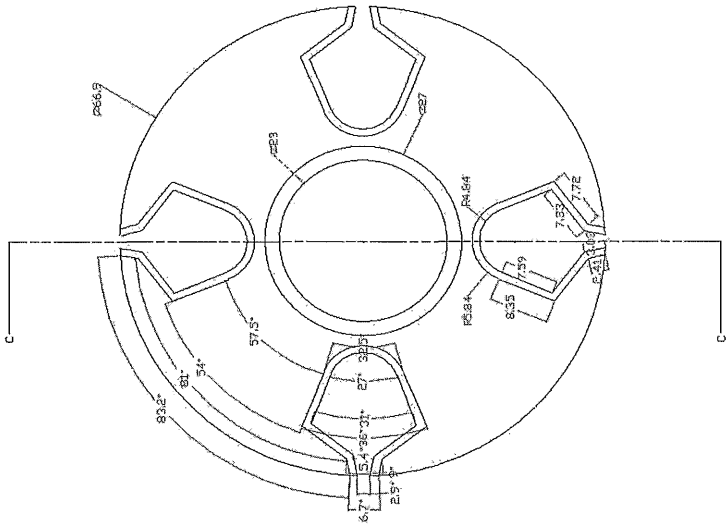
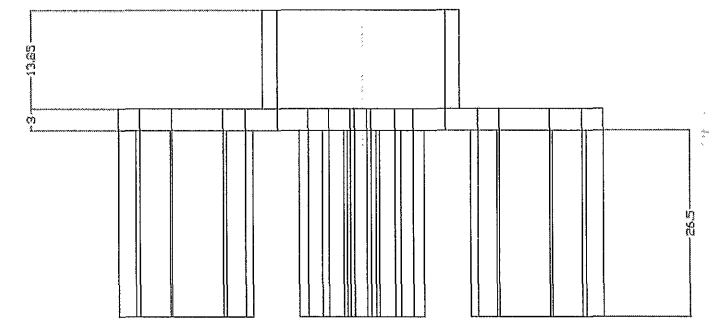
	Dimensions in mm 54612
	MATERIAL STAINLESS STEEL
QUANTITY: 2	QUANTITY: 2



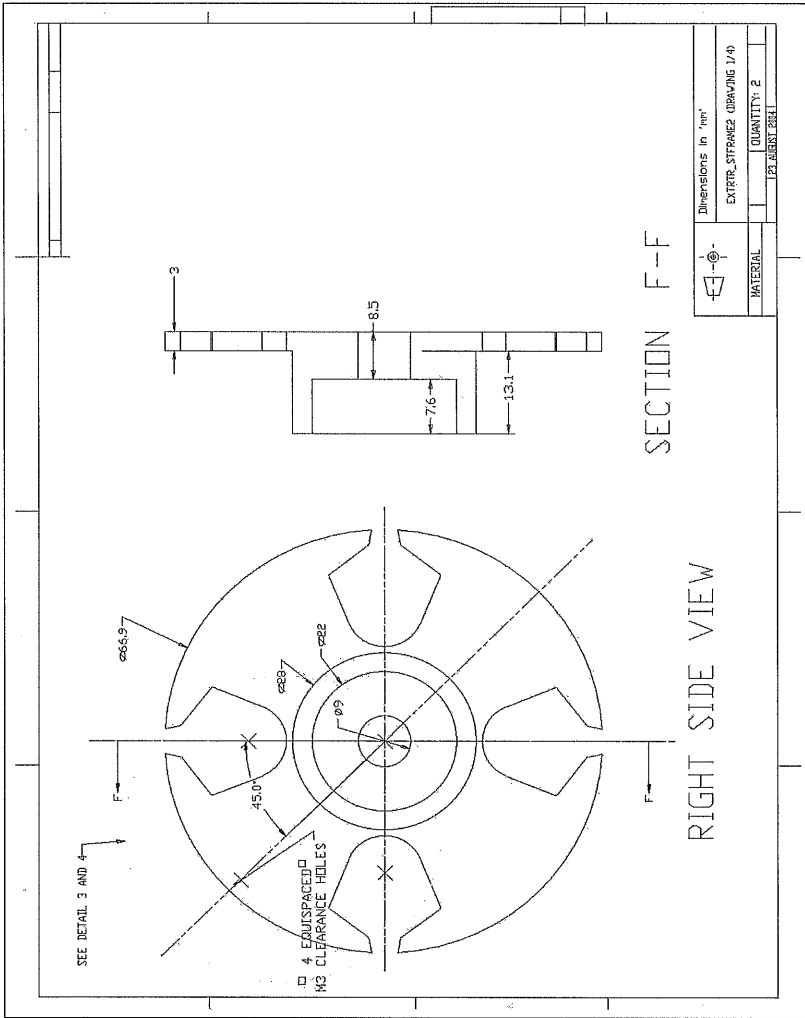


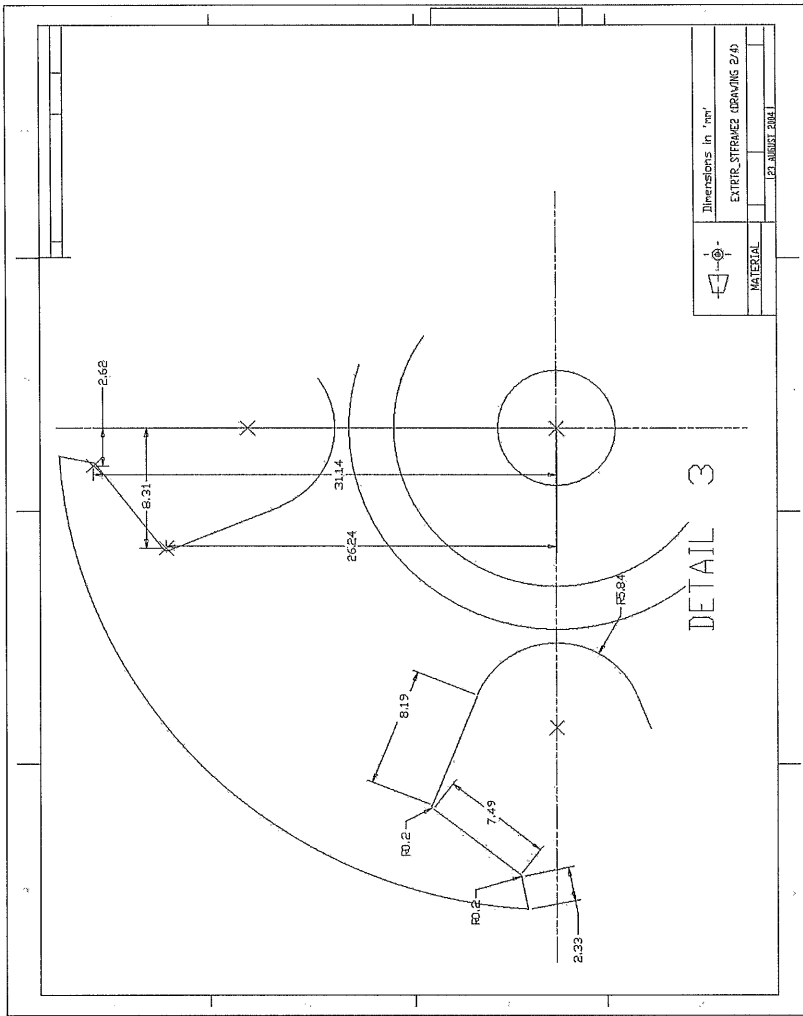


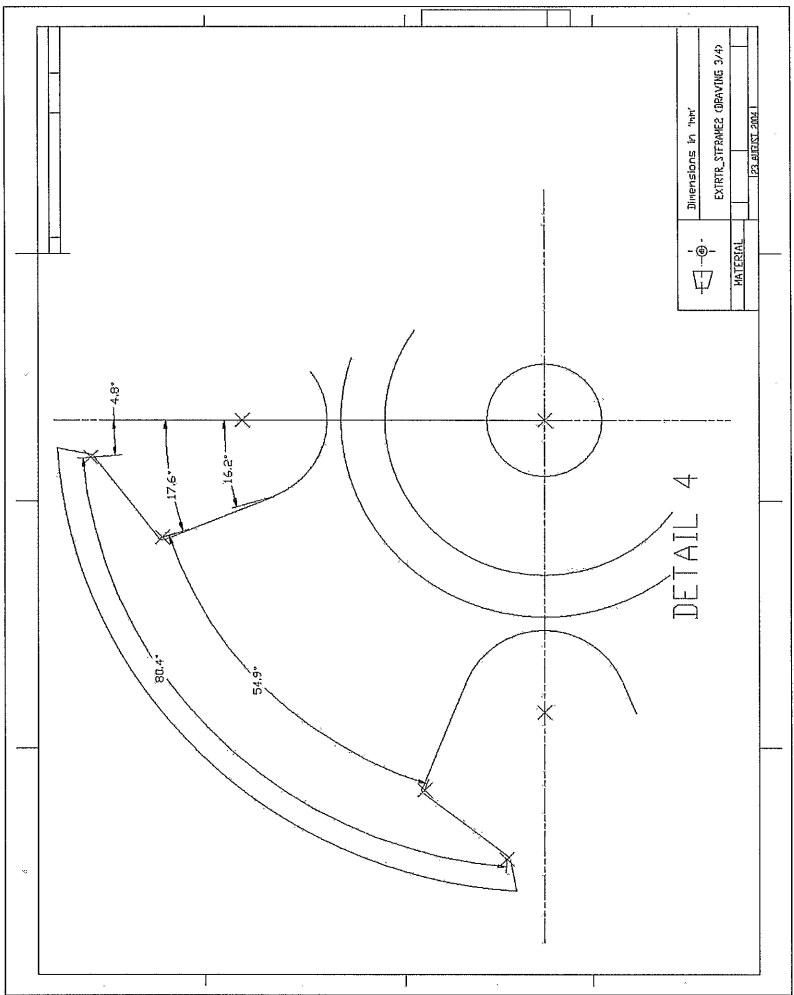


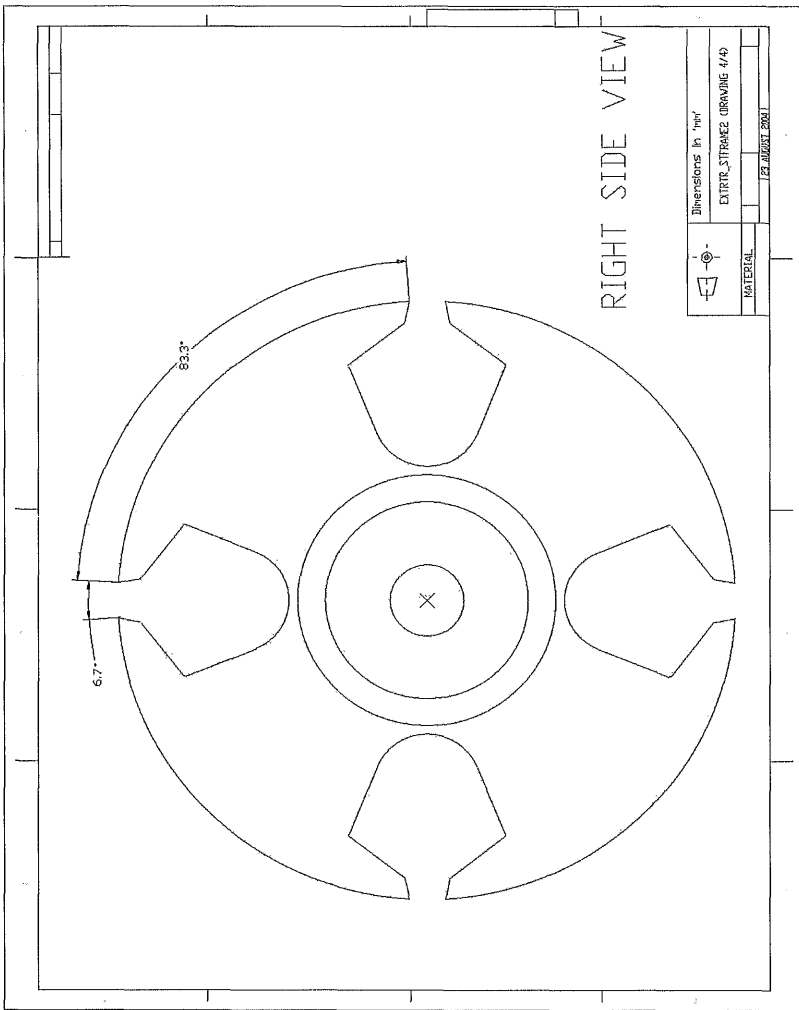


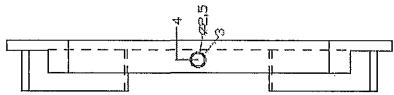
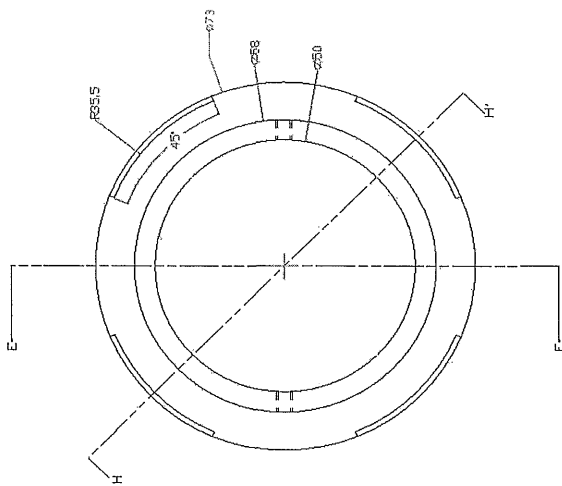
NAME EXTRA STRAWER
 HANDBAU GLASS-FILLED POLYMER
 Dimensions in mm



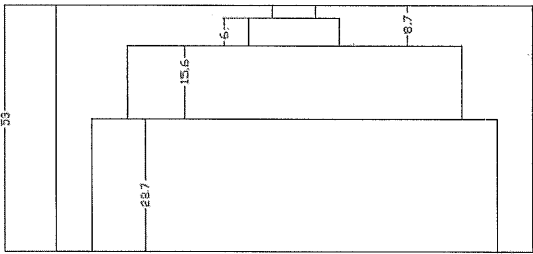
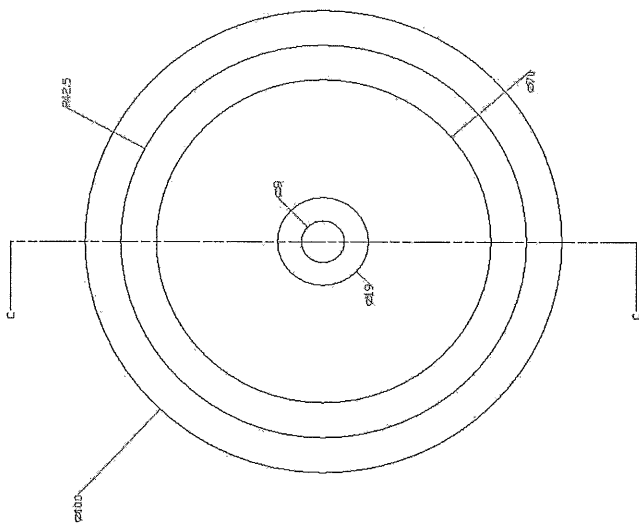




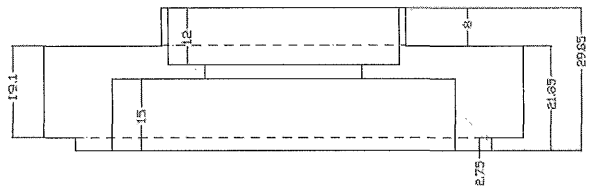
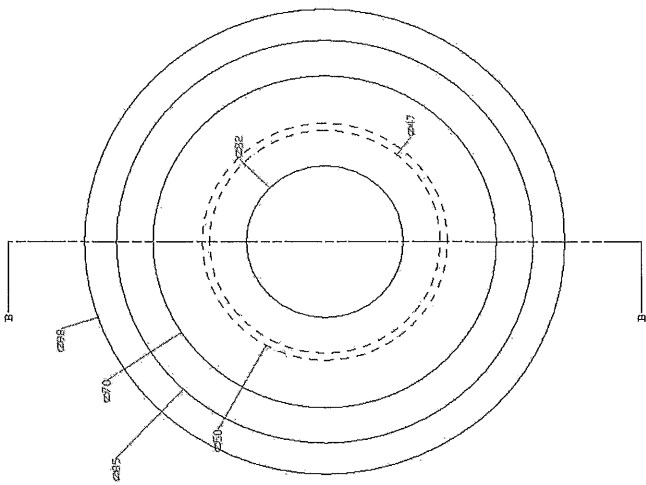




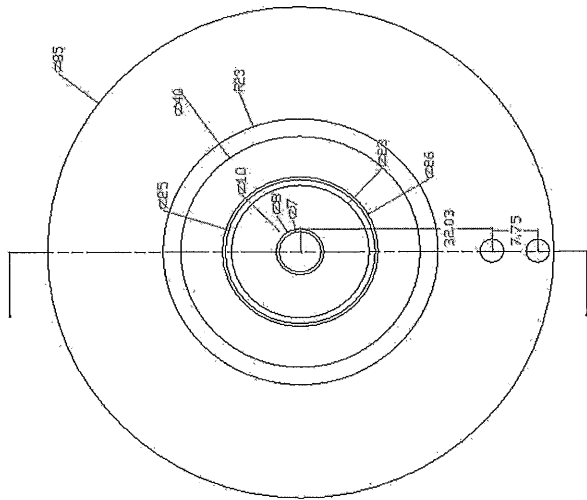
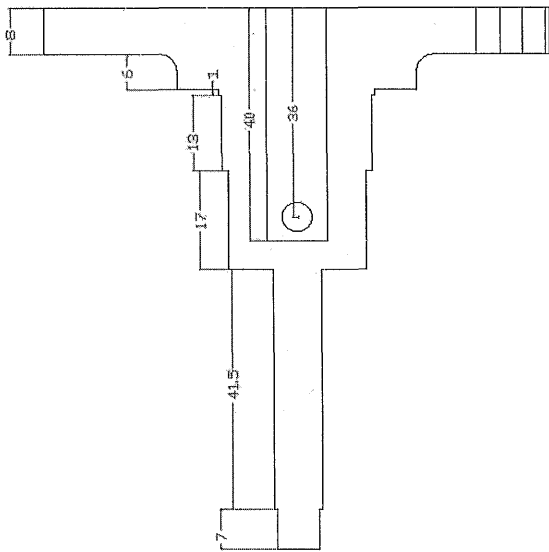
NAME: INTERTEC INTERCEPT2
 MATERIAL: ALUMINUM
 QUANTITY: 1
 DATE: 9 DEC 2004
 Dimensions in "mm"



NAME: RTEL AL FRAME
 MATERIAL: ALUMINUM
 DATE: 9 DEC 2004
 Dimensions in "mm"



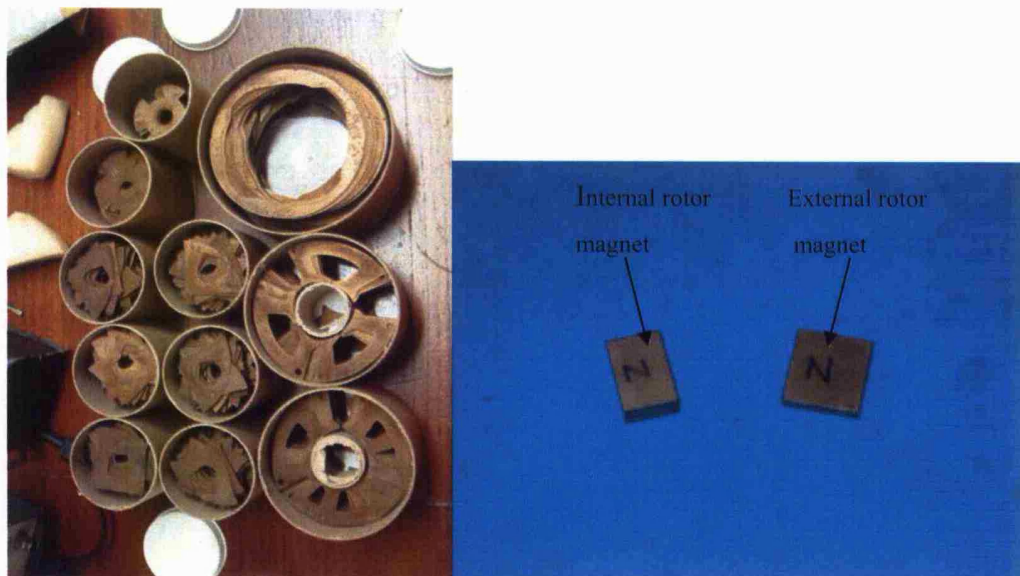
NAME: STEPHAN FRISCHER
 MATERIAL: ALUMINIUM
 DATE: 10.11.2004
 Dimensions in "mm"



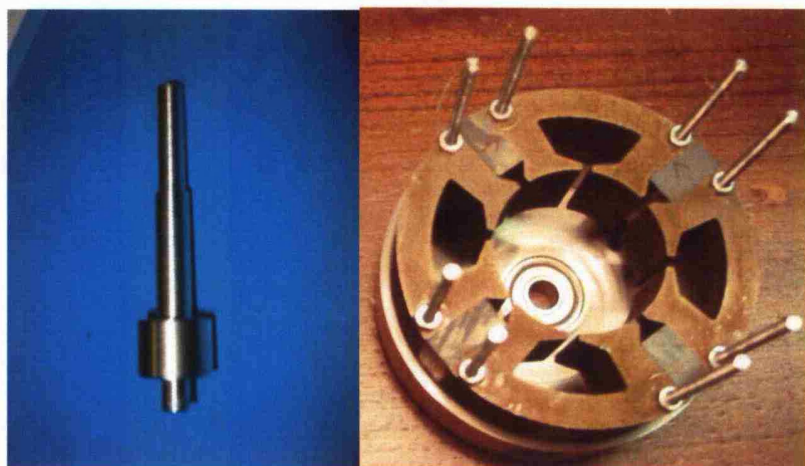
NAME: STATISHAFT
 MATERIAL: STAINLESS STEEL
 QUANTITY: 1
 DATE: 9 DEC 2004
 Dimensions in mm

Appendix F

Assembly of INTPMFSM 2 and EXTPMFSM 2

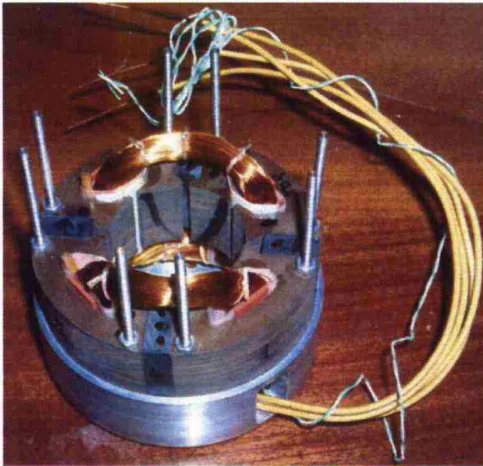


Stator and rotor laminations, and permanent magnets for INTPMFSM 2 and EXTPMFSM 2

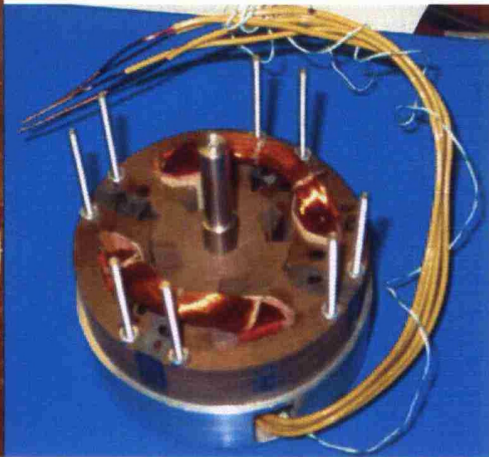


INTPMFSM 2 shaft

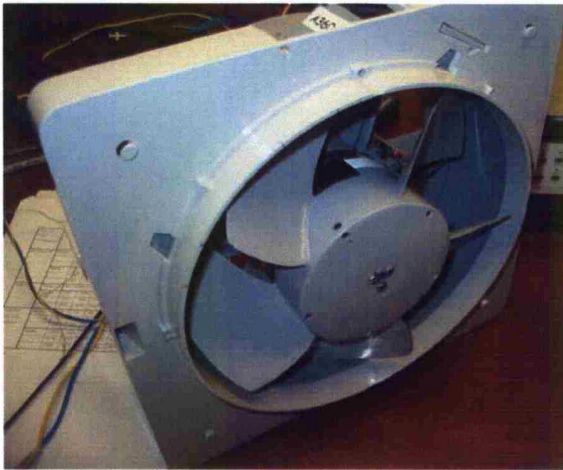
Partial assembly of INTPMFSM 2 with end-caps, stator laminations and magnets



Partial assembly of INTPMFSM 2 with coils



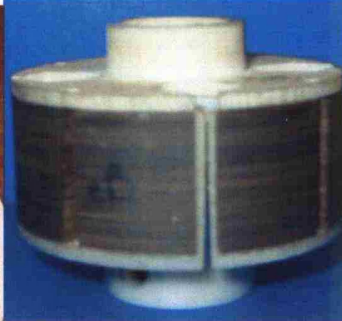
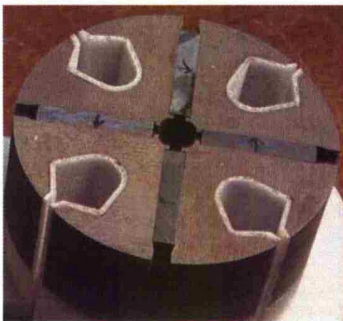
Partial assembly of stator and rotor parts



Final assembly onto existing housing of INTPMFSM 2



Static shaft for EXTPMFSM 2 Plastic stator lamination frame for EXTPMFSM 2



Stator lamination, magnets on frame assembly of EXTPMFSM 2



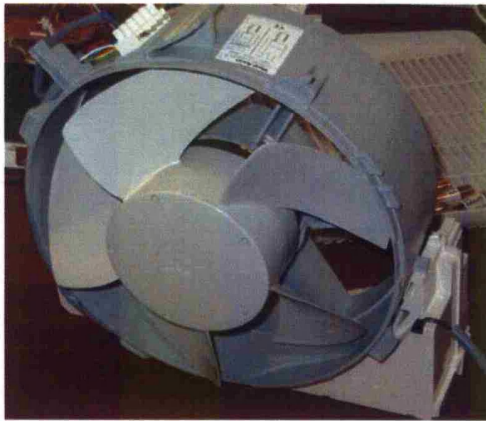
Front view

Back view

Partial assembly of stator assembly into static shaft with one part of rotor frame for EXTPMFSM 2



Rotor lamination and frame assembly for EXTPMFSM 2



Complete assembly into existing housing for EXTPMFSM 2